

University of Denver

Digital Commons @ DU

Electronic Theses and Dissertations

Graduate Studies

1-1-2012

Micro Channel Cooler Performance Improvement by Insonation

Peter Webb Higgins
University of Denver

Follow this and additional works at: <https://digitalcommons.du.edu/etd>



Part of the [Mechanical Engineering Commons](#)

Recommended Citation

Higgins, Peter Webb, "Micro Channel Cooler Performance Improvement by Insonation" (2012). *Electronic Theses and Dissertations*. 825.

<https://digitalcommons.du.edu/etd/825>

This Dissertation is brought to you for free and open access by the Graduate Studies at Digital Commons @ DU. It has been accepted for inclusion in Electronic Theses and Dissertations by an authorized administrator of Digital Commons @ DU. For more information, please contact jennifer.cox@du.edu, dig-commons@du.edu.

MICRO CHANNEL COOLER PERFORMANCE IMPROVEMENT BY
INSONATION

A Dissertation

Presented to

The Faculty of Engineering and Computer Science

University of Denver

In Partial Fulfillment

of the Requirements for the Degree

Doctor of Philosophy

by

Peter W. Higgins

August 2012

Advisor: Dr. Corinne S Lengsfeld

©Copyright by Peter W. Higgins 2012

All Rights Reserved

Author: Peter W. Higgins
Title: MICRO CHANNEL COOLER PERFORMANCE IMPROVEMENT BY
INSONATION
Advisor: Corinne Lengsfeld
Degree Date: August 2012

ABSTRACT

The motivation for this work is the need to remove waste heat from laser diodes and high speed transistors in processes which are exponentially increasing past 1 kW/cm^2 as anticipated by Moore's Law. The hypothesis guiding the work is that ultrasonic insonation of micro coolers employed to dissipate these heat loads can improve heat removal. It is thought that the mechanism promoting the benefit is enhancement of the ability of the coolant to remove latent heat in two-phase operation by managing entrained bubble size near the cooler's exit so as to forestall flow reduction or blockage caused by large bubbles, wedges and slugs accumulating there. Insonation experiments to prove the hypothesis have been done on several micro channel coolers in the range 4-80 kHz to quantify improvement in heat flux removal. In order to understand how insonation would produce benefit in heat removal, a research effort was undertaken to study the affect of 5-30 Pa acoustic fields on air bubbles rising in small aquariums. This involved developing a Faraday cage shielded acoustic probe, along with a force-beam calibration tool, for measuring field levels near a strongly electromagnetic-radiating ultrasonic source. Experiments were conducted on columns of pseudo monodisperse, sub-millimeter diameter air bubbles in water, and other fluids using bubble generators optimized for this purpose. A numerical analysis model based on energy balance of the acoustic work done

on a bubble resulted in predicting mass transfer flux, and in quantifying bubble shrinkage and growth when irradiated on either side of its resonance. The model, and experiments show that bubble populations can be predictably altered by ultrasound. The research was concluded by identifying and quantifying micro channel cooler performance change when insonated in the range 4-80 kHz. It was discovered that 28 and 58 kHz radiation of exchangers having hydraulic diameters spanning 0.02 to 0.6 mm could produce heat flux removal improvements of 5 W/cm^2 in devices normally removing less than 30 W/cm^2 , a factor of 17%. Peak thermal resistance improvement approaching 60 % has been observed.

ACKNOWLEDGEMENTS

The support of my advisor along with the fellow students in her BioFluids lab is greatly appreciated. A special thanks to my wife, Catherine, for her patience and encouragement for the long hours of work to make the 10000 pictures and videos, and dozens of test fixtures necessary for finishing this work.

TABLE OF CONTENTS

Chapter One: Introduction	1
Objective	3
State-of-the-art	4
Outline.....	7
References.....	7
 Chapter Two: Acoustic probe	 10
Introduction.....	10
Objective	13
Design, Fabrication And Characteristics Of Sensor	14
Design	14
Sensor calibration.....	18
Performance validation	20
Experimental methods	20
Experimental Apparatus.....	22
Acoustic field model.....	23
Results of Experimental Work.....	24
Predicted vs. Measured Signal.....	24
Shielded vs. Unshielded Probe Measurements	25
Phase as a Function of Position	29
Discussion	31
Predicted vs. Measured Signals	31
Shielded vs. Unshielded Measurements	33
Phase as a Function of Position	34
Conclusion	35
References.....	37
 Chapter Three: A thermodynamics approach to pulsing bubble growth	 40
Introduction.....	40
Objective	41
Method	41
Mass Change.....	43
Modeling.....	46
Experimental studies of bubble size change	55
Experiment to study growth in degassed water.	59
Results and discussion	60
Acoustic profiles in test tank.....	60
Model validation experiments in plain water.....	63
Bubble growth in degassed water	65

Mean population shift caused by insonation.....	67
Model Predicted bubble behavior	74
Conclusions.....	80
Nomenclature.....	82
References.....	86
Chapter Four: Improving micro cooler performance by insonation	90
Introduction.....	90
Recent approximations of heat flux in low quality boiling.....	94
Fluent modeling of bubble development near the exit of a cooler	95
Heat transfer coefficient and hydraulic diameter.....	96
Objective and Methods	98
Insonation System.....	100
Thermal resistance of insonated heat exchangers.....	102
Results and Discussion	109
Optical Assessment.....	109
Experiments on a milli and a micro channel cooler.....	111
Pulsed-mode experiments.....	121
Discussion of results	121
Conclusion	124
References.....	125
Chapter Five: Summary	127
Hypothesis.....	127
In order to test the hypothesis	127
Transducers and their operation.....	128
Producing, irradiating and photographing rising bubbles in water.....	128
Measuring the acoustic field.....	129
Modeling the effect on rising bubbles	129
Testing the hypothesis on micro channel coolers	130
Conclusion of the work.....	131
Appendix A: Photography	132
Getting started.....	132
High-resolution bubbles in flight from a porous wooden bubble block	133
Bubbles coalescing.....	137
Bubble aggregation.....	139
Appendix B Nucleation from insonation in micro channels.....	140
Introduction.....	140
Minnaert vapor bubble sesonance.....	141
Forced nucleation.....	142
Bubbles undergoing nucleation.....	143
Conclusion	145

Appendix C-Transducer driving circuit	146
Appendix D Piezoelectric Properties of Project Transducers.....	148
Manufacturers specifications for transducers	148
Property Values.....	149

LIST OF FIGURES

Figure 1.1. (Fig 1 from Reuse[4] credit Research Center of Karlsruhe) (A) Micro-channel plates, (B) Housing of the two-passage micro-structured reactor.	3
Figure 2.1. Image of sensor, sensor assembly and Faraday cage	15
Figure 2.2. A polar plot of the normalized radiation reception pattern for the 15 mm PZT probe evaluated from 90 to 270 degrees for 20, 40, 60 and 80 kHz acoustic fields. 16	
Figure 2.3. Probe signal response as a function of frequency (e.g., 20, 40, 60, and 80 kHz). Error bars represent a $\pm 0.2 \text{ E-}05$ volt uncertainty in the signal voltage reading which amounts to approximately 10 %.	17
Figure 2.4. Photograph of force beam calibration device with grounded target being insonated by a secondary standard transducer.....	20
Figure 2.5. Test cell and setup for verifying probe performance.....	23
Figure 2.6. Measured acoustic field compared to modeled field with probe between two radiating transducers.....	25
Figure 2.7. Transducer driving voltage signal impressed on the radiating transducer at terminals A and B (left callout), transformed by the response function of the radiator and broadcast into the water. Broadcasted signal, including reflections, is detected by the probe sensor housed in a Faraday cage, and transformed by the response function of the probe transducer. The resultant signal from the probe is output on terminals C and D which are attached to the oscilloscope. The signal at the oscilloscope is shown in the callouts on the right, when cage is grounded (top), or ungrounded (bottom). The probe is 9 cm from the radiator. In both cases the negative lead of the probe transducer is grounded and incased in shielded instrument cable.	27
Figure 2.8. Discrete Fourier Transform of normalized signals from (a) voltage impressed on the radiating transducer, labeled voltage driver dft, (b) signal from the grounded probe, labeled grounded probe dft, and (c) signal from the ungrounded probe, labeled ungrounded probe dft.	28
Figure 2.9. Schematic of experimental conditions (a) a radiating transducer insonifies two probes labeled 1 and 2; (b) probe 1 is then displaced in the horizontal direction by 2 cm moving closer to the source.	29
Figure 2.10. Grounded probe response for (a, left) probe distances of 10 and 14 cm from the source, and (b, right) probe distances of 8 and 14 cm from the source.	30

Figure 2.11. Lissajous plots for probe response when (a) grounded and (b) ungrounded for the probe positions in Fig. 9 (b).	30
Figure 2.12. Correlation coefficient between the two waveforms in Figure 8 as a function of fractional period displacement between them.	32
Figure 3.1 Normalized bubble growth and shrinkage predicted by Rayleigh-Plesset when the magnitude of the acoustic signal is 100 Pa.	47
Figure 3.2 Bubble in water, surface control volume.....	48
Figure 3.3. Experimental setup for the study of individual air bubble size change resulting from ultrasonic insonation.	56
Figure 3.4. Typical bubble photographic montage used to track and quantify bubble size and population changes.	58
Figure 3.5. Acoustic field survey setup.	61
Figure 3.6 Acoustic field strength along the vertical axis of the 4 element transducer array as was used to measure bubble response to 4-8 kHz stimulus.	62
Figure 3.7. Bubble growth of 12.3% in 14 mm when insonated at 5 kHz, and shrinkage of -1.9% when insonated at 8 kHz over a distance of 21 mm.	63
Figure 3.8. Bubble growth when insonated at 5 kHz, $\omega/\Omega = 1.37$, and shrinkage when insonated at 8 kHz, $\omega/\Omega = 0.88$, over a distance of 21 mm. (Data points from Fig. 3) compared to the model prediction.	64
Figure 3 9. Bubble growth in degassed 20 C water compared to growth in plain water. Bubbles were the same size to start, error bars are $\pm 1\%$ reflecting error in size resolution by ImageJ processing.	66
Figure 3.10. Distribution change in a generated pseudo-monodisperse air bubble column resulting from insonation at 5 and 6 kHz. The ordinate is the normalized bubble count in bins of bubble resonant frequency increments plotted on the abscissa in kHz. The mean frequency of the original bubble column and of the same column when insonated at 5 and 6 kHz is shown by dashed lines.	67
Figure 3.11 10 consecutive images of a rising air bubble column whose mean frequency is 9.7 kHz being insonated at approximately 1/20 bar by a 8.5 kHz continuous sine wave.....	70

Figure 3.12. Flow diagram of ImageJ macro to process sets of unforced, and forced photographs.	71
Figure 3.13. Two mono-dispersed bubble columns exposed to forcing frequencies on both sides of the unforced population mean resonance. The ordinate is the normalized bubble count in bins of bubble resonant frequency increments plotted on the abscissa in kHz. The unforced population profile has been colored light blue, and its mean is marked by a heavy blue line. The forced population is colored light green, and its mean is shown by a heavy green line. These colors have transparency so the overlap in population frequency is a darker blue-green tint.	73
Figure 3.15 a-e. Result of model parameter variations on bubble change.....	77
Figure 4.1 (Figure 15 from Cubaud [6]) Pressure drop as a function of capillary number showing flow regimes. Channel height is 200 microns.....	93
Figure 4.2. Shaded box containing bubbles is effective operating range for insonated heat exchanger performance improvement.	94
Figure 4.3 Variation of heat transfer coefficient for low values of quality and mass flux, G	95
Figure 4.4 Fluent modeling of developing bubbly flow in milli channel cooler	96
Figure 4.5 Heat transfer coefficient, h , and surface area to coolant volume as a function of micro channel scale.	98
Figure 4.6 Setup for video taped channel study.....	100
Figure 4.8 Apparatus setup for milli channel cooler.....	104
Figure 4.9. Electrical schematic for pulse generator.....	106
Figure 4.10 Fourier analysis of pulse shape; (left) long duration test pulse as determined by the value of pulse capacitor, (center) dft of pulse (right) dft of same pulse but occurring 10 times faster.	108
Figure 4.11 Setup for pulsed experiments. A closed alcohol coolant circuit was used..	109
Figure 4.12. Images extracted from video of insonated small channel	110
Figure 4.13 Variation in exit coolant temperature versus quality.....	113

Figure 4.14 Profiles of the difference of heater and cooler temperature as a function of coolant temperature when the state of the coolant in the micro channel is under the saturation dome. Plots are for Fixture 1 for flow rates of 2-6.2 mL/min, and insonation of 28 and 58 kHz.....	115
Figure 4.15 Profiles of the difference of heater and exchanger temperature as a function of coolant temperature when the state of the coolant in the micro channel is under the saturation dome. Plots are for Fixture 2 for a flow rate of 4 mL/min, and insonation of 39 and 80 kHz.	116
Figure 4.17 Best cases detail from the multi-frequency, multi-flow rates survey	118
Figure 4.19 Thermal resistance reduction from insonation at 39 and 80kHz of fixture 2 at 3.6 mL/min flow rate.....	120
Figure 4.20 Pulsed mode experiment heat flux results	121
Figure A.1 Olympic 35 mm film – Bubbles in flight	133
Figure A.2 Olympus E-510 10 MPx digital, Zuiko lens.....	134
Figure A.3 Bubbles forced into contact	136
Figure A.4 Bubbles coalescing when forced	137
Figure A.5 Bubbles aggregation when forced	139
Figure B.1 Apparatus for the study of nucleation by insonation.....	140
Figure B.2 View of the 9.6 mm channel.....	142
Figure B.3 small bubble $r = 0.221$ mm created by nucleation in 28 KHz field.....	144
Figure B.4 small bubble $r = 0.222$ mm created by nucleation in 28 KHz field.....	144
Figure C.1 Amplifier driving circuit for PZT transducer operation	147
Figure D.3 Piezoelectric crystal expanding in length (top) and width (bottom)	150

Chapter One: Introduction

There is an ever increasing requirement for effective heat dissipation to support accuracy, reliability and long life span of compact electronic devices especially for lightweight design constraints associated with the Department of Defense and NASA missions [1][2]. Heat dissipation needs are projected to rise well above 1000 W/cm^2 . Currently the best micro channel coolers work in the $100\text{'s } \text{W/cm}^2$ well below this projected level. Typically micro channel coolers or reactors couple high-thermal conductivity metals such as copper to the surface of the high temperature electronic device. This metal base is fabricated from numerous metal sheets that have been etched by lithography to produce small parallel passage dimensions of 12.5 to 250 micrometers. The metal walls act as fins allowing a massive increase in heat flux area into the cooling fluid (i.e. water, ammonia refrigerants).

One method for achieving a higher flux density is to utilize the latent heat available during a phase change. Several researchers have proposed the use of two phase flow within micro channels to enhance heat flux densities [3][4]; however, the fluid flow regimes are often compromised by the magnified effect of surface tension causing bubbles to collect and halt the liquid flow.

Our hypothesis is that a 0.5-0.8 bar acoustic field can be applied to micro-channel flows to allow operation beyond current dry-out conditions by managing bubble size so as to operate near phase change giving access to both latent and sensible heat transfer. Acoustic fields can also nucleate bubbles in the bulk, dislodge bubbles on the wall by acoustic streaming or mechanical agitation, as well as preventing the transition from bubbly to wedge flow. The aggregate improvement has the additional benefit of reducing pressure drop associated with friction factor by a factor of up to three [5].

Currently realization of multi-phase improvements is hampered by a poor ability to induce localized nucleation, the development of a gaseous insulation layer of wall bubbles and by dry out [5][6] conditions where the bubble size has grown to the height of the channel, plugging the main flow as a result, limiting the overall accessible flow rate and reducing heat extraction. It is already understood acoustic waves can cause cavitation in fluid flow [7]. Additionally the concept of how acoustic streaming can eject liquids [8] has been investigated in micro channels. However, little attention may have been paid to bubble management by rectified mass transfer. If the largest bubble size could be continually controlled to a fraction of the channel width, successful implementation would be achieved as volumetric flow rate would be sustained under any conditions ensuring a liquid layer at the channel wall.

In addition to micro channel coolers another promising application area, according to a recent article by Silva [9], are micro channel reactors used in constructing small scale automotive fuel cells, production of commodity chemicals and converting

waste to biofuels. This is confirmed in an article by Reuse [10] in which he states, “Micro-structured reactors are much more suitable for the distributed production of hydrogen compared to conventional systems. They are characterized by three dimensional structures in the sub-millimeter range.” Since our work focuses on improvements in a single micro channel it is relevant to all of the above applications because all have similar flow restrictions. Below is a figure from Reuse’s paper showing a commercial micro channel reactor.

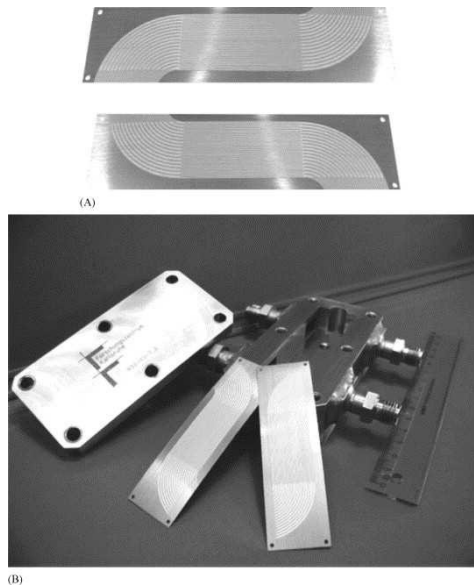


Figure 1.1. (Fig 1 from Reuse[4] credit Research Center of Karlsruhe) (A) Micro-channel plates, (B) Housing of the two-passage micro-structured reactor.

Objective

The objective of this effort is to determine if bubble management is possible in micro channel coolers using low to moderate intensity ultrasound to improve heat transfer

rates and flow. To complete this task in a manner that would be reproducible in other labs as well as easily applied to a variety of micro channel operating conditions, three specific tasks were under taken. First, a probe suitable for reliably measuring the transient pressure field from an acoustic source was developed, calibrated and validated. Second, a simple model to describe rectified mass transfer was proposed to predict the change in bubble size as a function of forcing frequency and intensity. This model was validated using photographic data from rising bubbles and pressure measurements from the probe. Finally, the application of this rectified mass transfer to manage bubble sizes with low power acoustic sources attached to micro channel coolers was studied.

State-of-the-art

In addition to the comprehensive review of this subject which presents CFD modeling of slug flow, and the advantages of multiphase operation of micro channel coolers by Gupta [6], the present state-of-the-art of micro channel cooler development is discussed in a recent survey article by Brandner, et. al. [11]. The characterizing parameter of these devices is hydraulic diameter:

$$d_h = 4 \frac{A_{cs}}{C_{ch}} \quad (1)$$

in which d_h is the hydraulic diameter, A_{cs} is the area cross-section of the channel and C_{ch} is the wetted channel circumference. Micro channel coolers optimize hydraulic diameter by maximizing wetted surface as a function of cooler volume. The disadvantage of these small channel devices include: pressure drop to force the coolant through them

which consumes pumping energy, expensive machining or chemical etching needed to achieve minimal surface roughness for operation in laminar flow and fouling.

Recently, progress in micro channel cooler design has included concurrent and contra flow devices in three dimensional geometries, i.e. arrays. Because micro channel coolers can remove, or add, high quantities of heat and mass relative to their size, and can be located closer to the source requiring this, industrial applications especially in laser diode heat management have proliferated, and industrial interest in micro channel reactors is expanding due to the desire to replace the automobile engine with a fuel cell that can make its own hydrogen from gasoline, and in producing biofuel from waste as a green conservation measure.

The potential mechanisms for bubbly flow management in these devices are numerous. Many observations in the literature discuss condensation, fracture and splitting of bubbles using electric fields [12][13], hydrodynamic shear gradients [14] and acoustic forcing [15]. Additionally, acoustic fields producing streaming has been studied as a mechanism for enhancing heat transfer [16]. The electric field required to split 500 μm bubbles is on the order of 35 kV [12] thus has limited application in many industrial settings especially with conductive liquids. The hydrodynamic shear gradient option is difficult to achieve in low Reynolds number applications like those discussed above. Thus the acoustic forcing option appears to be the most diverse in application, but to our knowledge the majority of the literature in this area is directed to theoretical/analytical exploration of the process, or experiments that utilize high power conditions which are

unlikely to be adopted by commercial applications. Absent in the micro channel cooler literature is utilization of more subtle bubble management techniques like rectified heat and mass transfer. We hypothesize that bubble management can be obtained using significantly lower energy systems than are discussed in the literature.

Neither in Brandner's or Gupta's article, nor in their list of references, is improvement by insonation (or by impressed electric fields) mentioned as a means of overcoming the inherent disadvantages. Should ultrasonic insonation further enhance performance of these devices by the means given above, it's possible that industrial applications will increase.

Concerning flow resistance, a major factor for the operation of a micro channel coolers, Gupta [6] and Cubaud [5] among many others have studied flow regimes for two-phase flow in them concluding that flow passes from bubbly to wedging to slug (Taylor flow) then annular to dry. Of interest is the considerable increase in friction factor of a factor of three in transitioning from bubbly to wedging flow. Thus, if insonation has the effect of preventing smaller than channel height bubbles to grow or coalescence leading to wedging flow, then a major benefit is achieved in throughput for a given pumping energy. A similar benefit is achieved by eliminating bubble congestive blocking in channel corners.

Outline

Following are three chapters showing the progression of the research work in support of demonstrating the stated objectives. Chapter two concerns the development of an acoustic probe to quantify the magnitude of the acoustic fields that produce measured effects on bubble elimination and size change. This paper has been peer reviewed, then published (June 2012) in the *Journal of Engineering and Applied Science*.

Chapter three explains the mass transfer resulting from rectified bubble growth and shrinkage in an acoustic field with a thermodynamics model, and validates the model by experiments of insonated bubbles. Currently it is under peer review of the journal *Bubble Science, Engineering & Technology*.

Chapter four documents completed research work to apply our findings on bubble insonation to improving heat flux removal in milli and micro channel devices around boiling. This research has revealed thermal resistance improvements approaching 60 %; and a US patent is being sought for it by DU. A third journal paper on this work is in preparation..

References

1. Montalbana, E., Electronic Component Cooling Solutions Wanted, *Design News*, www.designnews.com, (6/15/2015)

2. Bar-Cohen et. Al., Direct Liquid Cooling of High Flux Micro and Nano Electronic Components, *Proceedings of the IEEE*, V94, No.8, August 2006 p 1549-1571.
3. Qu, W., et al., Transport Phenomena in Two-Phase Micro-Channel Heat Sinks, Proceedings of IMECE2002, Nov 2002, New Orleans, Louisiana
4. Lee, J., et al., Two-phase flow in high-heat-flux micro-channel heat sink for refrigeration cooling applications: Part II-heat transfer characteristics, *International Journal of Heat and Mass Transfer* 48 (2005) 941-955
5. Cubaud, T., et al., Transport of bubbles in square micro channels, *Physics of Fluids*, V 16, No 12, (2004), p 4575-4585
6. Gupta, R., et al., On the CFD modelling of Taylor flow in micro channels, *Chemical Engineering Science*, 64, (2009) p. 2941-2950
7. Lentz YK, Anchordoquy TJ, and Lengsfeld CS, DNA acts as a nucleation site for transient cavitation in the ultrasonic nebulizer, *Journal of Pharmaceutical Sciences* , 2006, 95 (3): 607-619
8. Frampton, K.D., The scaling of acoustic streaming for application in micro-fluidic devices, *Applied Acoustics*, V64, I7, (July 2003), p 681-692
9. Silva, L., Processing Waste with Micro channel Reactors, *Innovation*, April-May 2009, p 24-25
10. Reuse P., et al., Hydrogen production for fuel cell application in an autothermal micro-channel reactor, *Chemical Engineering Journal* 101 (2004) p. 133-141

11. Brandner J.J., *et al.*, Concepts and realization of microstructure heat exchangers for enhanced heat transfer, *Experimental Thermal and Fluid Science*, 30 (2006) p. 801-809
12. Dong W, Li R Y, Yu H L, Yan YY, An investigation of behaviours of a single bubble in a uniform electric field, *Experimental Thermal and Fluid Science* 30 (2006) 579-586
13. Shiran M B, Watmough D J, An Investigation on the Net Charge on Gas Bubbles Induced by 0.75 MHz under Standing Wave Condition, *Iranian Physical Journal*, 2-2, 19-25 (2008)
14. Lewin P A, Bjorno L, Acoustically induced shear stresses in the vicinity of microbubbles in tissue, *J Acoustic Soc Am* Vol 71, No 3, March 1982
15. Vainshtein P, Fichman M, Gutfinger C, Acoustic enhancement of heat transfer between two parallel plates, *Int. J. Heat Mass Transfer*, Vol 38, No 10, pp 1893-1899, 1995
16. Loh B, Hyun S, Ro P I, Kleinstreuer, Acoustic streaming induced by ultrasonic flexural vibrations and associated enhancement of convective heat transfer, *J. Acoust. Soc. Am.* 111 (2), February 2002

Chapter Two: Acoustic probe

Introduction

There is a growing body of literature that documents the degradation of biological molecules from ultrasonic pressure waves [1][2][3][4][5]. For example, Wu [1] concludes that ‘cavitation is considered as a primary mechanism for the ionization of biomolecules.’ He cites cavitation bubble collapse energy release as promoting chemical reactions and ionizations such as reported for polymerization of benzene and CO₂. But, little is understood about how to control or mitigate degradation because of a lack of detailed fluid dynamic characterization of the system. Additionally, the use of ultrasonics to carry out unique chemistry for material fabrication is of current interest [6][7]. Gedanken [6] describes sonochemistry as one of the first techniques used to prepare nanosized compounds. He mentions, for instance, insonating Fe(CO)₅ to get iron nanoparticles. Both research areas would benefit from a detailed understanding of the pressure field within the fluid system. Under these operating conditions measurements are necessary close to an ultrasonic source in contact with the liquid media. When close to an ultrasonic transducer driven by high voltage, probe designs are susceptible to electromagnetic interference (EMI) from EMR because the sensor connections act as an antenna. There is,

therefore, a need for a small acoustic field pressure probe that can resolve the temporal and spatial fluctuation of the field when submersed close to a radiating piezoelectric source. This work documents the design and calibration of such a probe, and then evaluates its performance relative to theoretical predictions within a system that contains both a primary wave and reflections.

Commercial hydrophones are intended for pressure field measurements distant from sources of acoustic radiation. However, when operated close to a high voltage source, the primary electromagnetic radiation (EMR) emanating from the source needs to be subtracted, if known, or filtered [8] to isolate the voltage signal resulting from the hydrophone's sensor. Prior knowledge of the phase delay and amplitude of the EMI at that location is required. Uncertainties in these assumptions will impart error onto the actual pressure field signal, especially when the signals of interest are more than one order of magnitude lower than the driving voltage signal.

Many hydrophones are also too large to work in small test cells. Commensurate with large size, such devices have unknown, or uncertain, acoustic centers to resolve to a point in space.

There are several novel approaches to modify hydrophone operation to address specific issues. For example, to resolve position specificity, others have used a PZT ultrasonic sensor attached to a 20 cm long tapered acoustic horn [10]. These long horns have the potential to amplify the EMI problems. Bushberg [11] demonstrates a metal cage partially surrounding the PZT element without grounding to help with measurement

noise. Neither of these completely shield the PZT probe from EMI from the primary ultrasonic transducer source. Therefore, although appropriate for distant measurements, these devices will exhibit signal contamination close to a contacting source.

An alternative approach to measuring the pressure field has been to use thermocouples or thermistors [12], which are designed to make the active element (i.e., tip) an energy absorber. These devices proved incapable of quantifying acoustic fields to the desired accuracy or repeatability (unpublished work). Pugin [13] also concludes that these devices provide only a rough approximation of local maxima and minima. Susceptibility to EMI is not discussed in any of these papers. Data taken in our lab shows the connecting lead wires of these systems act as effective antennas when placed close to the source.

Durkee [14] promotes the use of strips of aluminum foil to evaluate the field strength over a cross sectional area of an ultrasonic cleaning tank [13]. In principle, stronger pressure fields produce pitting of a thin aluminum foil after about 10 minutes exposure. This technique was tried following the recommended practice. It was found that pitting was not significant, and that neither test had any temporal resolution, and only the rigidly supported strip had spatial resolution. However, the technique is immune to EMI problems.

Witte [15] reaffirms the need for low cost acoustic field sensors and describes a disposable hydrophone. The device transforms acoustic pressure into electrical energy based on the Auger Effect, relying on conductive rather than piezoelectric materials as a

sensor. The device described targets the higher frequencies used in medical applications with the lowest test conducted at 540 kHz. The devices' susceptibility to electromagnetic interference (EMI) is unknown.

Employment of a screen wire Faraday cage surrounding a PZT element sensor has been reported previously by Felizardo's group [9] during an attempt to detect the shock wave generated by bubble nucleation. In this case the sampling frequency was below 10 kHz. It was determined that the addition of a Faraday cage could induce noise into the preamplifier. A design that did not include preamplification within the probe assembly was not discussed. It is highly probable that lower frequency contamination observed could be eliminated with an alternate design.

Objective

Since no simple inexpensive means of quantifying the acoustic field environment near the radiating source (within 10 cm) was found, the objective of this work was the design of an acoustic probe having an appropriately sized planar PZT disk within a grounded Faraday cage for quantitatively measuring the pressure waves emanating from a 44 kHz driven ultrasonic transducer submerged in water. A secondary objective was the development of an accurate calibration method which would enable quantitative temporal and spatial characterization of the pressure field. To assess whether both objectives were met the probe performance was compared to a simulated 44 kHz wave with reflections.

This paper presents the construction of a probe that can resolve the temporal and spatial fluctuation of an acoustic pressure field near a radiation source. The probes' operating characteristics and methods for calibration are outlined. Then three measures to validate the sensor output are discussed: (i) comparison of the unshielded and shielded signals for magnitude and composition; (ii) comparison of experimental measurements to results by ray tracing; (iii) direct measurement of phase patterns. Finally, results from experimental measurements at multiple locations are provided as evidence that spatial differences can be resolved.

Design, Fabrication And Characteristics Of Sensor

Design

The probe assembly pictured in figure 1 was constructed for approximately \$50 USD. The round 15 mm diameter, 0.9 mm thick PZT sensor was purchased from Steiner & Martins, Inc.. It is made from SM111 PZT4 material having resonant frequencies of (Thickness) $2.2 \text{ MHz} \pm 50 \text{ KHz}$ and (Radial) $135 \text{ kHz} \pm 5 \text{ KHz}$. The resonant impedance, Z_m , is (Thickness) $\leq 1.55 \Omega$ (Radial) $\leq 11 \Omega$, while the static capacitance is $3481 \text{ pF} \pm 15 \% @ 1 \text{ kHz}$. The sensor is installed vertically, aligned with gravity. The disk is bonded by flexible Silastic to an electrically insulated pin (instead of a backplate) located on the centerline of a separately grounded, stainless-steel Faraday cage (tea stick infuser, Item # 800790, available from REI). A backplate is not needed in this application because its first resonant frequency (135 kHz) is much higher than the range of its intended use (20-80 kHz) so no attenuation of its resonant Q is required. A

front wear plate is also not needed since the sensor is protected by its Faraday cage, and long term, continuous use is not envisioned. No preamplifier is housed within the enclosure, because it is intended to be used within 2 m of a sensitive recording oscilloscope which serves as the preamplifier. Sensor connection wires are encased within a shielded instrument cable and mounted rigidly within the cage to reduce strain on the PZT disk. A separate ground wire for the Faraday cage is connected to the assembly, and is grounded at the recording oscilloscope ground. Probe signals are output in a shielded instrument cable terminated with a BNC electrical connector.

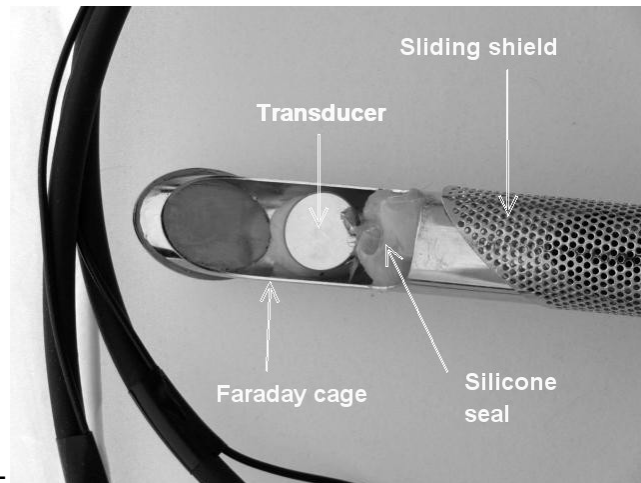


Figure 2.1. Image of sensor, sensor assembly and Faraday cage

Selecting cost effective PZT elements requires some characterization to ensure performance can be achieved within experimental tolerances. For example, planar disks are known to respond differently depending on their orientation with respect to the source. Characterization of 15 mm PZT radiation directivity can be approximated [16]

and is shown in Fig. 2. For a baffled disk (assuming the Faraday cage approximates a rigid baffle), the far field spatial pressure variation directivity factor is given by equation 1:

$$p(\vec{r}) = \frac{2 J_1(ka \sin \Theta)}{ka \sin \Theta} \quad (1)$$

where k is the wavenumber, a is the disk radius in meters, r is the vector to the far field point in meters, J_1 is the Bessel function of 1st kind, and θ is the angle from normal in radians.

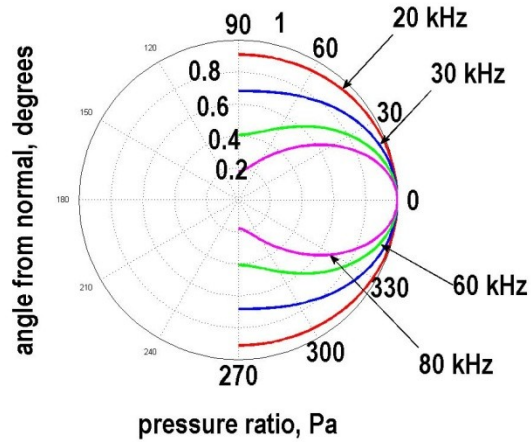


Figure 2.2. A polar plot of the normalized radiation reception pattern for the 15 mm PZT probe evaluated from 90 to 270 degrees for 20, 40, 60 and 80 kHz acoustic fields.

The results of the orientation dependency study, Fig. 2, demonstrate that a broader (more uniform) response is obtained for the lower frequencies presented within this work.

Moreover that precision alignment of the sensor and driving transducer face is also not required.

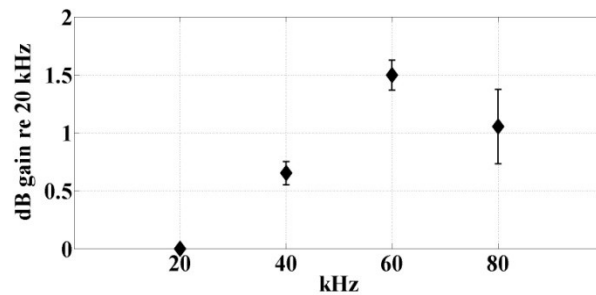


Figure 2.3. Probe signal response as a function of frequency (e.g., 20, 40, 60, and 80 kHz). Error bars represent a $\pm 0.2 E-05$ volt uncertainty in the signal voltage reading which amounts to approximately 10 %.

The frequency response of the probe is examined at the same four frequencies used to calculate angular response above to demonstrate that this PZT element will be excited by the intended driving transducer for determining the range of useful application. This is accomplished by measuring the voltage signal output of the probe along with the (RMS) power delivered to the radiating transducer at each frequency. The voltage squared output of the probe is adjusted to the same radiated power level, then the db response is computed as $10 \log$ of the response relative to the response at 20 kHz. By convention, the sensitivity should be measured in an anechoic environment, but this is a difficult measurement to make because the reflective environment in the test tank, produced by

pressure reflections from the walls of the test cell, produce nodes and antinodes near the probe which are functions of frequency as is modeled later in this paper. To overcome this effect the measurements made for the sensitivity study were pre-echoic. This means that the output of the probe was recorded by a high speed memory scope in single sweep mode to capture the probe response before being influenced by reflections. Considering the probe – radiating transducer distance was 7 cm, and the speed of sound in water at 20 C is 1481 m/s, the signal arrives at the probe in $\sim 50 \mu\text{s}$. But reflections from the nearest wall are at least 4 times this interval arriving after another $\sim 200 \mu\text{s}$. The measurements for Fig. 3 were taken before $100 \mu\text{s}$ thus avoiding the influence of reflections. The dB variation of probe response over 20-80 kHz is given in Fig. 3, showing a nearly flat response over the frequency range. This frequency response behavior is consistent with the findings of Lewin [17].

Sensor calibration

The transient and non-linear nature of the pressure field makes calibration of probes to measure the pressure magnitude difficult. The use of force measuring beams for calibration for other pressure sensors is not new, and has been reported by others [18][19]. It was decided to use a force beam apparatus that could be submersed in the water so as to directly measure the dynamic load of the transmitted signal at any desired frequency. Based on our prediction of the driving transducer's pressure load, a beam sufficiently flexible to deform under gram loads is selected. The flexible beam is a 12 cm long, 1.3 cm wide, and 1 mm thick copper strip sheared from a plate. An Omega

Engineering, Inc type KFG-3-120-C1-11L1M2R 120 Ω strain gauge is mounted 7 cm from the clamped end. A 15 mm PZT disk, identical to the probe's sensor, is attached to the tip of the flexible beam. It is important to create an identical target area, and to ensure that the strain gauge is not measuring the uncoupled vibration of a mass on its tip in addition to the acoustic field.

A Fluke model 8840A/AF precision digital desktop meter (accuracy = ± 1 m Ω) is used to quantify beam response to bending under a static (i.e., known mass) and dynamic (i.e., acoustic forcing) load. As constructed and under no load, the measured resistance is 122.389 Ω , while a 20 g static load produces a resistance reading of 122.411 Ω . Because the strain gauge is a thin foil, a slight temperature dependence is expected and observed, which is overcome by multiple readings. The resultant, experimentally determined, calibration curve slope for the force beam strain gauge under a static load is 22 m Ω /g.

The forced beam response is also observed under dynamic loading conditions. The beam is insonated by both a 44 kHz ultrasonic transducer that is driven at 20 W (electrical) and positioned 2.5 cm from the transducer face, and by an identical (to the sensor and to the target) 15 mm ultrasonic transducer at 45 kHz and at the same distance. For clarity the setup using the larger source is shown in Fig. 4. The accompanying PZT element response is observed and directly correlated to the strain gauge output from the force beam in terms of V/Pa to complete the probe calibration. For both static and dynamic loads on the beam, direct measurement of the change in resistance of the gauge is done by allowing the gauge resistance to stabilize in time, offsetting the gauge to its rest value to read zero, and then quickly making the difference measurement. This

accounts for temperature drift and additional resistance from wires and connections, which can change over time. The procedure is typically done six times and the results are averaged. Voltage measurements from the gauge are not useful because the gauge and its wiring have the same antenna effect as an unshielded probe. This method of reading the strain gauge probably resolves the criticism of strain gauge beams raised in reference 18.

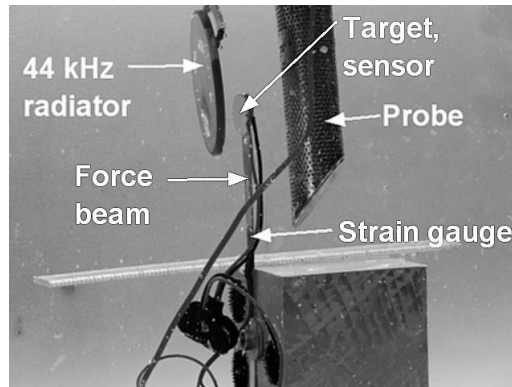


Figure 2.4. Photograph of force beam calibration device with grounded target being insonated by a secondary standard transducer.

Performance validation

Experimental methods

Different test scenarios were experimentally explored to verify that (a) the probe design isolated the transducer voltage induced EMI sufficiently to use the measured signal without other filtering or isolation methods, and (b) the probe could measure the detailed pressure field produced by an ultrasonic source:

1. Insonation of a single probe located between two continuous sine wave radiating transducers, one at 24 kHz, the other at 30 kHz (Fig. 5). The purpose is to study

the probe resolution of a complex acoustic environment, and to verify a phase shift in the detected signal. The latter objective is accomplished by displacing one of the radiating transducers 3 cm farther from the other while keeping the first transducer and the probe fixed in place. The results of these measurements (Fig. 6) are compared to an acoustic model of the expected field that accounts for the magnitude and phase contributions of chosen acoustic rays to the calculated field at the center of the probe sensor location. The chosen rays model direct radiation and 1st reflections from the top, bottom, sides and back glass surfaces. Multiple reflections are not considered.

2. Insonation of a single probe by a single transducer that is driven by a square wave to produce a complex field. The probe response is recorded with the Faraday cage grounded and ungrounded in order to quantify the degree of isolation from EMR when grounded (Fig. 7). Discrete Fourier Transforms are calculated from samples of these signals to produce a frequency spectra of the driving voltage signal, and of the transformed received signal from the grounded, and ungrounded probe, which helps establish that the grounded probe isolates the acoustic signal from induced EMR (Fig. 8).
3. Two probes of this design are radiated by a continuous sine wave, then one is moved 2 cm with respect to the other to further study complexity resolution and associated phase change (Figs.9-10). Lissajous patterns are recorded to verify the detected phase change. These patterns are created by plotting on an oscilloscope

the response of one probe on the ordinate and the other probe on the abscissa. The gain of the two channels is the same.

Experimental Apparatus

A 20 °C water-filled 8 L aquarium was used in the reported experiments to evaluate performance. The tank is glass-sided measuring 30 cm by 15 cm with a water height of 19.5 cm. The radiating transducers were 5 cm diameter by 0.3 cm thickness, PZT, SM111, planar mode vibration disks purchased from Steiner & Martins. These have a nominal natural frequency of 44 ± 3 kHz and an impedance of $< 8 \Omega$. Transducer driving signals were continuous sine waves in two experiments, and a square wave for the third. These were produced by a Leader, LAG 1208 Audio Signal Generator, and by a Victor VC 2002 digital frequency generator. Amplification of the driving signals was accomplished using a Crown Vs 1100, and a 240W dual channel amplifier, and recording was done with a Tektronix 2215 A 60 MHz oscilloscope. Signal detection was accomplished using probes of the design presented in this paper. A typical setup for testing is shown in Fig. 5.

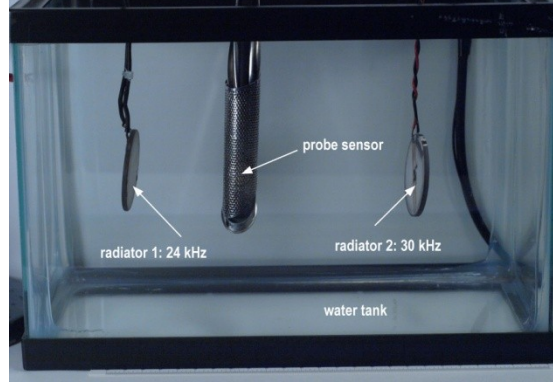


Figure 2.5. Test cell and setup for verifying probe performance.

Acoustic field model

A model approximation of the resulting wave form at the probe's sensor surface is computed from the one dimensional wave equation whose spatial and temporal amplitude, y , is given in equation 3 [20]:

$$y(x, t) = \sum_n \sum_i C_i \cos \left[\frac{2\pi}{\lambda_n} (ct - x_i) + \vartheta_i \right] \quad (3)$$

The acoustic pressure amplitude at a location is the sum of the wave amplitudes arriving from the 24, 30 and 40 kHz components radiating from the transducers directly or by reflection, and accounted for by the index, n . Six rays were considered from each radiator: the direct ray from the face of the radiating transducer to the surface of the sensor along with reflected rays from the top, bottom, sides and back glass surfaces of the tank. The rays are counted by the index i in equation 2, and have an associated phase change given by φ_i in radians. λ_n are the wavelengths for each frequency component in meters, c is the acoustic velocity in water in meters per second, x_i are the ray path

distances in meters and t is time in seconds. C_i are the relative amplitudes of each ray determined by the level of amplification of the driving voltages for the primary component, and by waveform analysis to size the induced coupling for the 40 kHz component. Unity reflection coefficients were used because the hard glass surface is purely reactive. Reflections from the far wall, and multiple reflections, are not included which are limitations in how well the model will fit the data.

Results of Experimental Work

Predicted vs. Measured Signal

The response of a single shielded probe in a complex field produced by two radiators is recorded. With respect to the bottom left front corner of the test tank, the probe sensor is situated on a centerline 7 cm from the bottom of the test tank that lies between a disk radiator at 6.5 cm and second disk radiator at 21 cm for the first measurement. Then the second transmitter is moved from 21 to 24 cm for the second measurement. These measurements of field pressure, along with modeled pressure for the same configurations, are shown in Figure 6.

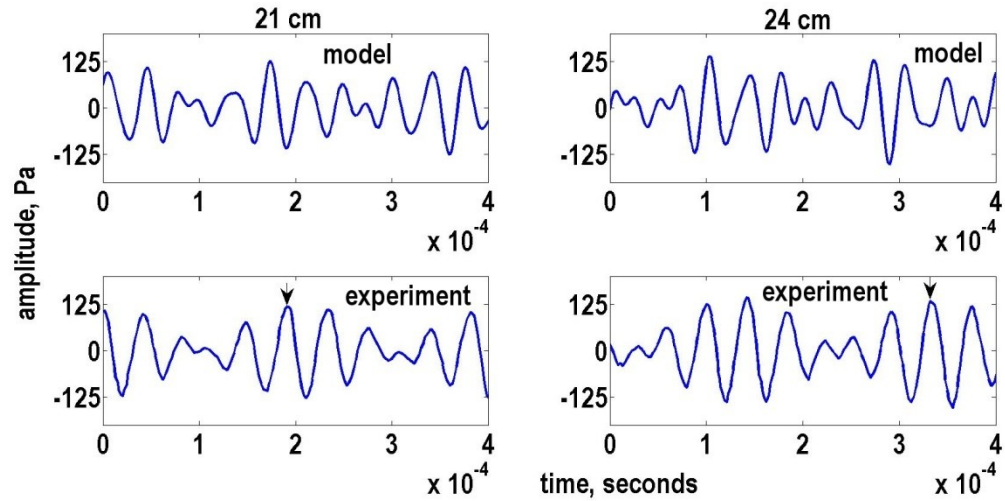


Figure 2.6. *Measured acoustic field compared to modeled field with probe between two radiating transducers.*

The radiator at 6.5 cm is broadcasting a continuous sine wave at 24 kHz along with a much smaller 40 kHz signal from transducer resonance coupling to the driving voltage. The radiator initially at 21 cm, then at 24 cm transmits a 30 kHz sine wave along with its induced 40 kHz component. The top row graphs of Figure 6 are the corresponding modeled acoustic signal obtained by first order ray tracing.

Shielded vs. Unshielded Probe Measurements

Figure 7 shows how shielded and unshielded probe measurements were made in a complex acoustic environment allowing the EMR and acoustic signals to be identified. The radiating source transducer is driven by a 50 V_{pp}, 40 kHz, square wave on terminals A and B from a signal generator described in the apparatus section. A portion of two cycles of this driving signal as recorded by an oscilloscope connected to A and B are

shown in the left callout of Fig. 7. The radiating transducer smoothes the square wave slightly as it broadcasts an acoustic signal from surface vibration caused by the piezoelectric effect into the water that follows direct and indirect (by reflections) paths to the probe sensor. Additionally, the voltage signal radiates EMR into the water since terminals A and B are submerged. This broadcasted acoustic signal is detected by the sensor of the probe from vibrations of its surface that are transformed into a voltage signal by the piezoelectric effect. If the Faraday cage is ungrounded, the electrodes plated on the probe's sensor surface pick up the EMR that becomes EMI when mixed in with the acoustic signal. The ungrounded and grounded voltage signal output from the probe on remote terminals C and D (the end of the grounded, shielded instrument cable attached to the probe) are shown in the right hand callouts. The signal strength of the ungrounded probe signal is of the order of $10 V_{pp}$, while the real acoustic signal shown in the top right callout is only millivolts in magnitude. This same millivolt acoustic signal is seen in the lower right hand callout as a straight line with no detail.

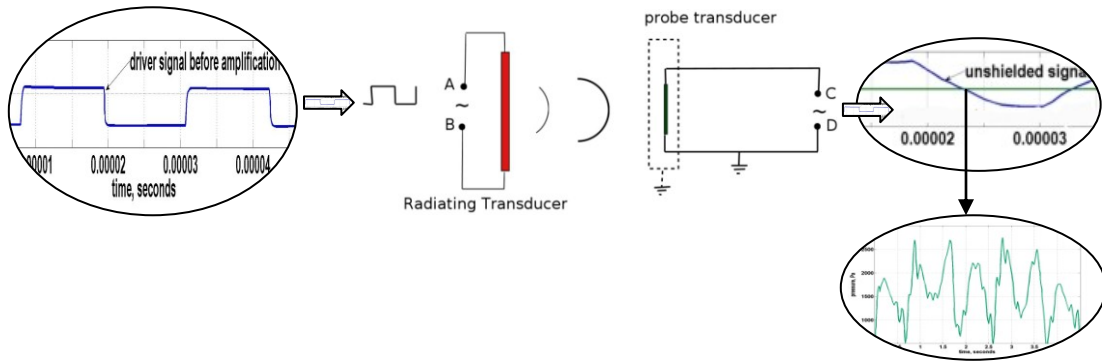


Figure 2.7. Transducer driving voltage signal impressed on the radiating transducer at terminals A and B (left callout), transformed by the response function of the radiator and broadcast into the water. Broadcasted signal, including reflections, is detected by the probe sensor housed in a Faraday cage, and transformed by the response function of the probe transducer. The resultant signal from the probe is output on terminals C and D which are attached to the oscilloscope. The signal at the oscilloscope is shown in the callouts on the right, when cage is grounded (top), or ungrounded (bottom). The probe is 9 cm from the radiator. In both cases the negative lead of the probe transducer is grounded and incased in shielded instrument cable.

The response differences between grounding and ungrounding the insulated probe (shown in Fig. 7 as a dotted rectangle around the probe sensor) can be further clarified by comparing the dominant frequency components contained in these waveforms which have been calculated using a Discrete Fourier Transform (DFT) obtained by numerical analysis solutions of:

$$X(k) = \sum_{j=1}^N x(j) \omega_N^{(j-1)(k-1)} \quad (2)$$

$$\omega_N = e^{\frac{-2 \pi i}{N}}$$

where x is the vector of samples of the waveform, N is the sample frequency, k is the number of discrete sample points, and ω contains the sine and cosine frequency components contained in the sampled waveform. The computational result, X , is the vector of coefficients of the sine and cosine components contained in x . In the implementation of this solution the waveform sample vector is converted to equal increments, and a sampling frequency adequate for temporal resolution is selected. The calculated dominant frequencies for the signals shown in Fig. 7 are plotted in Fig. 8.

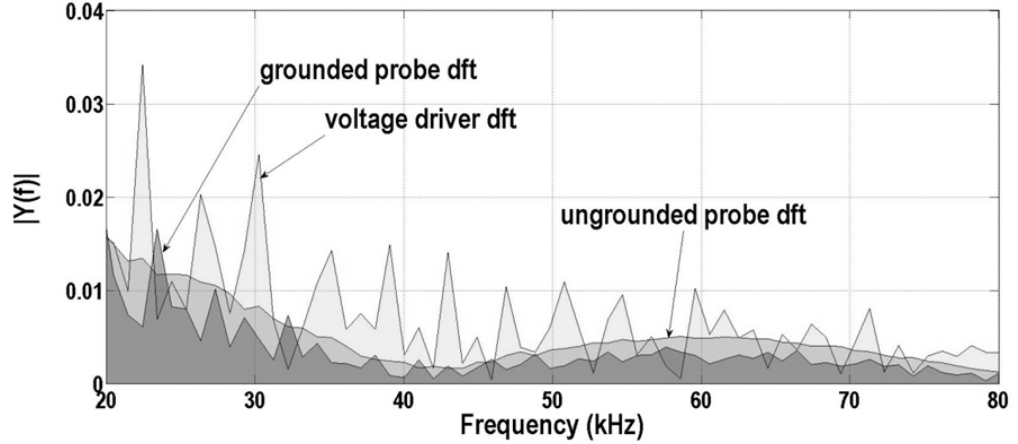


Figure 2.8. Discrete Fourier Transform of normalized signals from (a) voltage impressed on the radiating transducer, labeled voltage driver dft, (b) signal from the grounded probe, labeled grounded probe dft, and (c) signal from the ungrounded probe, labeled ungrounded probe dft.

Phase as a Function of Position

The response from two Faraday shielded probes having the design of Fig. 1 are recorded when being insonified by a single transducer radiator for studying resolution and phase change. The positioning of the probes and the radiator are shown in Figure 9.

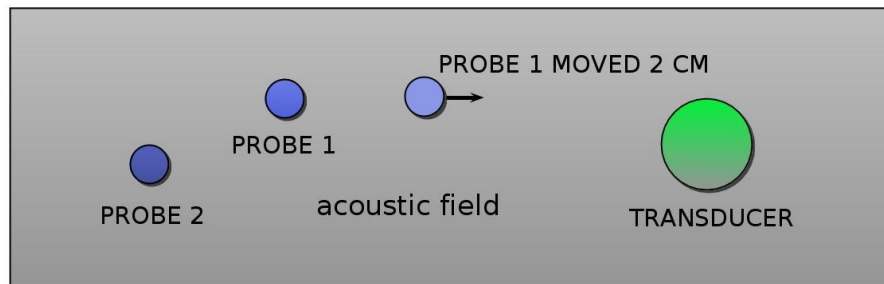


Figure 2.9. Schematic of experimental conditions (a) a radiating transducer insonifies two probes labeled 1 and 2; (b) probe 1 is then displaced in the horizontal direction by 2 cm moving closer to the source.

Fig. 2. 10 shows a comparison of the grounded probe response from the two probes in these two positions in the test tank when being insonified by the 5 cm disk radiator.

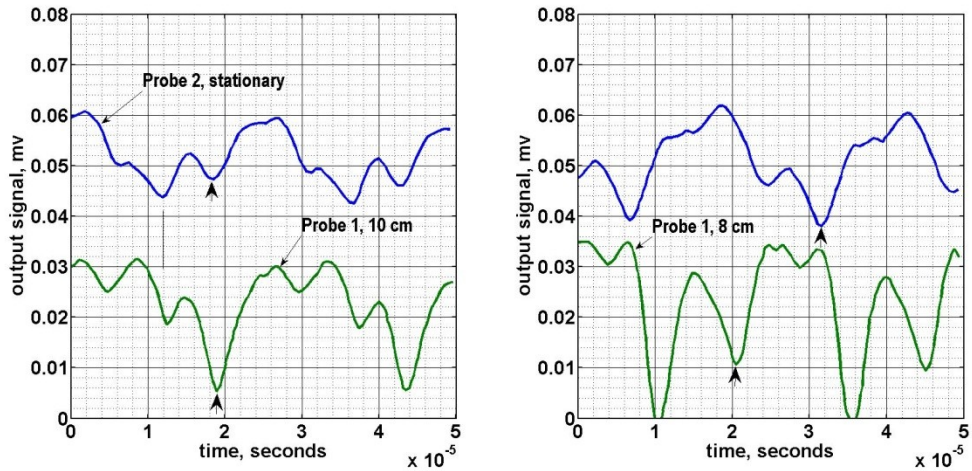


Figure 2.10. Grounded probe response for (a, left) probe distances of 10 and 14 cm from the source, and (b, right) probe distances of 8 and 14 cm from the source.

Two Lissajous plots were made using the grounded and ungrounded probe signals when separated by 6 cm, and are shown in Figure 11. These are made by connecting the signal from each probe to separate input channels of an oscilloscope set in the XY plotting mode and setting the gain of each channel to be the same

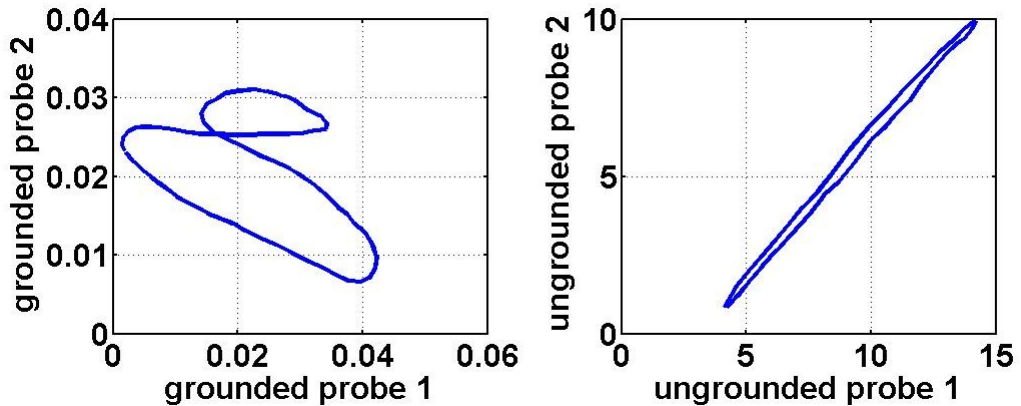


Figure 2.11. Lissajous plots for probe response when (a) grounded and (b) ungrounded for the probe positions in Fig. 9 (b).

Discussion

Predicted vs. Measured Signals

The correlation characterizing the fit of the predicted signal by ray tracing to the experimentally measured signal for the two opposing transmitter case was determined from equation 4 [23] and plotted as a function of signal incremental displacement in Fig. 12.

$$r_{xy} = \frac{\sum_{i=1}^n (x_i - \bar{x})(y_i - \bar{y})}{\sqrt{\sum_{i=1}^n (x_i - \bar{x})^2 \sum_{i=1}^n (y_i - \bar{y})^2}} \quad (4)$$

r is the correlation coefficient ranging from 0 for no relationship between curves x and y , and 1 when x completely matches y . n is the number of sample points, and the variables with the bar are the means of each distribution. The denominator is the equivalent of the product of the standard deviations of the two distributions. r^2 is a measure of the amount of variation in one curve that is related to the other curve. The maximum correlation obtained with lagging time between signals of 16.7 ms is 0.8. This is sufficient to assert that the measured waveform has its source in the radiated signature of the transducer and not from the driving voltage EMR because the measured signal correlates to the predicted signal from vibration of the face of the transducer established by transducer performance characteristics and not to the square wave impressed voltage constituting the EMR. Consequently, this probe design is capable of resolving high frequency components of a transmitted ultrasonic signal that are likely needed in determining energy input to

sonochemistry mechanism models for ionization and polymerization as mentioned by Wu [1]. If much higher frequency components need to be resolved shrinking the physical PZT sensor may help. Alternatively a different PZT element with appropriate response range can be found. The movement of probe 1 closer to the source correctly shows a growth in measured signal amplitude. It can be seen in Fig. 10 that the characteristics of the two curves change when probe 1 is moved, even though probe 2 remains in the same place. This is the result of the change in the complex acoustic field in the tank caused by a different reflection environment emanating from the structure of probe 1 when in its new position, and is further evidence of the probe's spatial sensitivity.

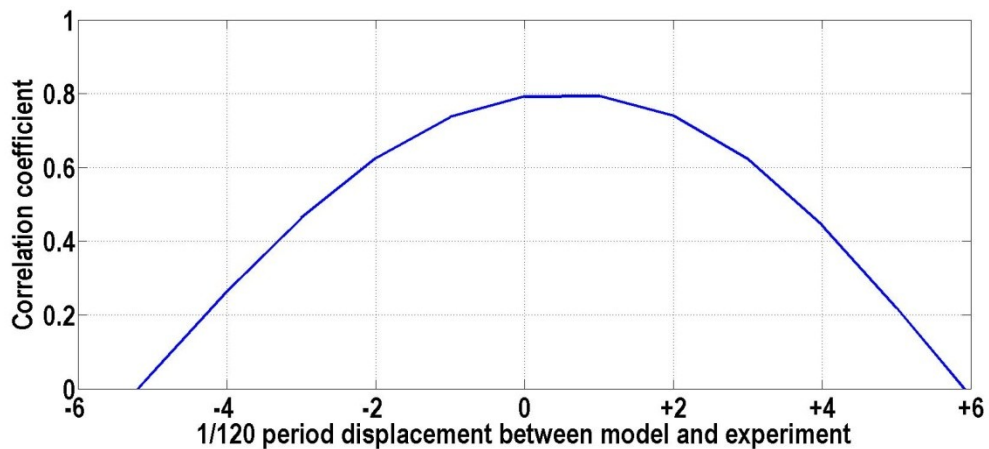


Figure 2.12. Correlation coefficient between the two waveforms in Figure 8 as a function of fractional period displacement between them.

Shielded vs. Unshielded Measurements

The grounded probe response in Fig. 7 shown in the callout is approximately 150 millivolts peak to peak. By contrast, the ungrounded probe signal is more than 5000 millivolts peak to peak when driven by a 50 V peak-to-peak driving signal. Furthermore, the unshielded probe signal in Fig. 7 is roughly the same square wave shape as the applied voltage to the transducer, and exhibits an integrated average phase which is constant because phase changes for the electromagnetic signal are too small to resolve.

Thus the grounded probe detects a complex acoustic signal that is .003 times smaller than the ungrounded signal generated by EMR.

The Discrete Fourier Transforms calculated for the 50 V_{pp} voltage driving signal, and the grounded and ungrounded probe signals reveal a series of sharp resonance peaks as expected from the Fourier series representing the spectrum of the square wave source. The normalized DFT of the ungrounded probe response shows the effect of processing the square wave voltage signal through both the radiating transducer and the probe's sensor while allowing the contribution from the dominant EMR emanating from the impressed high voltage driving signal. In doing this the ungrounded probe response removes the detail of the spectrum of the square wave broadcast signal from the radiating transducer thereby substantially removing acoustic field detail. By contrast, once the probe is grounded the detail of the broadcasted acoustic signal is restored as the peaks in the grounded DST demonstrate. Importantly, there is a difference in the spectrum of the broadcasted acoustic signal as measured by the grounded probe, and the spectrum of the

square wave driving signal before it passes through the radiating transducer. This is apparent in the difference in the peaks not including the 2 peaks near 40 kHz where coincidence is expected.

Phase as a Function of Position

In interpreting Fig. 11, it is known that Lissajous patterns on an oscilloscope will be inclined ovals, or circle patterns depending on the magnitude of the phase change for each major frequency component, while phase changes of only a few degrees will appear as an inclined straight line having a slope determined by the magnitude of the signals. The Lissajous patterns in Fig. 11 confirm that a significant phase change occurs between grounded probes when one is displaced relative to the other, and the phase change vanishes upon ungrounding of the Faraday cage. Examination of plot 11 (a) reveals that the slope of the major oval has passed 90 degrees indicating a phase shift in excess of a quarter wavelength. It is also seen that the Lissajous pattern for (a) is in millivolts while in (b) it is about 10 Volts across.

The phase changes shown in Figures 10 and 11 can be understood as follows: when the probes are separated by a significant fraction of the radiated acoustic wavelength, and when both are grounded, phase change should be observed in comparing their output. If both are ungrounded, the signal being detected will be dominated by EMR from the transducer driving voltage, and little phase change should be observed. This is because the transmitted EMR is electromagnetic radiation traveling at the speed of light having a very short wavelength given by equation 5.

$$\lambda = c / f \quad (5)$$

where λ is the wavelength in meters, c is the velocity of light and f is the signal frequency in cycles per second. Thus the wavelength of the electromagnetic signal is much shorter than the acoustic signal. Since the transmitted pressure wavelength is 3.7 cm, a phase shift for an ~ 2 cm displacement would be near one half of a wavelength. Inspection of Fig. 10 shows the phase shift of probe 1 which was moved approximately 2 cm closer to the source has a phase shift to an earlier time of about a half wave when comparable features of the two signals are examined (see arrows). The starting point of the curves will shift between figures due to the triggering point of the oscilloscope.

Conclusion

A submersible ultrasonic acoustic pressure probe is presented and characterized which is designed for making pressure measurements in fluids near a strong source of electromagnetic radiation. It is significantly isolated from electromagnetic signal contamination from the high voltage driving signal of the ultrasonic source because it employs shielding from a separately grounded Faraday cage. The efficacy of this shielding, and the sensitivity of the probe, is examined and proven by test cases. The first experiment shows that the probe can resolve the detail of a complex acoustic field according to theory, the second experiment demonstrates measurable difference in amplitude, frequency and phase from grounding compared to ungrounded designs, while the third experiment proves the probe is responding to the acoustic signal, not the EMR, by comparing phase changes.

An apparatus and method for calibrating the probe is developed and tested based on an instrumented force measuring beam which can be submersed into the same liquid environment. This beam is made from a copper strip onto which a narrow strain gauge is bonded, and having a pressure force target matching the probe's active element. Response of the beam to both gram weights, a static load, and to the dynamic load from the signal to be tested comprises a calibration method to produce a sub-standard from which the probe itself may be calibrated. Sub-standards may be created for each test frequency of interest.

It is seen that the probe is able to record waveform changes resulting from path differences on the order fractions of a wavelength. This can be useful in experiments in which the details of field exposure needs to be resolved. Furthermore, the effective isolation of a probe by a grounded Faraday cage so as to better characterize an acoustic field level can be very important in determining dose from ultrasonic exposure. Without adequate isolation there is the possibility of overestimating ultrasonic dosage.

Subsequent to this work, the author's laboratory has successfully miniaturized this design using a 5 mm active element encased in a metal connector shielded by screen wire to comprise the Faraday cage. The resulting small detector is suitable for insertion in small volumes where knowledge of pressure fields is important to understand system behavior. This probe design also has applications in small volume systems like sonochemical material manufacturing and protein degradation work in medical and food applications.

References

1. Wu, C.I., et al., Ultrasound ionization of biomolecules, *rapid commun mass sp*, 24(17), p. 2569-2574, (2010).
2. Edwards, J., et al., Effect of ultrasonic cavitation on protein antigenicity, *J. Acoust. Soc. Am*, **59** (6), p. 1513-1514, (1976).
3. Marchioni, C., et al., Structural changes induced in proteins by therapeutic ultrasounds, *Ultrasonics*, 49, (6-7): p. 569-576, (2009).
4. Gulseren, I., et al., Structural and functional changes in ultrasonicated bovine serum albumin solutions, *Ultrason. Sonochem.*, 14(2): p. 173-183, (2007)
5. Suslick, K., et al., Characterization of sonochemically prepared proteinaceous microspheres, *Ultrason. Sonochem.*, 1 (1), p. s65-s68, (1994).
6. Gedanken A., Using sonochemistry for the fabrication of nanomaterials, *Ultrason. Sonochem.*, 11, I 2, p. 47-55, (2004).
7. Aurbach, D., Nanoparticles of SnO Produced by Sonochemistry as Anode Materials for Rechargeable Lithium Batteries, *Chem. Mater.*, 14 (10), p. 4155–4163, (2002).
8. Shariat-Panahi, S. et al., Design and test of a high-resolution acquisition system for marine seismology, *IEEE Instrumentation & Measurement Magazine*, 12, I2, p. 8 – 15, (2009).

9. Felizardo, M. et al., Improved acoustic instrumentation of the SIMPLE detector, *Nucl Instrum Methods*, 585, p. 61-68, (2008).
10. Soudagar, S.R., Samant, S.D; Semiquantitative characterization of ultrasonic cleaner using a novel pressure intensity probe; *Ultrason. Sonochem.*, 2 No 1, p. s49-s52, (1995).
11. Bushberg, J., et al., *The Essential Physics of Medical Imaging*, 2nd Ed., Lippencott Williams & Wilkins, Philadelphia, PA., p. 484, (2002).
12. Martin C J, Law A N R, Design of thermistor probes for measurement of ultrasound intensity distributions, *Ultrasonics*, **21**, I2, p. 85-90, (1983).
13. Pugin, B.; Qualitative characterization of ultrasound reactors for heterogeneous sonochemistry; *Ultrasonics*, 25 (1), p. 49-54, (1987).
14. Durkee, J; Management of Industrial Cleaning Technology and Processes; 1st ed., 2006, *Elsevier*, p. 368.
15. Witte R.S. et al., Inexpensive acoustoelectric hydrophone for mapping high intensity ultrasonic fields, *J. Appl. Phys.*, 104, p. 054701 1-3 (2008)
16. Morse, P.M., Ingard, K.U.; *Theoretical Acoustics*; McGraw-Hill Book Company; New York, p. 381, p. 269, (1968)
17. Lewin P.A., Sensitivity of ultrasonic hydrophone probes below 1 MHz,

- Ultrasonics*,. 38, p. 135-139, (2000).
18. Ultrasonic Power Output Measurement by Pulsed Radiation Pressure; *j res natl inst stan*; 101, Number 5, p. 659-669, (1996)
 19. Ziskin M.C., Lewin P.A., *Ultrasonic Exposimetry*, CRC Press, p. 133, (1993)
 20. Beranek, Leo, *Noise and Vibration Control*, McGraw-Hill Book Company, p. 15, (1971)
 21. Chen, H. et al., Blood Vessel Deformations on Microsecond Time Scales by Ultrasonic Cavitation, *phys rev lett* 106, 034301, p. 106, (2011).
 22. Miki Y., Acoustical properties of porous materials-Modifications of Delany-Bazley models, *J. Acoust. Soc. Jpn.*, p. 21, (E) 11, 1 (1990)
 23. Fisher, R.A., *Statistical Methods for Research Workers*, 6th ed. Oliver and Boyd, Edinburgh, p. 185, (1936)

Chapter Three: A thermodynamics approach to air in water pulsing bubble growth

Introduction

Rectified heat transfer into insonated vapor bubbles around boiling has been extensively analyzed by Wang [1], Patel [2] and Hao [3], and discussed in general by Ashokkumar [4]. Wang established the detailed theory to describe heat and mass transfer into bubbles as a result of evaporation cycles in an oscillating bubble. Patel *et al.* studied this effect in liquid helium where the vapor in helium is devoid of foreign gases so the effects could be quantified without contamination. Hao and Prosperetti pursued the contribution to this phenomena by bubble translation, and the resulting increase in convective heat transfer. As a result, they discovered that bubble velocity can cause bubble growth or destabilization over a narrow velocity range in sub-saturated near-boiling conditions. Ashokkumar gives an overview of bubbles in an acoustic field, and along with his colleague, Leong [5] worked on the additional effects of surfactants which were found to promote bubble growth by rectification. Frequently, however, the influence of thermal diffusivity within the bubble is neglected because the bubbles studied were

small compared to the insonating wavelength. Moreover, these studies were limited to vapor bubbles which may not be applicable to a broad range of industrial applications.

The current work investigates the approach of predicting air bubble growth and shrinkage in terms of rectified heat transfer utilizing a simple thermodynamic method which appears to agree well with experiments when evaporation and condensation are not a factor. The model is used to explore non-vapor bubble behavior of large sizes (i.e., 0.1 to 1 mm) rising in water, a regime not examined previously. This regime of bubble behavior is of interest in applications such as aeration [6], food processing [7] and dissolving foams [8], where managing bubble size is important in sub-boiling processes. Other areas of interest concern the injection of air bubbles of controlled size for the purpose of managing droplet size following flashing in spray systems [9] or waste removal [10].

Objective

The objective is to determine if the size of air bubbles in sub-boiling processes can be manipulated using selected frequencies of ultrasonic insonation. This will be explored using a simplified, application oriented, model validated by experimental measurements.

Method

Bubble growth and shrinkage are obtained from experiments done in water aquariums in which a bubble generator is placed in the center and near the bottom of the

tank. Bubble generation is accomplished by forcing air through a short section of 1.6 mm stainless steel tubing having an 0.18 mm I.D. Most experiments on the 6-20 cm/s rising stream of air bubbles were insonated by ultrasonic transducers located 23 cm from the bottom and in the center of the tank. The bubble generator was isolated from acoustic radiation by placement of a long stem glass funnel over it. In this way, the bubbles emanating from the 1 cm stem are insonated and not the bubble generator itself since the stem diameter is much smaller than a wavelength. Field pressure levels were measured around this radiator that were used in modeling.

The size change and velocity of insonated rising air bubbles was done from ImageJ analysis of photographs taken by two burst mode cameras: a Casio Exilim at 40 fps, and a 14 Mpx Panasonic DMC-FZ100 at up to 60 fps. The exposure times were 1/2000-1/4000 seconds as needed for image analysis. Positive identification of individuals is done from 6 contiguous frame montages. Rasband at NIH [11] has placed ImageJ, V 1.45, in public domain software. Population size analysis was done from ImageJ scripted group photograph studies of pictures made by an Olympus E-510, 10 MPx camera with a 50 mm Zuiko lens equipped with an Olympus A-macro lens and using an extender when needed. Photographs were back-lighted by up to 1500 W combined incandescent and florescent illumination through a finely sandblasted glass diffuser screen.

Insonated bubble size changes captured by experiments are examined using explicit numerical analysis modeling developed from thermodynamic first principles coupled to an empirical correlation to determine convective heat transfer.

Mass Change

The change in mass predicted by the modeled volume likely is contributed by mass diffusion. The transfer of mass through a pulsating surface area has been theoretically analyzed extensively by Wang [1]. He estimates the contribution from all mechanisms of rectified mass transfer for a nitrogen bubble in 20 C water being insonated at 10 kHz in terms of bubble size (see Figure 6, p. 1140). For a bubble size of 0.4 mm, this is an addition of $\sim 10^{-9}$ gm/cycle, and is proportional to the square for the acoustic field intensity in bars. In our case field intensity is $\sim 1/10$ bar leaving the magnitude of the effect to be $\sim 10^{-11}$ gm/cycle. Assuming exposure of 1 second to the maximum field of 10 KHz this becomes a contribution of 10^{-7} gm (this is unlikely as the field varies between nodes and antinodes). The mass of a 0.4 mm radius bubble is $\sim 2.7 \times 10^{-7}$ gm. Thus, a conservative estimate for the upper limit on bubble growth would be equivalent to a 11% growth in radius. It's noted that in our work for fields $\leq 1/10$ bar the maximum growth seen was $\sim 12\%$. Thus, it's reasonable to conclude that the mass influx predicted by the constant density volume growth in our simplified model is due largely to rectified mass transfer. The confirmation of this mechanism near resonance was studied in this work by conducting identical experiments in degassed and plain water.

Farther from resonance, there are three additional mechanisms for the addition of the much smaller mass changes found in our studies:

Hsieh and Plesset have provided an approximation of the mass flux into a bubble due to pressure pulsation [12]:

$$\frac{dm}{dt} = 8 \frac{\pi}{3} DCr \left(\frac{\Delta P}{P_0} \right)^2 \quad (1)$$

This expression has been solved for values of the variables typical of our experiments. The resulting radius change from equation (2) for a 0.2 mm radius bubble was found to be ~1.7 %. This change is consistent with our observations of bubble growth farther from resonance.

Mass transfer associated with bubble shrinkage also occurs by convective diffusion in a non-pulsing bubble. This effect was approximated as follows: Consider a 0.1 mm air bubble rising in water in the absence of a forcing field such that convective effects dominate. The concentration of air in the water immediately surrounding the rising bubble is being refreshed. The mass loss can be approximated as a convective mass transfer process in which the rate of mass loss, \dot{m} , is determined by Fick's law of diffusion:

$$\dot{m}_{conv} = h_{mass} A_s (C_s - C_\infty) \quad (2)$$

The mass loss for a small bubble can be estimated once the mass transfer coefficient is known along with the air to water interface concentration. h_{mass} is obtained from the Sherwood number as a function of the Schmidt number. Levich [13] gives the Sherwood

equation, the Schmidt number comes from the definition of the Lewis number [14]. The air/water concentration at the bubble surface can be calculated from the atmospheric pressure at the surface (water depth neglected) minus the partial pressure of saturated water vapor at 293 K divided by Henry's constant at this temperature, 62900. Taking the air concentration in the water as zero, maximum shrinkage rates can be approximated for a small bubble rising at 13 cm/s (a typical value in our experiments) having a Reynold's number around 50. The mass transfer radius change in this low velocity case is around 0.2% over 5/40 second . Thus shrinkage rates due to convective mass transfer are not a major factor in this study.

Mass transfer by stationary diffusion also exchanges a small quantity of mass. Epstein and Plesset [15] investigated stationary bubble diffusion shrinkage in undersaturated water, and growth in supersaturated water. They found that for a bubble of 0.1 mm radius in 50% saturated water including surface tension effects, it takes 241 seconds for the bubble to completely dissolve. Therefore, this mechanism also contributes only a small amount in the time frames studied which is limited to a maximum of 7/40 seconds.

Lastly, size change by hydrostatic growth was considered. Bubbles expand when rising in a hydrostatic pressure field in which the pressure is diminishing by $g \rho \Delta h$. For air bubbles rising only 10 cm (the height of the analysis zone) in water this effect is small. Cerza [16], for example, shows this effect to be much less than 1% of the original radius for sizes comparable to those studied.

Details on the thermodynamic modeling design, and on the experimental setup are presented in the sections which follow.

Modeling

Mathematical modeling of the effects of insonating bubbles is desirable in order to predict bubble change when exposed to acoustic fields at frequencies and power levels not tested by experiment. Experimental data from testing can be used to validate a model so that its forecasts are reliable. Conventionally, bubble models have been based on variations of Rayleigh-Plesset. The RPNNP version of Rayleigh-Plesset [26, p. 302-306] that includes viscosity, equation (3), and two variations of it, Cox [27] and Gehrke [28], were studied at frequencies of 27.5, 28 and 28.5 kHz to determine if these models could be used as predictors.

$$R\ddot{R} + \frac{3\dot{R}^2}{2} = \frac{1}{\rho} \left\{ \left(p_0 + \frac{2\sigma}{R_0} - p_v \right) \left(\frac{R_0}{R} \right)^{3\kappa} + p_v - \frac{2\sigma}{R} - \frac{4\eta\dot{R}}{R} - p_0 - P(t) \right\} \quad (3)$$

In equation (3) R is bubble radius, m, p_0 and p_v are air and water vapor partial pressures, Pa, σ is surface tension, N/m, ρ is density of water, kg/m³, $p(t)$ is the acoustic pressure as a function of time, Pa, κ is the polytropic constant and η is the shear viscosity.

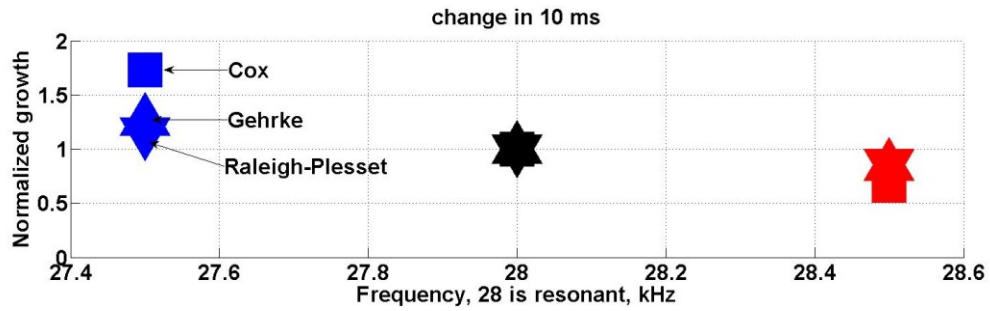


Figure 3.1 Normalized bubble growth and shrinkage predicted by Rayleigh-Plesset when the magnitude of the acoustic signal is 100 Pa.

Predictions of bubble behavior using variations of Rayleigh-Plesset as plotted in Fig 3.1 follow experimental trends as established in this work, however, in order to approach experimental bubble change values, unrealistically small forcing pressures were required since these equations yield very large bubble radius excursions within a few cycles. For this reason, an application model was undertaken based on similar reasoning to that used to develop the Rayleigh-Plesset equation: Conservation of work done on the bubble by the compression of the acoustic pulse is converted to a heat pulse which leads to a temperature and volume change through a non isentropic form of the Gibbs equation as detailed in this chapter. While this model determines volume change of the insonated bubble as a heat transfer problem, and does not explicitly model mass flux, the association between heat and mass transfer is well established and is accounted for by the entropy associated with using the polytropic constant as opposed to the ratio of specific heats.

Kays [17] presents the following rationale for associating a mass flux into a bubble resulting from temperature gradients. Drawing a control volume enclosing an air water interface, Fig. 2, an energy equation can be written in terms of enthalpy, i ,

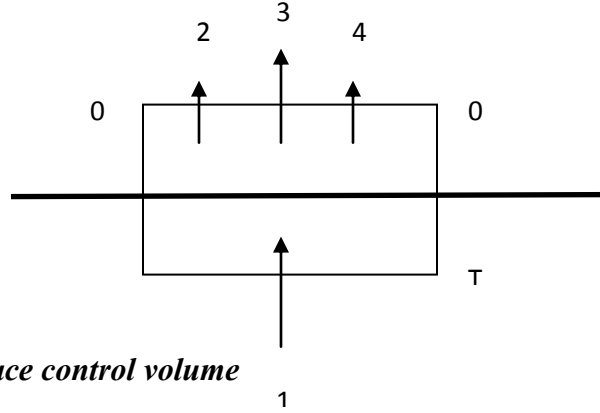


Figure 3.2 Bubble in water, surface control volume

producing a balance of the form, term 2-term 3-term 4-term 1=0 given by equation 4 below.

$$\dot{m}_{total}i_0 - \sum_j \left(\gamma_j \frac{\partial m_j}{\partial y} \right)_0 i_{j,0} - \left(\Gamma c \frac{\delta t}{\delta y} \right)_0 - \dot{m}_{total}i_{T=0} = 0 \quad (4)$$

wherein \dot{m}_{total} is the total mass at the interface $\text{kg}/(\text{m}^2 \text{ s})$, i_0 is the static enthalpy evaluated on the 0-0 side of the control box, j indexes the species, γ_j is the mass-diffusion coefficient for substance j in a mixture $\text{kg}/(\text{m s})$, m_j is the mass of the j th component (kg), i_j the enthalpy of the j th component crossing 0-0, Γ is the thermal diffusion coefficient $\text{kg}/(\text{m s})$, c the specific heat at constant pressure, $\text{J}/(\text{kg K})$, t is temperature, K , i_T is the static enthalpy crossing T-T. The importance of equation 3 to the modeling development that follows is the association of a change in mass flux with thermal diffusion into the bubble. Our model predicts a volume change (bubble radius change) which in turn

specifies a mass flux since the temperature and density are held constant. The feasibility of this association is anticipated by equation 3. It will be seen that the mass flux predicted by our model is in accordance with the work of others (notably Wang) in which the mass flux term is explicitly described in their work while being inferred in ours.

The modeling employed in this work is explicit, energy balanced, finite difference numerical analysis that includes thermal diffusivity governing heat penetration through the wall of the bubble. The oscillations of the bubble are determined by considering it to be a mass on a spring having a spring constant proportional to its surface tension [18]. Transmissibility calculations [19] govern the effectiveness of the applied acoustic force to displace the wall of the bubble as a function of the driving frequency. The bubble's resonant frequency is determined by Minnaert's equation [20], and the damping coefficient is assumed to be the value reported in the literature [21]. Phase calculations are done as a function of frequency and damping. The magnitude of the heat pulse is determined by adiabatic compression that converts the pressure change to temperature. Every half cycle of modeled bubble oscillation the bubbles' excess temperature gain, or loss, is converted back to volume change adiabatically, and the new bubble size is used to recompute the magnitude of the thermal pulse from acoustic work. The heat transferred to and from the fluid in this process is determined using a heat transfer coefficient computed from the Whitaker correlation [22] for a moving sphere as a function of Reynolds number, Prandtl number, and viscosity. This is calculated at each iterative time step. Following are the details of this process most of which can be found in [14].

Heat transfer in and out of an air bubble in water is governed by the heat equation for temperature, u , a function of space and time.

$$\frac{\partial u}{\partial t} - \alpha \nabla^2 u = 0 \quad (5)$$

Equation 5 was first solved by Fourier using separation of variables in which time is replaced by dimensionless time, τ , given by:

$$\tau = \frac{\alpha t}{r^2} \quad (6)$$

where α , the thermal diffusivity, is defined as equation (7) (Liebermann gives a slightly higher value, 2.9E-5, than is computed by (7) [23]):

$$\alpha = \frac{k}{\rho c_p} \quad (7)$$

Thus, we see characteristic thermal transport time (τ) is limited by thermal diffusivity, equation. The penetration time for a heat pulse to travel the radius of a bubble is approximated by [22]:

$$t = \sqrt{\frac{r^2}{\alpha}} \quad (8)$$

Due to the scale of applying this to small bubbles with high frequency excitation, explicit numerical analysis is needed. A spherical bubble is modeled composed from

concentric shells with nodal surfaces bounding each shell, and the surface node being a half shell.. The energy balance method is applied to each node.

$$\Delta t \sum_{allsides} \dot{Q} = \Delta E_{element} \quad (9)$$

The heat transferred into any nodal element in an incremental time from its neighboring shells is given by Fourier's law of heat conduction (10) when considering internal nodes; and also includes Newton's law of cooling for the convective surface node (11). The sum of these drive the temperature change of that element's mass through its specific heat.

$$\dot{Q} = -kA \frac{dT}{dr} \quad (10)$$

$$\dot{Q} = hA(T_s - T_\infty) \quad (11)$$

Therefore, in a time step the model iterates over equation (12) for each successive internal node, and terminates by solving equation (13) for the surface node.

$$kA_{ns}(n-1) \frac{(T^i(n-1) - T^i(n))}{dr} + kA_{ns}(n) \frac{(T^i(n+1) - T^i(n))}{dr} = \rho A_{ns}(n) c_p dX \frac{(T_n^{(i+1)} - T_n^i)}{dt} \quad (12)$$

$$kA_{ns}(n-1) \frac{(T^i(n-1) - T^i(n))}{dr} + hA_{surface} (T_{surface}^i - T_{heatpulse}^i) = \rho A_{surface} c_p \frac{dX}{2} \frac{(T_n^{(i+1)} - T_n^i)}{dt} \quad (13)$$

The selection of the time step is dictated by properly resolving the cyclical temperature pulse resulting from the compression work done on the bubble by the sinusoidal acoustic insonation. To properly resolve this pulse, a time step was selected allowing the pulse to be sampled at least 20 times in a period. Large time steps result in an oscillatory behavior of the solution within a second. Therefore modeled results were limited to those possessing time steps smaller by at least a factor of five from the onset of instability. It is worth noting that the usual tests for time step size which are functions of Fourier and Biot numbers result in time steps that are too large for long term stability due to the high frequency heat pulse.

A bubble wall displacement is determined from equation (14), modified by the transmissibility factor, equation (15).

$$dr = \frac{P_a}{8\pi\sigma} \frac{P_{atm}}{\sigma} \quad (14)$$

$$\frac{F_T}{F} = \frac{\sqrt{1 + (2\xi \frac{\omega}{\omega_r})^2}}{\sqrt{\left[1 - (\frac{\omega}{\omega_r})^2\right]^2 + (2\xi \frac{\omega}{\omega_r})^2}} \quad (15)$$

This bubble wall displacement produces an adiabatic pressure change resulting in a temperature pulse determined from $dT = T_2 - T_1$ where T_2 is found from (16), and γ is the polytropic constant established by Crum [24].

$$T_2 = T_1 \left(\frac{P_2}{P_1} \right)^{\left(\frac{\gamma-1}{\gamma} \right)} \quad (16)$$

The varying operative term of internal bubble pressure resulting from surface forces are computed from:

$$P_i = \frac{2\sigma}{r} \quad (17)$$

In model iterations the application of the heat pulse is applied to the bubble as it pulses. Both are varying according to a cosine wave whose frequency is determined by the acoustic signal. The phase of the application of the acoustic force is computed from:

$$\tan \phi = \frac{2\zeta \left(\frac{\omega}{\omega_r} \right)}{\left(1 - \left(\frac{\omega}{\omega_r} \right)^2 \right)} \quad (18)$$

The resultant phase difference between bubble oscillations and the applied force (and temperature pulse) shifts from $\phi=0$ to $\phi=180^\circ$ when crossing the bubble's resonant frequency.

At the end of model iterations for a half cycle of the applied force, a new radius is computed by allowing the bubble to adjust size polytropically:

$$V_{new} = V_{initial} \cdot \left(\frac{T_{newaverage}}{T_{initial}} \right)^{\left(\frac{1}{1-\gamma} \right)} \quad (19)$$

where the new r is extracted from V_{new} , and γ is 1.2.

Using the new bubble surface area determined by the new radius, a revised acoustic force is computed leading to a revised distance increment which yields a revised temperature pulse.

The Reynolds number is first computed according to (20) which permits calculation of the Nusselt number from the Whitaker correlation (21) that, in turn, yields h from the definition of the Nusselt number (22) which is used in equation (13).

$$Re = vel \frac{D}{\nu} \quad (20)$$

$$Nu = 2 + (0.4 Re^{0.5} + 0.6 Re^{0.667}) Pr^{0.4} \left(\frac{\mu_{\infty}}{\mu_{surface}} \right)^{0.25} \quad (21)$$

$$Nu = \frac{hD}{k} \quad (22)$$

In the equations above the difference in using the polytropic constant and the ratio of specific heats (the isentropic case) accounts for the entropy created by heat and mass transfer.

Experimental studies of bubble size change

Experimental apparatus

Experiments on insonated 0.2 to 0.6 mm radius rising air bubbles in water generated using a bubble pipe were conducted in a 40 L hexagonal aquarium as shown in Fig.3.3. Nearly mono-disperse bubble columns were produced by the bubble pipe pictured at the bottom. Fig. 3.4 shows insonation on rising air bubbles from the bubble pipe formed in acoustic isolation, then rising through a 10 kPa, 6 kHz acoustic field. Acoustic isolation was achieved using an inverted glass funnel placed a sufficient distance from the acoustic source. Both acoustic pressure measurements and bubble behavior (data not shown) confirm negligible effect on bubble size in the base of the funnel, only becoming minor at its outlet. The rising bubbles emanating from the 1 cm funnel stem were insonated by both a two transducer array, and by the four transducer array of 14 mm PZT disk radiators mounted on microscope slides shown in the figure. The arrays were always operated in-phase.

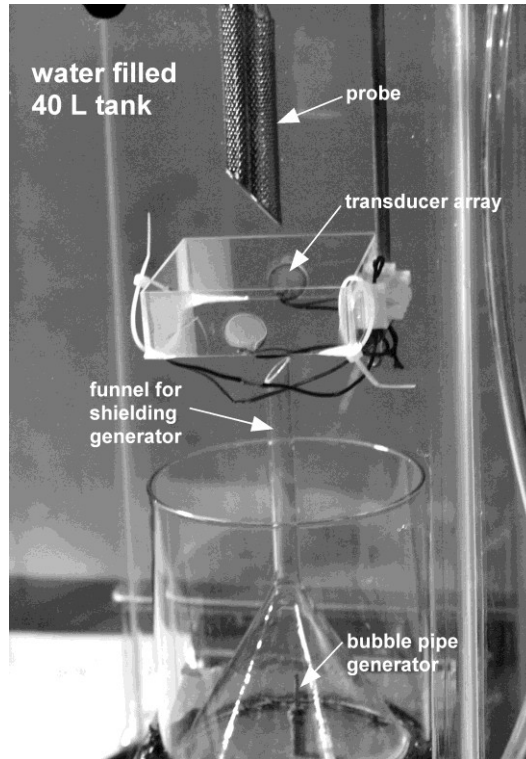


Figure 3.3. Experimental setup for the study of individual air bubble size change resulting from ultrasonic insonation.

Typically, the insonating transducers were driven by a 100-110 V_{pp} continuous sine wave signal output from a Vs 1100 Crest audio amplifier having a 2 V_{pp} input signal from a Leader LAG 1208. Current to the transducers was measured to be approximately 0.32 amps thereby producing about 32 Watts electrically into the transducer array. The generated acoustic field measured an average of 0.9-1.0 V_{pp} using the acoustic probe which eliminates radiated EMI from the 100 V insonation array located just centimeters away in the water [25]. The probe measurements indicate varying pressure levels of 4 to 7 kPa when operating between 4 and 8 kHz that are produced from the highly reflective

environment caused by the glass walls of the aquarium. Fields of this pressure level are near acoustic thresholds thought to influence bubble growth when experimenting with vapor bubbles [2].

In experiments performed to capture bubble change when subjected to insonation by frequencies from 4 to 8 kHz, many hundreds of sequential pictures were taken. Fig. 3.4 shows an example of these photographs separated by 1/40 second. These photographs are then processed in ImageJ for quantification of bubble growth and shrinkage. The general procedure for sizing bubbles is: (a) open a photograph in ImageJ, (b) calibrate based on measuring a known linear dimension, (c) crop a zone to be analyzed, (d) subtract background, (e) convert to 32 bit monochrome, (f) transform to binary, (g) invoke *analyze particles* which determines area of each circular object based on a user-determined circularity threshold, repeat in a programmed loop until the sequence is processed. Calibration needs to only be done once per set. Once an area dataset file is made the radius is calculated in Matlab.

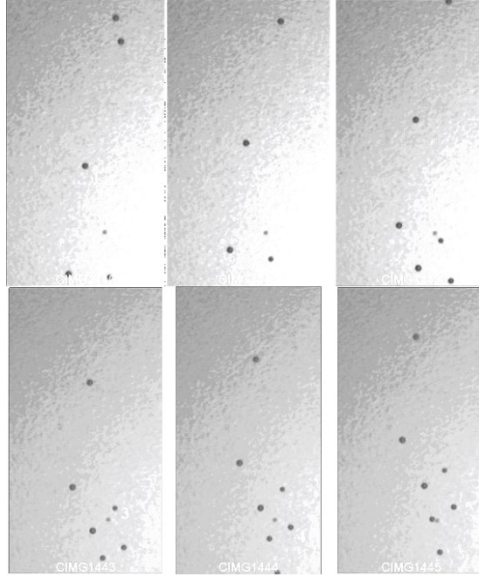


Figure 3.4. Typical bubble photographic montage used to track and quantify bubble size and population changes.

Measured bubble size change.

Individual bubble traces were studied for size change over 6 frames (6/40 seconds) to quantify growth or shrinkage as a function of initial bubble radius, and insonation frequency. The growth of a 0.43 mm radius bubble insonified by 6 kHz compared to the shrinkage of a 0.51 mm radius bubble insonated by 8 kHz is reported in the results section.

In addition to measurements of individual bubble size change when insonified at different frequencies, experiments were done to quantify population change resulting from insonation near resonance. Photographs of a rising bubble stream from the bubble

pipe were made at 0, and 4-8 kHz. Except for the no field case, 0 kHz, the transducer array was driven at 100 V_{pp}.

Experiment to study growth in degassed water.

This experiment studies insonified bubble growth and shrinkage of initially the same sized bubble in degassed water and again in plain water at 20 C when exposed to a 10 kHz acoustic field. The purpose is to determine if the effects of insonation are noticeably different when performed in degassed water because the absence of dissolved air would reduce mass transfer in the expansion phase. Shrinkage, however, might still occur due to the concentration gradient in the contraction phase of the pulse. Thus, a confirming factor is whether significant growth is still observed when experiments are repeated in degassed water.

Plain water was degassed at 20 C in a vacuum chamber evacuated to 22 inch Hg for 30 minutes. ~0.2 mm rising air bubbles were produced from the same bubble pipe and insonated by a forcing field generated from 44kHz transducers driven by a continuous sine waves at 10 kHz. The driving signal was produced by the same signal generator, audio amplifier and impedance matching devices as were employed in all the other experiments. Two experiments were performed: The first was done in degassed water, the second in plain 20 C water. In both, the bubble pipe was inserted into the test cell immediately before the experiment was done so as to minimize aeration. For one set of bubbles having an initial radius of 0.27 mm the bubble stream was insonated at 10 kHz from the side at a distance of 2 cm by a disk transducer where the acoustic probe detected

a strong field of 72 kPa. For the second set of bubbles initially 0.29 mm in radius insonation came from a ring transducer surrounding the pipe emitter and producing a 30 kPa field. A sequence of high resolution pictures were made. This was then repeated in plain water. The collection of pictures, insonated and non-insonated were then analyzed by ImageJ for size growth, and the results are reported in the next section.

Results and discussion

The experimental data was first used to validate the simplified model. Then the model and experiments were utilized to explore the hypothesis that insonation alters bubble size distributions. Before interpreting the results of insonating bubbles at different frequencies in the large aquarium, it is informative to examine field profiles along the line of flight of the bubbles studied at the same frequencies.

Acoustic profiles in test tank

The acoustic field profile for the 4 to 8 kHz bubble exposure experiments was surveyed at the same transducer array power and at 6 and 44 kHz (continuous sine wave). The former representing the approximate field strength variation as seen by the bubbles studied, while the latter matches the higher frequencies examined in the acoustic probe ray tracing discussed in Chapter 2. The field strength along four points of the vertical path travelled by the bubbles for the two survey frequencies was extracted from the continuous experimental data and is plotted in Fig 5. The experimental setup for this acoustic field survey is shown in Fig. 3.5 with labels marking the four survey points.

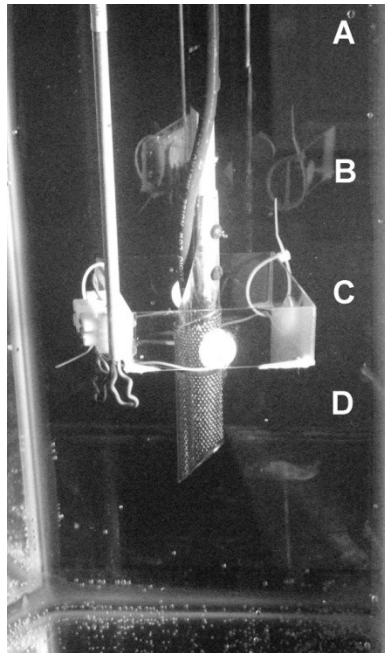


Figure 3.5. Acoustic field survey setup.

To record field strength as a function of position the acoustic probe was attached to a wand held by a laboratory clamp attached to a ring stand. This permitted raising the probe along the central vertical axis of the 4 transducer array. The signal trace from the probe was displayed on a Tektronics oscilloscope, and was continuously recorded by a digital microscope camera. The video files from these recordings were displayed in Microsoft Movie Maker allowing snapshot pictures to be made at the A-D positions. The probe was calibrated using the force beam method discussed in Chapter 2.

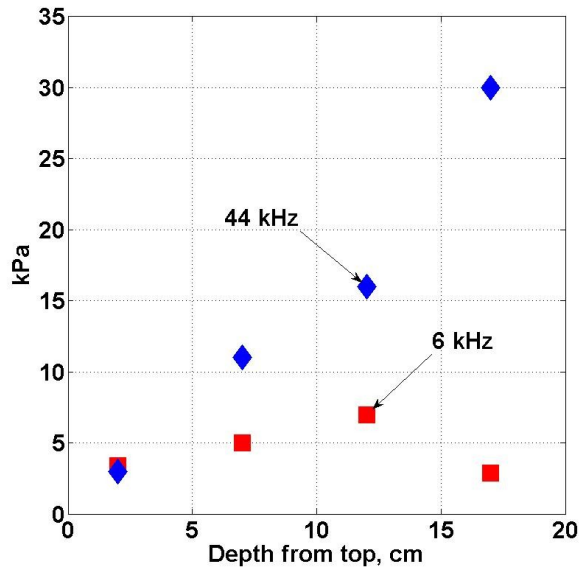


Figure 3.6 Acoustic field strength along the vertical axis of the 4 element transducer array as was used to measure bubble response to 4-8 kHz stimulus.

Examination of the field strengths plotted in Fig 3.6 show a large field intensity (proportional to amplitude squared) variation at 44 kHz due to the shorter wavelength resulting in enhanced interference from the walls of the test aquarium. Location C corresponds to the near field of the array. The field intensities associated with 6 kHz which is in the mid-range of the bubble studies show almost no variation in the farther field of the array where the bubble studies were done, and only a factor of two spanning the survey range.

Model validation experiments in plain water

The behavior of isolated bubbles in an acoustic field in plain water was studied to validate the simplified model. Measurements of air bubble growth and shrinkage by insonation at 8 kHz at a level of 5 kPa produced bubble changes up to 12% within 5/40 seconds as seen in Fig. 3.7.

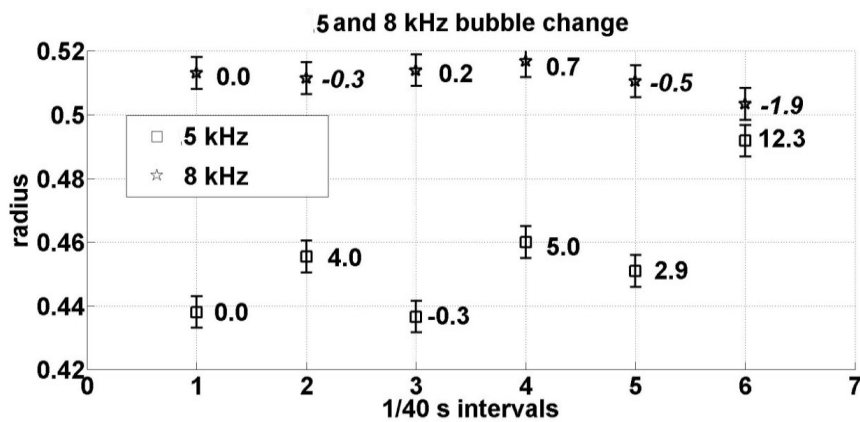


Figure 3.7. Bubble growth of 12.3% in 14 mm when insonated at 5 kHz, and shrinkage of -1.9% when insonated at 8 kHz over a distance of 21 mm.

Model predicted bubble size variation as a function of time and forcing frequency for the data in Fig. 3.7 falls within anticipated experimental errors (Fig 3.8).

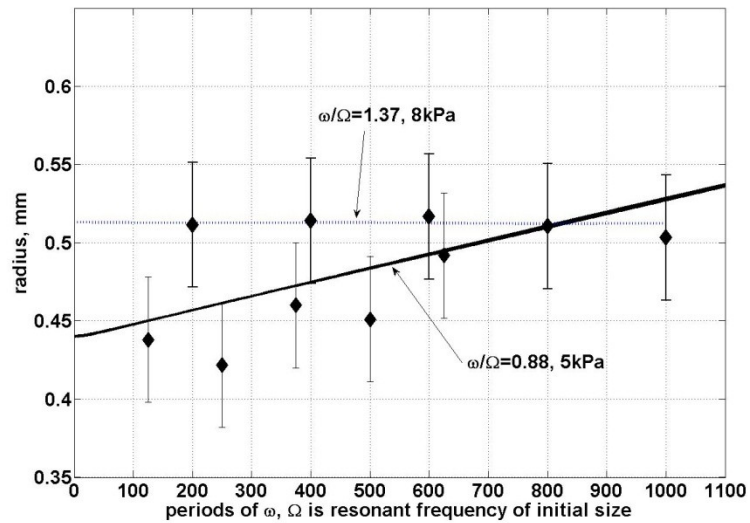


Figure 3.8. Bubble growth when insonated at 5 kHz, $\omega/\Omega = 1.37$, and shrinkage when insonated at 8 kHz, $\omega/\Omega = 0.88$, over a distance of 21 mm. (Data points from Fig. 3) compared to the model prediction.

In Fig. 3.8 the data points of Fig. 3.7 are plotted by frequency ratio, ω/Ω (insonation frequency/bubble resonant frequency), and exposure time as expressed in periods of the insonation frequency. The error bars on the data points represent a very conservative value of $\pm 10\%$ of radius associated with pixel resolution in this analysis procedure. The correspondence between the data and model values confirm the model since the 0.44 mm bubble exposed to 5 kHz grows to the value predicted within the error bar, while the 0.52 mm insonified by 8 kHz shrinks to the value predicted.

Bubble growth in degassed water

The results of the experiments to study bubble growth in degassed water compared to growth in plain water are shown in Fig. 3.9. Growth attributable to the ejected bubble having a higher pressure than its surroundings is discounted for two reasons: first if it were the result of an expanding pressurized bubble then the growth with and without the field would be similar which is not the case as this has been checked repeatedly, secondly if this were the case then bubble growth in degassed and plain water would be the same. This is also not the case.

In Fig. 3.9 two sets were chosen that had the exact same initial radius, and whose resonant frequencies were slightly above the insonation frequency of 10.2 kHz so growth would be expected. One set had an initial radius of 0.27 and a natural frequency of 11.0 kHz, the other was initially 0.29 mm with a corresponding natural frequency of 10.4 kHz

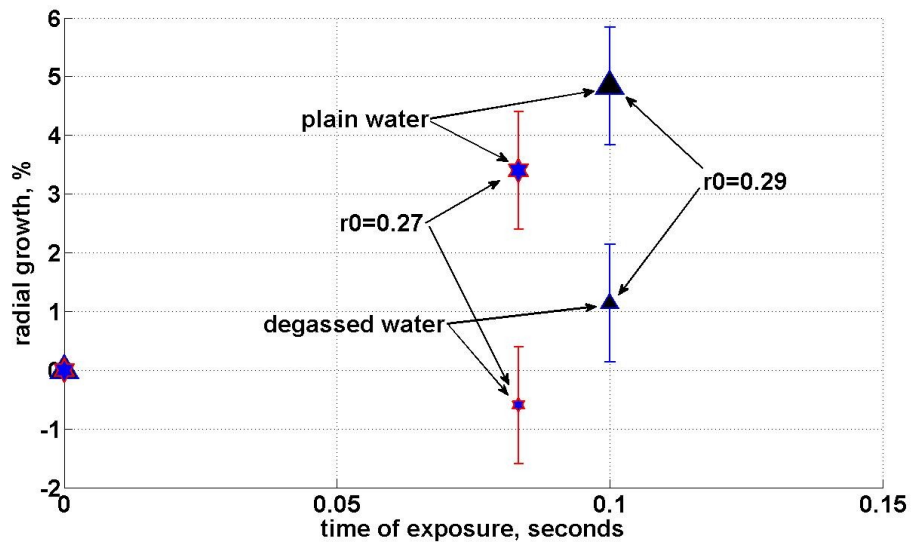


Figure 3.9. Bubble growth in degassed 20 C water compared to growth in plain water. Bubbles were the same size to start, error bars are $\pm 1\%$ reflecting error in size resolution by ImageJ processing.

It is seen in Fig. 3.9 that the acoustic field induced bubble growth of the 0.29 mm radius pair which have a natural frequency nearer the 10 kHz insonation frequency exceeded the growth of the 0.27 mm radius pair further in frequency away even considering conservative error. It is also seen that growth in plain water was up to 5 times that in degassed water. This verifies that the concentration of dissolved air in the water limits bubble growth as would be expected if this mechanism is a dominant source of mass change near resonance.

Mean population shift caused by insonation

The effect of insonating a nearly mono-disperse bubble stream at frequencies just below the population mean are presented in Fig. 3.10. The non-insonated bubble stream has a mean resonant frequently centered around 6.7 kHz as shown in the top graph. Insonation at 6060 Hz of the stream is plotted in the center, while insonation at 5060 Hz is plotted at the bottom

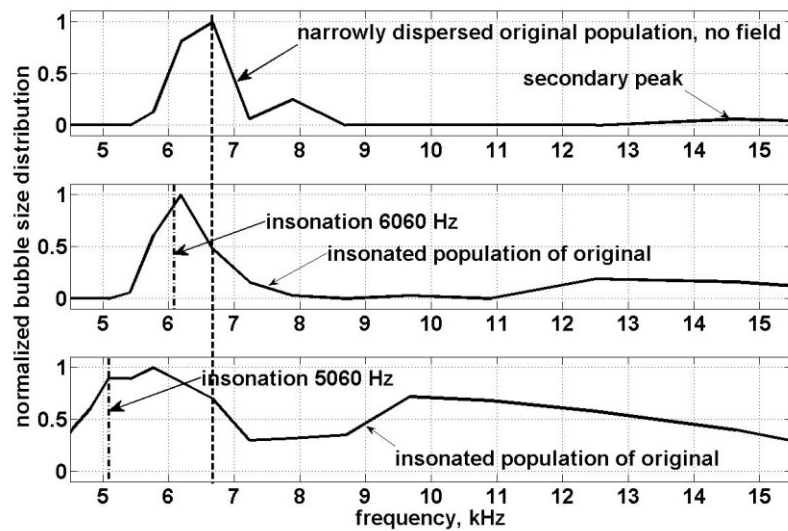


Figure 3.10. Distribution change in a generated pseudo-monodisperse air bubble column resulting from insonation at 5 and 6 kHz. The ordinate is the normalized bubble count in bins of bubble resonant frequency increments plotted on the abscissa in kHz. The mean frequency of the original bubble column and of the same column when insonated at 5 and 6 kHz is shown by dashed lines.

In Fig. 3.10 (top) the non-insonated population size is closely grouped around bubbles having resonance near 6.7 kHz. The model predicts that insonating them at a frequency of 6 kHz should have the effect of growing larger bubbles, thus shifting the new bubble mean frequency downwards, peaking around 6 kHz where bubble change would stop. This same effect is also expected for the higher frequency secondary peak of the uninsonified population. Then, when insonated at 5060 Hz the new mean should shift further downward approaching the insonation frequency. The center and bottom plots confirms this.

The shift of the original secondary peak by the lower insonation frequencies is not fully understood because although this shift is in the right direction the shift seems more pronounced by the 5 kHz radiation than by the 6 kHz which would be otherwise expected to cause the greatest change. At least two factors may account for this: First, the plot is done by normalizing bubble distributions. Its therefore possible that bubbles very near the resonant frequency are being eliminated so as to make the secondary peak more pronounced. Secondly, the radiating transducer contains higher frequency components wherein voltage and current to the transducer come closer in phase causing acoustic pressure peaks at these points. For instance it is noted that the shift in the original secondary peak at around 14.5 kHz is to nearly the first harmonic frequencies of the radiated signal (~12, ~10).

Fig. 3.10 addresses the case when a population is forced at a frequency promoting growth. Remaining unaddressed is the case of a mono-disperse bubble column being radiated at a forcing frequency higher than the mean frequency of the column where the

model predicts bubble shrinkage. This would be seen as a shift to higher bubble frequencies in the forced population.

To study insonation of mono-disperse bubble columns using higher frequencies than mean bubble resonance, a bubble pipe generator was installed at the bottom of a 40 L hexagonal water-filled aquarium as employed to produce Fig. 3.10. In this experiment a cylindrical, 44 kHz transducer irradiated the column from the top of the tank with the axis of the transducer aligned with the axis of the rising column so as to insonify the rising air bubbles in the far field. High speed, burst-mode photographs of the rising bubble column were made at the rate of 60 frames per second, and a shutter speed of 1/2000 seconds with a Panasonic DMCFZ100 camera. Insonation occurred when the signal from the signal generator was switched to the audio amplifier and to the external triggering circuit of a Winsco Model E-43 Stroboscope. This had the effect of adding a light band to pictures taken with insonification. Therefore pictures without the light band are unforced. The sixty per second frame rate is sufficient to capture the same bubble image in at least 10 consecutive frames. A typical montage of a 10 frame sequence of insonation at 8.5 kHz is shown in Fig. 3.11.

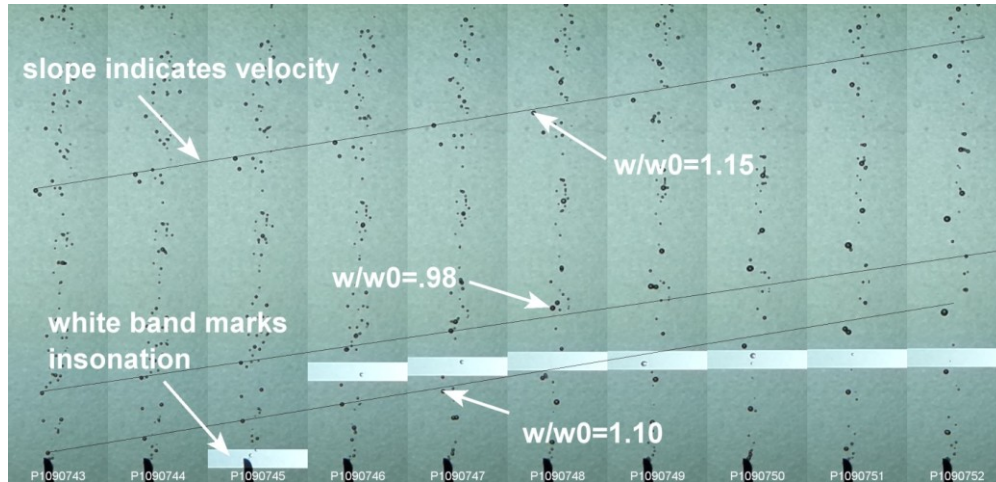


Figure 3.11 10 consecutive images of a rising air bubble column whose mean frequency is 9.7 kHz being insonated at approximately 1/20 bar by a 8.5 kHz continuous sine wave.

Small bubbles of a size unaffected by the forcing field rise at constant velocity without spiraling. The trace of these bubbles established by drawing a line connecting them will have a constant slope proportional to their velocity. Unaffected bubbles having no growth or shrinkage are quickly identified by this technique. Bubbles that change size as a result of acoustic signal exposure will show traces having a constant slope up to a frame showing insonation then the slope will become less steep if the bubble shrinks and slows down, or the slope will steepen if the bubble grows and accelerates. Furthermore, if the bubble is being continuously affected by acoustic exposure then it will accelerate away from the initially drawn unforced slope. Thus those accelerating upwards are continuously growing while those progressively slowing down are shrinking.

The effects described above are seen in Fig. 11. The top, and bottom traces show bubbles slowing down, thus shrinking having $\omega/\omega_0 = 1.15$ and 1.1 . The middle trace shows a bubble growing rapidly with $\omega/\omega_0 = .98$ which is closer to bubble resonance than the other cases. It can be further observed that the growth and shrinkage effect for these bubbles is happening in flight.

To quantify the average effect of insonating these rising bubble columns in a similar analysis as was employed to produce Fig 3.10 a script was written to automate ImageJ. The flow diagram of this script is shown below:

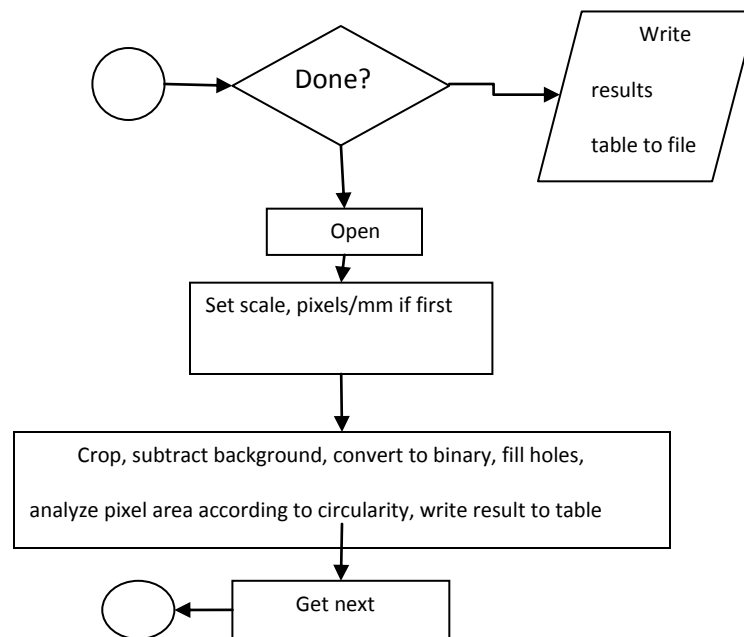


Figure 3.12. Flow diagram of ImageJ macro to process sets of unforced, and forced photographs.

Once the area in square millimeters for each bubble has been measured by ImageJ, and written to an ASCII txt file, the forced and unforced area files are read by a Matlab program that calculates individual bubble radii and resonant frequency storing this information in an array. The array is processed into a histogram, normalized then plotted. A plot for insonifying a mono-disperse bubble column by a forcing frequency that would be expected to grow bubbles in the unforced population is shown in Fig. 3.13 (A); while Fig 3.13 (B) is a plot of another similarly generated bubble column that is insonated at a forcing frequency which is expected to shrink bubbles in this population.

In Fig 13 (A), the unforced mean bubble frequency is 9.7 kHz. When this population of bubbles is insonated at a forcing frequency of 8.5 kHz which is below the population mean the model predicts a shift in the insonated population towards the insonating frequency meaning that bubbles will grow thus having lower frequencies. This was shown to happen in Fig 3.10 and is confirmed in Fig 3.13 (A).

In Fig 13 (b), the mono-dispersed bubble column produced by the bubble pipe mean size is larger with an unforced mean of 7 kHz. (It is very difficult to obtain exactly the same bubble sizes in different tests because size is a very sensitive function of bubble pipe parameters.) This population was insonated at 10 kHz which should make bubbles in the unforced stream smaller, thus shifting the population mean higher. Fig. 13 (B) shows this result with the forced population increasing from 7.0 to 7.4 kHz.

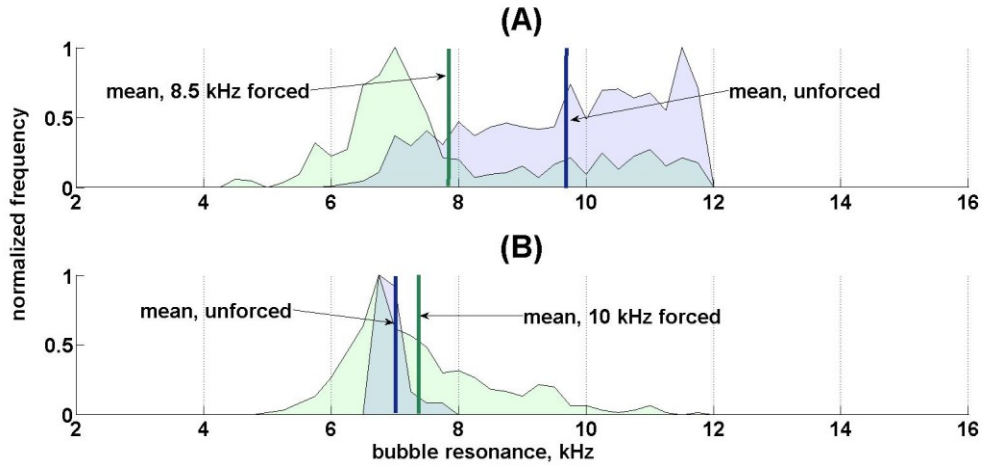


Figure 3.13. *Two mono-dispersed bubble columns exposed to forcing frequencies on both sides of the unforced population mean resonance. The ordinate is the normalized bubble count in bins of bubble resonant frequency increments plotted on the abscissa in kHz. The unforced population profile has been colored light blue, and its mean is marked by a heavy blue line. The forced population is colored light green, and its mean is shown by a heavy green line. These colors have transparency so the overlap in population frequency is a darker blue-green tint.*

The observation of the mean of bubble population size being shifted by insonation provided experimental evidence that distribution tuning by acoustic forcing appears possible. Figs 10 and 13 show how distributions plotted by resonant frequency shift when appropriate forcing frequencies are selected. The exact mechanism driving this shift can be explored in the model.

Model Predicted bubble behavior

Considering a bubble as a damped oscillator having a resonant frequency related to its size; the change in its size resulting from insonation will be mostly determined by the phase of the forcing thermal pulse to that of the oscillating bubble. When the thermal pulse is in-phase with bubble pulsations, the bubble will grow, when the thermal pulse is out-of-phase with the bubble oscillations, the bubble will shrink.

Model Predicted bubble behavior as a function of phase

The model predicted phase relationship is plotted in Fig. 3.14 for bubbles ranging in size from 0.2 to 0.8 mm when exposed to insonation frequencies starting at 6 kHz in 1 kHz steps up to 16 kHz. The shape of the trace of these computed points is dependent on the damping ratio. For this plot $\zeta = 0.1$ which is consistent with the combination of contributing damping factors, viscous, thermal and radiative, determined by Eller for oscillating bubbles [21].

Significant bubble size change, both growth and shrinkage, will occur near $\omega/\omega_r = 1$ where ω is the insonation frequency and ω_r is the resonant frequency of the bubble. When the bubble resonance frequency matches insonation frequency the phase angle is $\pi/2$ and the bubble will not change size.

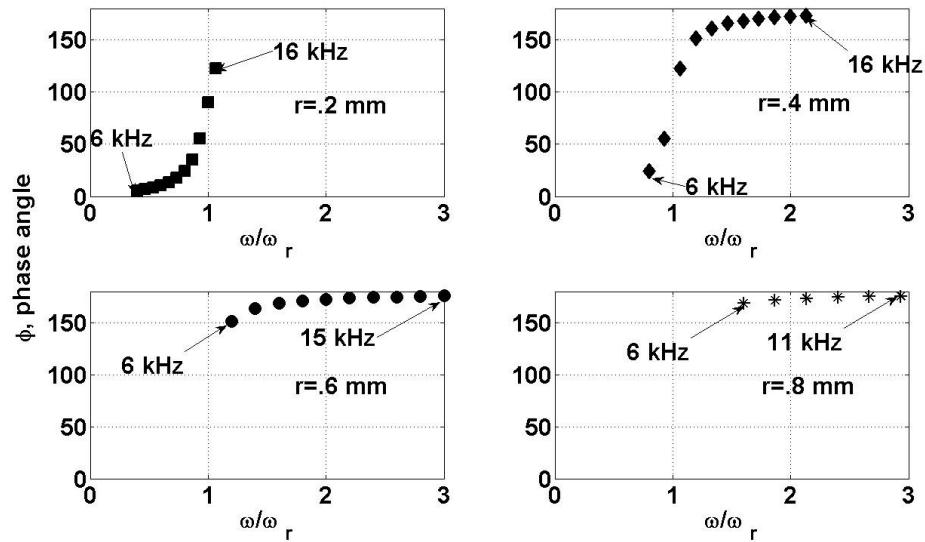
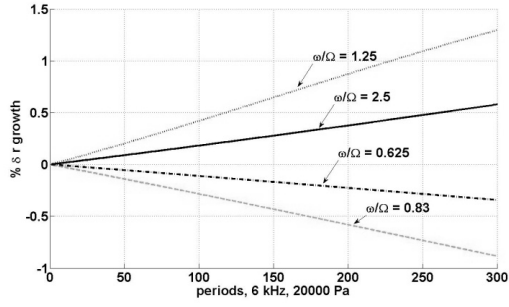


Figure 3.14. Phase angle in degrees between bubble displacement and the temperature pulse.

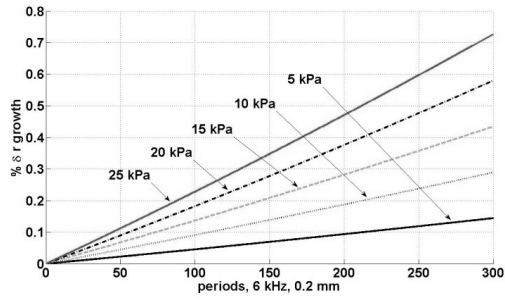
Examination of Fig. 3.14 reveals that bubbles of small size (i.e. 0.2 mm) are on the growth side of the phase curve for all 6-16 kHz frequencies, whereas the large bubbles (0.8 mm) are entirely on the shrinkage side. The mid-size bubbles (0.4 and 0.6 mm) span across resonance at 6-16 kHz insonation, and thus can grow or shrink depending on the insonation frequency in this range. Experimental data discussed previously for insonation at frequencies entirely below the resonant frequency of a bubble shows an increase in size, while data for insonation at frequencies above bubble resonance shows reduction in size, but data around resonance bubbles can grow or shrink depending on the phase angle.

Parametric studies

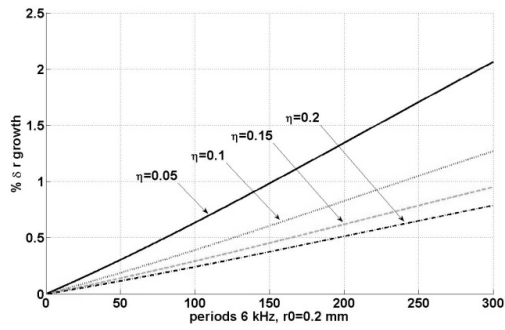
A parametric study was conducted to observe the sensitivity that initial bubble size, insonation amplitude, insonation frequency, damping and velocity have on bubble size change as plotted in Fig. 3.15. In each of these figures only one parameter was varied, the others being held constant. The parameter varied is identified to the right of the plot. In these plots, ω is the bubble natural frequency, while Ω is the insonation frequency.



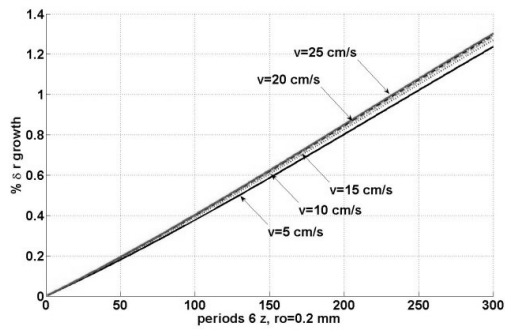
(a) bubble size varied.



(b) insonation amplitude varied



(c) damping varied



(d) velocity varied

Figure 3.15 a-e. Result of model parameter variations on bubble change

Fig. 15 (a) shows that bubbles having natural frequencies above the insonation frequency will grow. The closer the bubble resonant frequency is to the insonation frequency the more the bubble will grow. Conversely, larger bubbles, that have resonant frequencies below the insonation frequency will shrink. The closer the bubble resonant frequency is to the insonation frequency the greater the reduction in size. Unlike the growth effect on vapor bubbles when driven by latent heat, size change takes 100's of cycles instead of the 10's of cycles for vapor bubbles. However, growth or shrinkage will not persist for very long periods because the process is self limiting as bubble size reaches a size having a frequency approaching the insonation frequency. Even though the rectified heat transfer growth phenomena is reduced when latent heat is not a factor, it can still contribute significant size change near resonance.

Fig. 15 (b) demonstrates that stronger acoustic fields simply amplify growth or shrinkage.

Fig. 15 (c) shows the effect of damping on the response of a 0.2 mm bubble. At a fixed frequency chosen to promote modest growth in a given population as a reference, small damping that exacerbates resonance amplitude promotes the rectified effect while increasing damping reduces this effect. Damping is the result of three energy dissipation mechanisms [26]:

1. Radiation in the form of acoustic waves from the pulsating bubble which can be significant near resonance, and is responsible for the Bjerknes forces between bubbles which dissipates bubble energy.

2. Thermal losses to the fluid.
3. Work done against viscous forces. The consequences of this damping factor being slower size change in highly viscous fluids.

Fig. 15 (d) explores the effect of bubble velocity on growth. For vapor bubbles growth is a strong function of velocity, but for air bubbles the magnitude of heat transfer when sensible heat dominates appears to make a difference only for lower velocities.

Temperature penetration, diffusivity

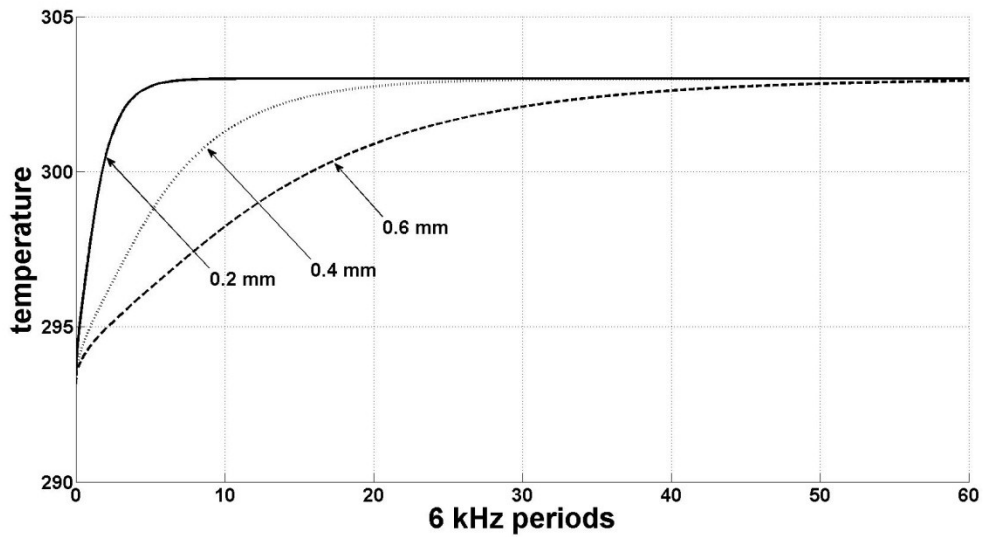


Figure 3.16. Temperature penetration to bubble center after 60 periods of 6 kHz insonation for a fixed temperature change of 10 K imposed on the outside shell at $t = 0$ seconds.

The influence of thermal diffusivity on size change in the first 60 periods of 6 kHz insonation for 0.2 to 0.6 mm radius bubbles was explored with the model. The predicted result is plotted in Fig. 3.16 which shows that larger bubbles with respect to a given acoustic insonation frequency experience a much longer thermal penetration time than smaller ones. When bubbles of different size are modeled with a step temperature change at their surface it is found that the larger bubbles reach thermal equilibrium in a time greater than 60 periods of the driving frequency. This is in contrast to the findings of Hao and Prosperetti [3] where vapor bubbles expand in the first cycle.

Conclusions

At a given frequency of insonation, air bubbles with about the same velocity in room temperature water can remain almost unchanged by the acoustic field, or can grow, or shrink in size at a rate that increases significantly when the resonant frequency of the bubble is near the acoustic field frequency. This is strongly a function of how close the natural frequency of the bubble is to the insonation frequency, and on the intensity of the acoustic environment it passes through.

The mechanism for this behavior in vapor bubbles has been extensively explored by others. In general, bubbles will change size by change in hydrostatic pressure over a significant distance, they will change size and shape if rising and their radius is above a certain size, they will change by convective transfer of heat and mass, and they will change by a rectification effect of pulsing surface area and boundary layer on both heat and mass transfer. The latter being especially true for vapor bubbles. In this work

insonified air bubbles rising short distances in plain shallow water at room temperature, the operative mechanism near resonance appears to be rectified heat and mass transfer. In this work, these mechanisms have been modeled by a much simplified, adaptive numerical analysis model based on a thermodynamic approach.

When modeled as a mass on a spring with damping, the model shows the combined damping constant also has a strong effect on bubble growth and shrinkage as expected in a damped oscillator model when near resonance. However, bubble change around resonance would be much greater than observed except for the fact that the thermal pulse generated by the compression effects is in phase transition. It shifts from in-phase with bubble oscillations, thereby reinforcing growth, to out-of-phase, which supports bubble shrinkage.

It was found that the change in growth for air bubbles in 20°C water is a much weaker function of velocity than is the case for vapor bubbles near boiling as discovered by Hao and Prosperetti.

Air bubble size change in 20°C water due to ultrasonic insonation appears to happen even though the mechanism promoting this change is much weaker than occurs with vapor bubbles near boiling. The mechanism for the latter is the cycling of evaporation and condensation involving latent heat transfers two orders of magnitude greater than the sensible heat transfers for air not undergoing a phase change.

This work turns attention to the behavior of injected air bubbles such as is used for protein skimming in aquariums, aeration of wastewater, and the attempt by injecting air bubbles to change the characteristics of bitumen to facilitate efficient burning as fuel. Since size change is strongly related to insonation near the resonant frequency, and to acoustic pressure levels, it is likely that applications which take advantage of this phenomena would do so by pulsing the ultrasonic field to obtain a broader frequency range and to increase field strength, by sweeping the frequency source, or by using multiple sources of different frequencies.

Nomenclature

A nodal interface area, m^2

A_{ns} nodal interface areas, m^2 for node n

A_s Surface area, m^2

C concentration

C_S concentration at bubble surface M/m^3

c_p specific heat of air, kJ/kgK

C_∞ concentration in fluid M/m^3

D mass flux diffusion constant

D bubble diameter, m

E energy of element, J

F applied force, N

F_T transmitted force, N

h heat transfer coefficient, W/m^2K

i superscript, current time

$i+1$ superscript, next time step

i_0 static enthalpy crossing control volume boundary 0-0, J/Kg

i_T static enthalpy crossing control volume boundary T-T, J/Kg

h_{mass} convective mass transfer coefficient

k conductivity, Wm/K

\dot{m} rate of mass loss, kg/s

n node counter

Nu Nusselt number

P pressure, Pa

P_a acoustic pressure, Pa

P_{atm} atmospheric pressure at sea level, Pa

Pr Prandtl number

\dot{Q} rate of heat transfer, W

r radius of bubble, m

dr increment of nodal distance, m

Re Reynolds number

T time, s

T, t temperature, K

T_s nodal surface temperature, K

T_∞ temperature of far environment, K

u temperature in heat equation, K

V volume, m^3

vel velocity, m/s

∇ Laplacian operator

α thermal diffusivity, m^2/s

γ ratio of specific heats

Δ increment

ζ damping coefficient

μ dynamic viscosity, Ns/m^2

ν kinematic viscosity, m^2/s

ρ density of air, kg/m^3

σ surface tension, N/m

τ dimensionless time

φ phase angle, radians

ω angular frequency, radians/s

ω_r resonance angular frequency, radians/s

Ω resonant angular frequency associated with bubble size, radians/s

Γ thermal diffusion coefficient, $\text{kg}/(\text{m s})$

References

1. Wang, T., Rectified heat transfer, *J. Acoust. Soc. Am.*, **56** (4), p. 1131-1143 (1974)
2. Patel G.M., Nicholas R.E., Finch R.D., Rectified heat transfer in vapor bubbles, *J. Acoust. Soc. Am.*, **78** (6), p. 2122-2131 (1985)
3. Hao, Y, Prosperetti, A., Rectified heat transfer into translating and pulsating vapor bubbles, *J. Acoust. Soc. Am.*, **112**, (5), p. 1787-1796, Pt. 1, (2002)
4. Ashokkumar, M, Lee, J, Kentish, S, Grieser, F, Bubbles in an acoustic field: An overview, *Ultrasonics Sonochemistry* **14**, p. 470–475, (2007)
5. Leong T, et al., Growth of Bubbles by Rectified Diffusion in Aqueous Surfactant Solutions, *J. Phys. Chem. C*, **114**, p. 20141–20145, (2010)
6. Rubio J, et al., Overview of flotation as a wastewater treatment technique, *Miner Eng* **15**, p. 139–155, (2002)
7. Thakur, R.K., et al., Combined effects of process parameters and composition on foaming of dairy emulsions at low temperature in an agitated column, *J Food Eng*, V 68 I3, p.335-347, (2005)
8. Zuñiga R N, Aguilera J M, Aerated food gels: fabrication and potential applications, *Trends Food Sci Tech*, **19**, p. 176-187, (2008)

9. Mohan A.M. et al., “Effervescent Spray Characterization of Jatropha Pure Plant Oil”
23rd Annual Conference on Liquid Atomization and Spray Systems, Brno, Czech Republic, p. 1-3, September (2010)
10. Hosny, A.Y., Separating oil from oil-water emulsions by electroflotation technique,
Separations Technology V6 p. 9-17,(1996)
11. Rasband, W., ImageJ 1.45j, *National Institutes of Health*, USA
12. Hsieh D Y, Plesset M S, Theory of Rectified Diffusion of Mass into Gas Bubbles, *J. Acoust. Soc. Am*, V33, No 2, p. 206-215,(1961)
13. Levich V.G.: Physicochemical Hydrodynamics. N.J., EnglewoodsCliffs. Prentice-Hall (1962)
14. Cengel, Y. Heat and Mass Transfer, 3rd edition, McGraw-Hill, ISBN:10:0-07-312930-5, p. 285-334, (2007)
15. Epstein P.S., Plesset M.S., On the Stability of Gas Bubbles in Liquid-Gas Solutions, *J Chem Phys*, **18**, 11 p. 1505-1509, (1950)
16. Cerza M, et al., Pseudo-Steady Diffusional Growth or Collapse of Bubbles Rising in Time Dependent Pressure Fields, *Laboratory for Computational Physics and Fluid Dynamics*, NRL Memorandum Report 6584, p. 12-24, (1990)
17. Kays, W.M., Crawford, M.E., Convective Heat and Mass Transfer, 3rd Ed., (1993), McGraw-Hill, Inc., ISBN 0-07-033721-7

18. Attard, P., Miklavcic S., Effective Spring Constant of Bubbles and Droplets, *Langmuir*, 17, p. 8217-8223, (2001)
19. Thomson, W.T., Theory of Vibration with Applications, Prentice Hall, ISBN 0-13-914549, p. 63, (1972)
20. Lohse D, Bubble Puzzles, *Physics Today*, 36, p.37 (2003)
21. Eller, A.I., Damping constants of pulsating bubbles, *J. Acoust. Soc. Am.*, 47, p.1469-1470, (1970)
22. Hagen, K., Heat Transfer with Applications, Prentice Hall, ISBN 0-13-520941-2, p. 174, (1999)
23. Libermann, L, Air Bubbles in Water, *J Appl Phys*, 28, 2, p. 205-212, (1957)
24. Crum, L.A., The polytropic exponent of a gas contained within air bubbles pulsating within a liquid, *J. Acoust. Soc. Am*, V73, p 116-120 (1983)
25. Higgins, P. W., Lengsfeld, C, A shielded acoustic probe for accurate dynamic pressure measurements in the near field of a radiating ultrasonic transducer, accepted by *J Eng Appl Sci*
26. Leighton, T.G., The Acoustic Bubble, *Academic Press*, p.175, (1974)
27. Cox, D.J. et al, Ultrasound-Induced Dissolution of Lipid-Coated and Uncoated Gas Bubbles, *Langmuir*, 2010, 26(18), 14774–14781

28. Gehrke, T. Overhoff, H.M., Microbubble Oscillation due to harmonic, pulsed and frequency modulated excitation with ultrasound, Medical Engineering Laboratory, University of Applied Sciences Gelsenkirchen

Chapter Four: Improving micro cooler performance by insonation

Introduction

The operation of high-performance electronic systems (e.g. computers, RF electronics and solid state lasers) are currently limited by thermal management issues. There is a need to maintain these devices within their acceptable operating range while removing heat in excess of $1\text{kW}/\text{cm}^2$ flux and $1\text{kW}/\text{cm}^3$ heat density as well as hot spot mitigation above $5\text{ kW}/\text{cm}^2$ [DARPA-BAA-12-50]. All this must be accomplished with a minimum amount of size, weight and power consumption added to the overall system. Many speculate that these high heat fluxes can only be dissipated if both the sensible and latent heat can be accessed through two phase, micro fluidic cooling system. More over the addition of bubbles to a otherwise laminar flow will add desirable turbulent mixing to enhance the local heat transfer coefficient.

Micro channel coolers operate by allowing high conductivity materials (e.g. copper, diamond etc.) to transfer the heat from the chip over a volume in as uniform temperature profile as possible. The more uniform the temperature profile within the solid volume of the cooler, a maximum utilization of the entire convective heat transfer

surface can be obtained. The solid material of the cooler is embedded with micro channels to transfer the heat from the material into a flowing liquid and away from the chip. Tukerman [1] conducted an numerical optimization of these channels and found that milli or micro channels widths with heights equal to 10 times the height maximized heat removal in single phase flows. In a single phase region heat removal involves sensible heat only which for water is $4.18 \text{ J/}^\circ\text{C}$. For example, for every gram of water within the micro channel, 4.18 J will be removed for each degree of coolant heating. Unlike single phase operation were higher flow rates yield high heat transfer coefficients access to phase change or latent heat enhances heat transfer in two phase flow. Thus as coolant flow rate decreases, more energy will have been transferred to a single unit mass of coolant allowing a fraction of the liquid to be converted to gas (termed quality), see Figure 4.3. In this case the water temperature remains the same, but the heat absorbed vaporizes the water. The energy required to vaporize water is 2676 J/g . Thus observing the same 1 gram of water as before but assuming 10% of the water is vaporized one would achieve 267 J of heat removal. Therefore the potential enhancement of operating micro channel coolers even in a low quality region is 64 times better. State-of-the-Art micro channel coolers have obtained heat flux capabilities above 100 W/cm^2 , thus two phase operation will mitigate the 5kW/cm^2 hot spot requirements projected in the future.

Four critical engineering problems must be overcome to make two phase operation reliable. First, the nucleation of bubbles in specific regions is desirable to ensure transition to two phase flow, however, the surface roughness of these channels is less than 2% of the channel width (i.e. 100 to 500 nm) often causing the system to be

superheated as no nucleation sites exist [2]. Second, microfluidic flows are dominated by surface tension forces making bubble removal from the wall difficult [3]. When bubbles are not removed effectively a gaseous insulating layer will form that degrades the performance for heat dissipation. Third, bubbles that are removed or translated downstream are in close proximity and with thereby rapidly coalesce raising the pressure requirements to drive the flow, see figure 4.1, and eventually causing dry out or channel blockage. Finally, the total lifetime of these systems is limited by corrosion and erosion problems.

Bubble nucleation or the onset of stable cavitation by acoustic fields is well established [4]. The onset of bubble formation is a function of the operating frequency, intensity of the pressure field, vapor pressure of the solution and predominance of available nucleation sites. Other experiments in our lab have demonstrated the ability to translate this to confined micro channels (Appendix B]. As acoustic fields are applied to liquid media a phenomena of acoustic streaming can be observed especially under high intensity oscillations. Energy from the acoustic emission is absorbed by the fluid and translated into forward fluid motion. Several researchers have reported attempts to remove bubbles from micro channel surface via acoustic streaming but will promising the efficiency of this process is very low, much less than 1% [5]. Previously our lab established that air bubbles rising in water exposed to low intensity acoustic fields can shift the mean bubble size by rectified mass transfer. This work seeks to determine if energy efficient, low intensity acoustic fields will improve micro channel cooling

performance through bubble management; maintaining bubbly flow at larger quality factors. See fig. 4.2.

The flow transitions shown in Fig. 4.1 and 4.2 are well known, and have been studied by several researchers [6][7][8][9][10].

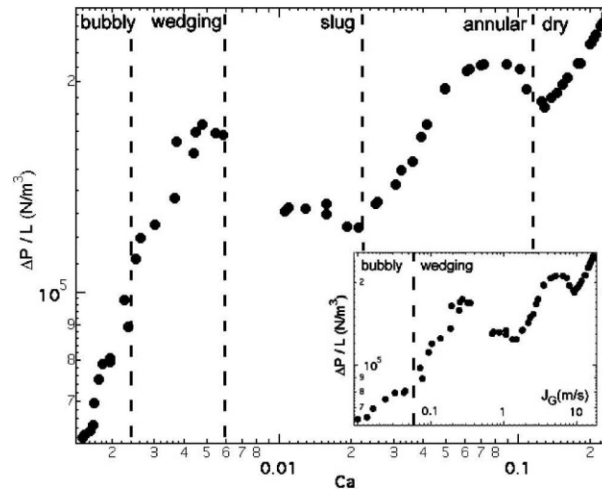


Figure 4.1 (Figure 15 from Cubaud [6]) Pressure drop as a function of capillary number showing flow regimes. Channel height is 200 microns.

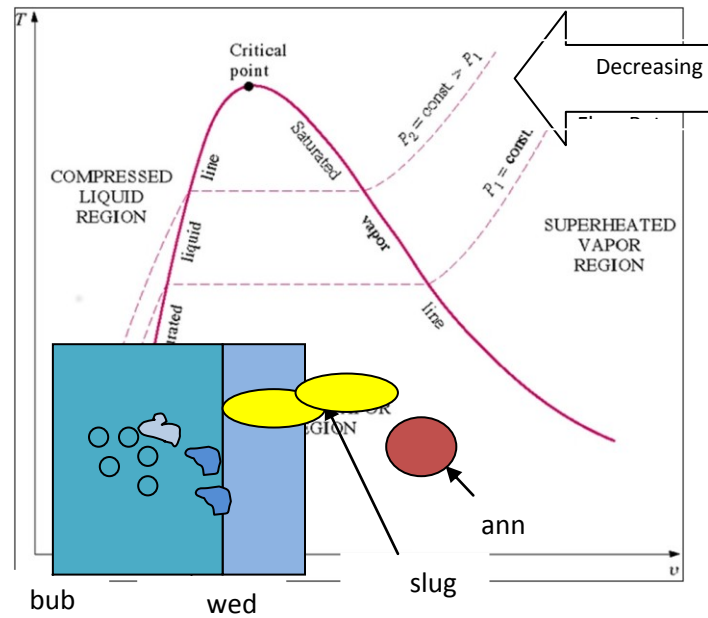


Figure 4.2. Shaded box containing bubbles is effective operating range for insonated heat exchanger performance improvement.

Recent approximations of heat flux in low quality boiling

Confirmation of the advantages of operation of a cooler at the onset of boiling has been published by Bertsch [11], and is plotted in Fig 4.2. In this figure it is seen that the heat transfer coefficient peaks at near $8500 \text{ W/m}^2\text{K}$ when the quality is 0.2 and the mass flux is $81 \text{ kg/m}^2\text{s}$. The data points are for R-134a $D_h=1.09 \text{ mm}$. A complete summary of experiments done on near boiling heat transfer coefficients may be found in this paper.

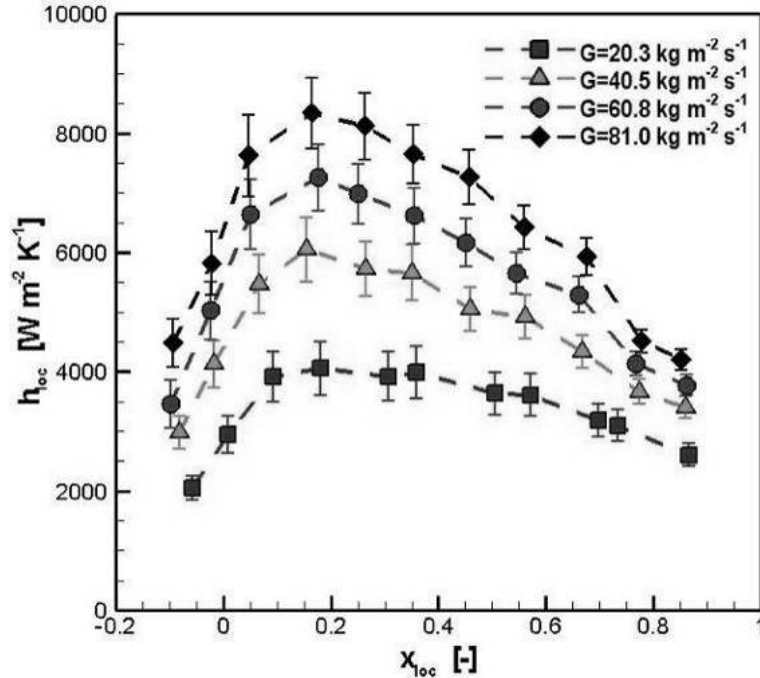


Figure 4.3 Variation of heat transfer coefficient for low values of quality and mass flux, G

Fluent modeling of bubble development near the exit of a cooler

The development of bubbly flow in a milli channel was simulated using VOF (volume of fluid) numerical modeling in Fluent, a computational fluid dynamics program. A milli channel of height 200 microns with 2 mm width and a centimeter long having walls heated to 400 C was studied with water coolant at different flow rates. Specialized UDF (user defined function) code was written to capture vapor bubbles from cell data having vapor fractions ≥ 0.75 . Fig 4.4 is a solution capture when the flow was 9.6 mL/min showing bubbles accumulating near the exit of the channel.

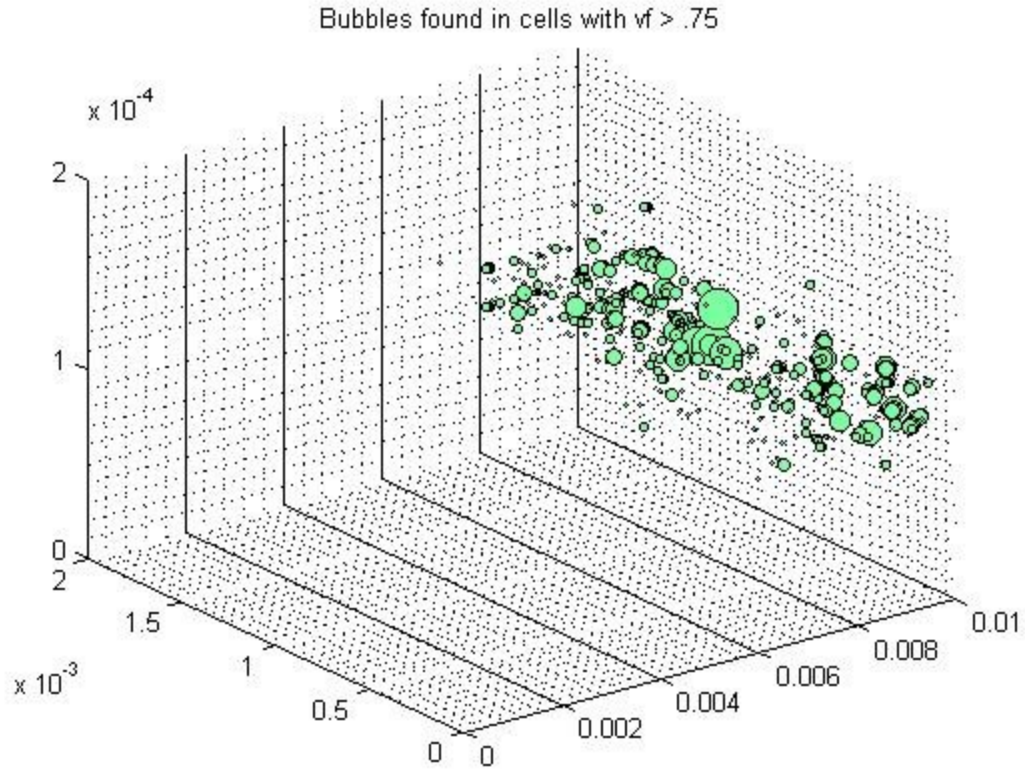


Figure 4.4 Fluent modeling of developing bubbly flow in milli channel cooler

Heat transfer coefficient and hydraulic diameter

Enhanced forced convection used to cool micro channel devices must be maximized by circulating coolant absorbing heat along the surface area of the channel according to Newton's Law of Cooling:

$$\frac{\dot{q}}{A} (\text{heat flux}) = h \cdot (T_w - T_c) \quad (1)$$

Wherein \dot{q} is thermal energy transferred (W), A is surface area of channel (cm²), h is the heat transfer coefficient, T's are local temperature of walls and coolant (°C). Heat is

normally absorbed by the copper construction of the cooler and spread out over it.

Maximizing thermal conductivity of the cooler is important to create uniform temperature over the entire structure for efficient heat removal and avoidance of hot spots.

The heat transfer coefficient for flow in a rectangular channel is:

$$h = Nu \cdot k / D_H \quad (2)$$

where Nu is Nusselt number, k is thermal conductivity of the coolant and D_H

is the hydraulic diameter of the channel given by:

$$D_H = 4 \cdot A_c / P \quad (3)$$

In which A_c is the cross sectional area of the channel and P is its perimeter. For laminar flow as determined from Reynolds number, Nu has constant values of 3.657 (constant wall temperature) or 4.364 (constant wall heat flux) before the onset of boiling. In case of constant wall temperature the thermal temperature profile through the channel is linear, for constant wall heat flux the coolant profile is logarithmic. Tuckerman and Pease (1981) were the first to notice that large heat transfer coefficients can be achieved with small hydraulic diameters. This in itself does not fully explain why micro channels are so efficient. The reason a high heat transfer coefficient for very small device dimensions does not cancel benefit is that as channels decrease to 100's of microns the ratio of surface area to the volume of the contained coolant increases, Fig 4.5. Thus,

micro channels have a comparatively large surface area to gather heat that is carried away by the thermal absorption capacity of the coolant.

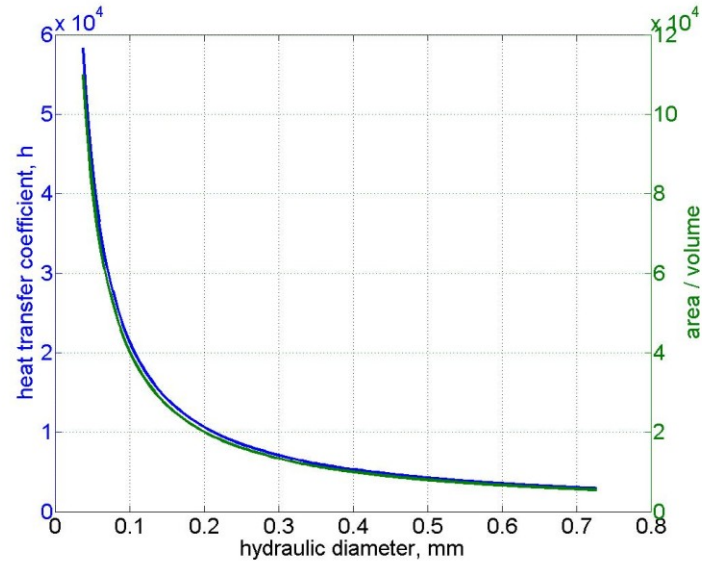


Figure 4.5 Heat transfer coefficient, h , and surface area to coolant volume as a function of micro channel scale.

Objective and Methods

The objective of this work was to test the hypothesis that insonating micro channel heat exchangers of different dimensions can improve heat flux dissipation. Performance was evaluated as a function of flow rates, insonation frequencies and quality factor to understand if the enhancement is uniform or dependent on operating conditions. Visual observations of bubble management were performed near dry out in an optically accessible milli channel. Subsequently, a parametric study to quantify the enhance heat dissipation by isonisation evaluated over a range of quality factors in both a milli

(channel width = 100's μm) and micro (channel width = 10's μm) channel cooler. Conditions in single phase operation were conducted to evaluate the effect of stable, localized cavitation. Studies at different forcing frequencies explored the impact of acoustic streaming versus rectified mass transfer bubble size management. Lastly, an investigation of duty cycling the acoustic field to maintain bubbly flow yet reduce power consumption was conducted using a pulsing mode transducer driver integrated into a micro channel cooler.

A detailed description of the test, the apparatus used and its setup, and test procedures employed for each of these experiments follows.

Optically Accessible Mill Channel Cooler

A glass-covered channel 300 μm deep by 1 cm wide was milled in a 1 cm thick, 10 cm by 10 cm aluminum plate with embedded heaters. Water was pumped by a Watson Marlow peristaltic pump through the channel at a flow rate between 2 and 10 mL/min. Bubbles formed as the mean coolant temperature approached boiling (e.g. coolant in close contact to heated surface could be boiling while the mean fluid temperature is below boiling). When channel flow was observed restricted by dry out or partial blockage a 28kHz, 150 volt acoustic field was applied. The transducer was in contact with the unheated side of the aluminum plate and in close proximity to the cooling channel was driven by sine wave, and the effect on channel flow was recorded using a digital microscope video recorder. The layout for this experiment is shown in Fig. 4.6 below.

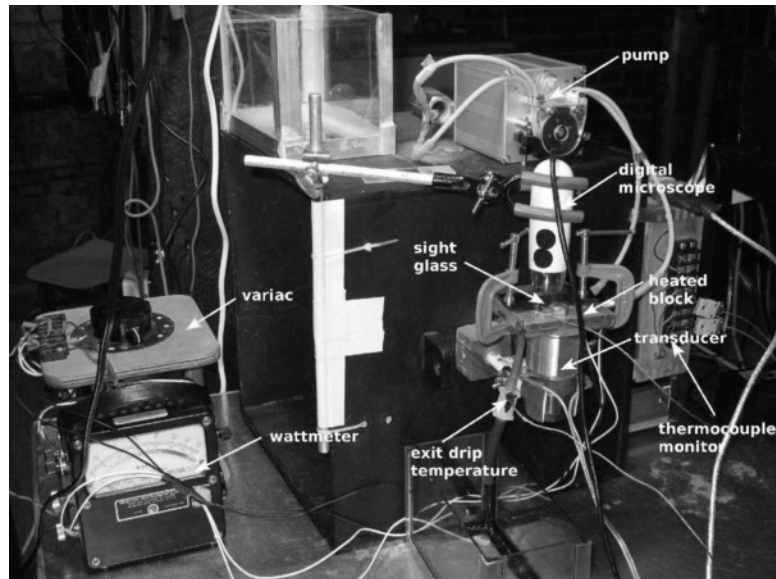


Figure 4.6 Setup for video taped channel study.

Insonation System

Three micro channel coolers were constructed: a milli channel, micro channel and one only used in the pulsing experiment. The channel attributes are summarized in Table 4.7.

	H, mm	W, mm	L, mm	D_h, mm
Milli Channel	330	10	24	64
Micro Channel	20	0.2	50	40
Pulsed Trans.	25	0.250	50	45

Table 4.7 Cooler attributes

For all testing insonation was done using bolt-clamped Langevin transducers from Steiner & Martins having resonances of 28 kHz and 120 kHz and constructed from SM 118 ceramic material having a Curie temperature of 300 C. The signal to the transducer was generated by a Leader LAG-120B then amplified by a Crest Vs 1100 audio amplified operated in the bridged mode. Impedance matching to the 35 Ohm (resonant) resistance of the transducer is done with a 4:1 coils power transformer. Further impedance tuning is accomplished with a 3 mH inductor in series with the load.

Temperature measurements were accomplished using K-type thermocouples with welded junctions. K-type thermocouples were chosen for accuracy and small size. Thermocouples were connected to an Omega Engineering OMR 6018 data acquisition module communicating with a LabView interface that decodes the multiplexed channels, display's the real-time values and logs the data to an ASCII text file. Calibration of the DAQ is accomplished using a Transmation 1045 SN calibrator to accurately produce the 0-55 mV range signals needed by the DAQ. The DAQ automatically generates the cold junction compensation. The logged data was read and processed by MatLab.

A Watson-Marlow peristaltic 2 channel pump, model Alita 400, was employed to displace non-circulating, plain water through the test heat exchangers at rates ranging from 2-4 mL/min.

Thermal resistance of insonated heat exchangers

Heat exchangers with hydraulic diameters of 64 μm (fixture 1) and 2 μm (fixture 2) were insonated at different flow rates and frequencies. Input power was always maximized to assure insonation of the flow through the connection to the radiating transducers.

The thermal resistance was computed from:

$$R_T \left(K \frac{\text{cm}^2}{\text{W}} \right) = \frac{\Delta T_{bc} \text{ (K)}}{\dot{q} \left(\frac{\text{W}}{\text{cm}^2} \right)} \quad (4)$$

ΔT_{bc} is the temperature difference across the interface between the heated billet and the micro channel cooler. \dot{q} is the heat flux input to the exchanger computed from:

$$\dot{q} = hA\Delta T_e \quad (5)$$

Where h is the laminar flow, constant wall heat transfer coefficient equal to 3.657, A is the channel area and ΔT_e is the temperature gain of the coolant passing through the exchanger.

The heat flux dissipated by radiation and conduction is assumed to be nearly constant over an individual data set but may vary among data sets accounting for the unforced thermal resistances at the same flow rate being different.

Milli Channel Cooler

Surface tension is well known to dominate the behavior of fluids within micro fluidic devices. A parametric study was first conducted in a milli channel cooler that had higher surface tension affects than the bulk flow bubbles explored in chapter 3, but less influence than micro channel coolers. This milli channel cooler also had dimensions that were consistent with the frequencies investigated in chapter 3. The cooler was constructed from a 3 mm brass plate with 2 mm coolant entrance and exit ports. A top brass plate 0.4 mm thick was press-bonded using cyanoacrylate to minimize joining thickness. The dimensional resonant frequencies for height and width were 24 kHz and 6 kHz, respectively. Heat absorption was monitored by measuring the mean fluid temperature when in contact with a heater held at constant heat flux (ie., maintaining constant input electrical power from a variac and monitored by a wattmeter). Thermal contact between heater and the exchanger was maximized by the use of Active Silver Ceramique heat sink compound.

The coolant was preheated water. Preheating insured two phase operation within the cooler without driving heat block temperatures above the Currie temperature of the transducer. beaker. K-type thermocouples were bead welded then placed to monitor heater body temperature, heat exchanger case temperature and coolant exit temperature. The PZT transducer was driven by continuous sine wave signals in the range 5-100 kHz and 100-300 volts This was accomplished by connecting the 2 V_{pp} output signal from a Leader LAG 120B signal generator to a bridge-mode Crest Vs 1100 audio amplifier. The 8 Ω output impedance of the amplifier was transformed to the near 35 Ω input impedance

(at resonance) through a 1:4 windings power transformer which also increased the output voltage. To compensate for the transducer capacitance a 2.5 mH inductor was placed in series with it. The apparatus setup with component labels is shown in Fig. 4.8.

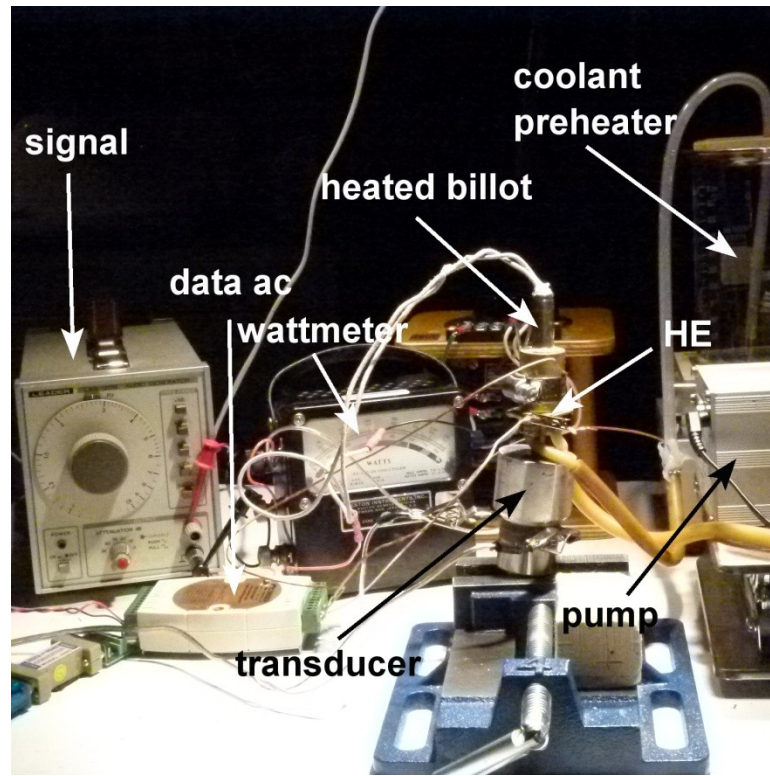


Figure 4.8 Apparatus setup for milli channel cooler

Micro Channel Cooler

As passage size reduces and bubbles shrink, the capability of surface tension to dampen out affects increases, thus a similar yet smaller parametric study as described above was conducted on a channel cooler with dimensions 1/10th those previously investigated. The cooler was constructed from a 3.3 mm etched brass plate with 2 mm

coolant entrance and exit ports. The dimensional resonant frequencies for height and width were 326 kHz and 32.6 kHz, respectively. Heat absorption was monitored by measuring the mean fluid temperature when in contact with a heater held at constant heat flux (ie., maintaining constant input electrical power from a variac and monitored by a wattmeter). Thermal contact between heater and the exchanger was maximized by the use of Active Silver Ceramique heat sink compound. A 120 kHz Langevin transducer was driven by a 200 volt sine wave at 39 and 80 kHz.

Pulsed Transducer Integrated Micro Channel Cooler

Continuous wave excitation from amplification of signals from a sine wave generator by an audio amplifier has the disadvantages that the equipment to accomplish this is relatively expensive, large in size and audio amplifiers are not intended for use above 20 kHz even though it has been found that such amplification can be achieved for limited durations up to 100 kHz.

In industrial practice it might be advantageous to excite the heat exchanger with high-voltage, very short duration pulses if similar results to continuous wave excitation could be achieved.

This experiment is designed for pulsing from 1 to 5 pulses per second. To accomplish this an elementary transducer pulse generator has been constructed and its electrical schematic appears in Fig. 4.9.

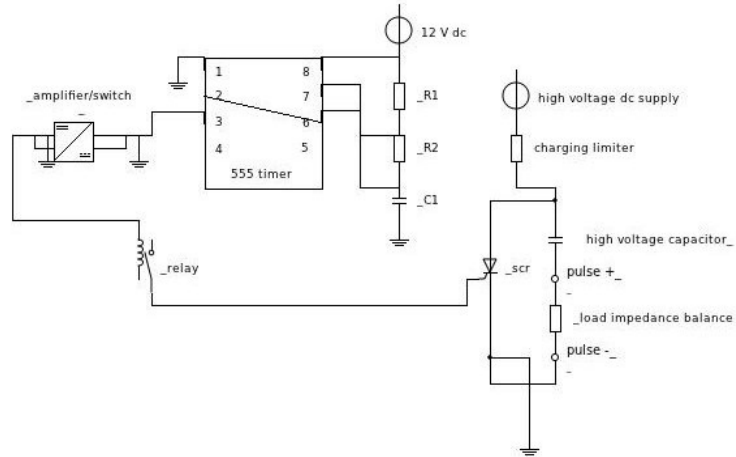


Figure 4.9. Electrical schematic for pulse generator

In this device, a 555 integrated circuit timer generates a 12 V_{pp} high impedance square wave pulse train having on and off times and duty cycle determined by the resistance values, R1 and R2 and the capacitor, C1. These contribute according to:

$$f = \frac{1}{0.693 \cdot (R1 + 2 \cdot R2) \cdot C1} \quad (6)$$

$$t_{on} = 0.693 \cdot (R1 + 2 \cdot R2) \cdot C1 \quad (7)$$

$$t_{off} = 0.693 \cdot R2 \cdot C1 \quad (8)$$

where f is the frequency and R1, R2 and C1 are components shown in Fig.4.10. The timer pulse train opens and closes contacts in a pc board mounted relay. If the output pulse train fails to operate the relay contacts, it may need to be amplified by a 741 operational amplifier, or use an intermediate 2N-2441 high speed switching transistor. In our testing impedance boosting of the timer wave train was unnecessary. The opening

and closing of the relay contacts shorts the gate of a high voltage SCR to its cathode which immediately turns on the SCR, discharging a high-voltage pulse capacitor through an impedance matching (to the transducer) resistor. When the positive pulse from the timer passes, the relay contacts close, the gate is no longer shorted to the cathode, and the SCR turns off. When the SCR is in the off state, high dc voltage from the supply appears simultaneously on the anode of the SCR and on one side of the high voltage capacitor which is storing the energy for making output pulses.

Input high voltage of the order of 400-1000 Vdc can be obtained by a commercial device, or it can be produced by transforming 120 Vac mains to the desired high voltage ac, then rectified and filtered.

Short pulses have high frequency components as seen in a Fourier transform of the pulse shape. In order for pulses to effectively drive a 28 kHz ultrasonic transducer they must have a high voltage magnitude and be very short duration. As the duration shortens, higher frequency components are produced. It is for this reason that an SCR is used to switch the charge storage on the capacitor instead of a transistor switch which cannot activate fast enough for the needed high frequency components. This can be seen in the Fourier transform of a much longer test pulse plotted in Fig 4.10.

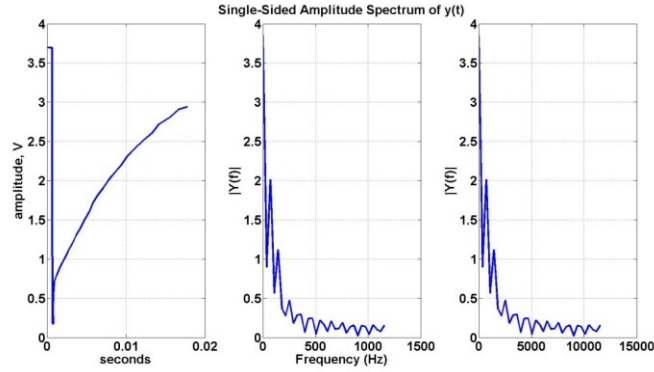


Figure 4.10 Fourier analysis of pulse shape; (left) long duration test pulse as determined by the value of pulse capacitor, (center) dft of pulse (right) dft of same pulse but occurring 10 times faster.

It is seen in Fig. 4.10 that a pulse lasting 20 ms distributes most of its energy below 250 Hz. If this same pulse shape happened in a tenth of the time (ie 2 ms) then this energy distribution extends to 2500. Thus, in order to get sufficient energy into a 28 kHz transducer the pulse must happen on the order of 20 micro seconds. This requires a low value, high voltage pulse capacitor, a high supply dc voltage and very fast switching time.

The pulsing experiment was performed with the apparatus shown in Fig. 4.11. Test fixture 3 was heated by contact, then separated from the heater. Its cooling with circulating alcohol at 6 mL/min was recorded with and without pulsed insonation.

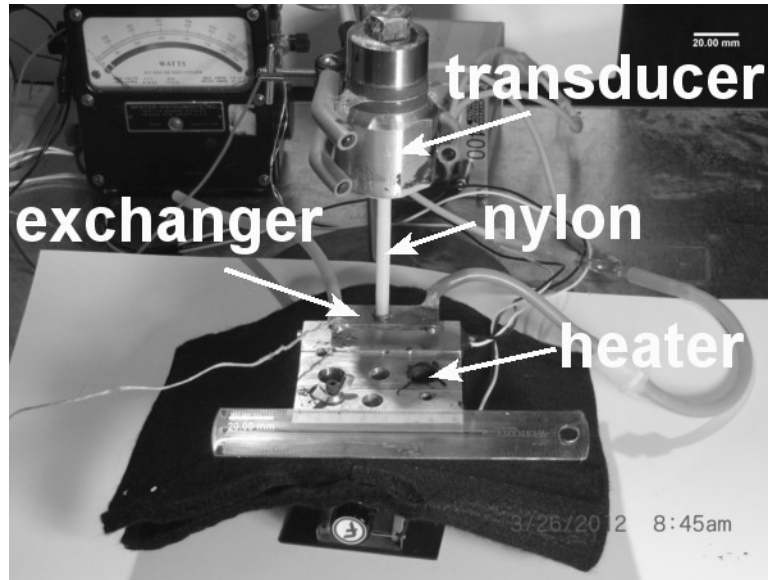


Figure 4.11 Setup for pulsed experiments. A closed alcohol coolant circuit was used.

Results and Discussion

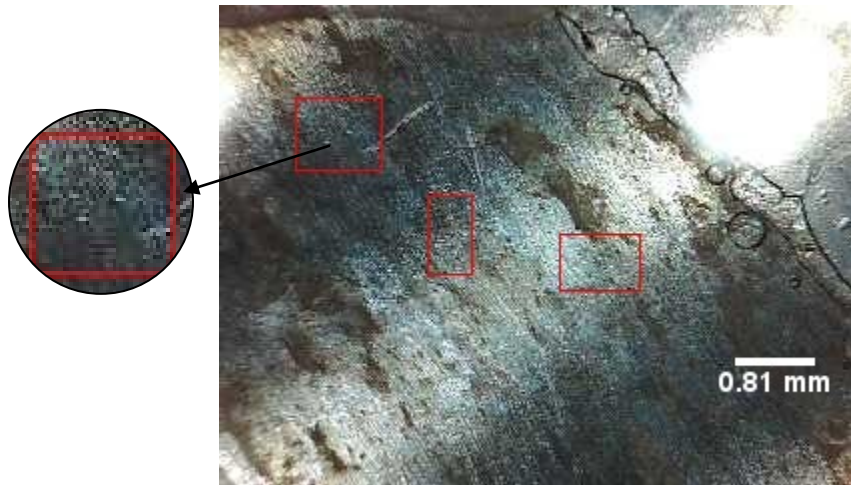
Optical Assessment

The insonated channel flow visualization film pictures establish that 20 W insonation applied to the channel removes larger bubbles and vapor blocks in less than 1 second after the application of the acoustic field, see figure Fig. 4.12. These preliminary observations did not attempt to quantify flow rates, frequencies or channel dimensions that produce best results, but instead were intended to verify that the largest bubbles sizes could be managed. As seen in Fig 4.12 (c) larger bubbles have been reduced to smaller ones ~ 0.1 mm in diameter.



(a) before insonation

(b) < 1sec after insonation



(c) small bubbles remaining after insonation

Figure 4.12. Images extracted from video of insonated small channel

Experiments on a milli and a micro channel cooler

Experiments on a milli and a micro channel (Fixtures 1 and 2) cooler were performed at the strong resonant frequencies of the two project ultrasonic transducers to learn if an improvement in heat exchanger performance by insonation would be detected, thus validating the hypothesis of this research. These experiments were not intended to identify optimum combinations of channel size, flow rate and insonation frequency as this is left for future work.

Heater, exchanger case and coolant temperatures (in and out) were taken as a function of time as the cooler was operated at various flow rates, and was intermittently insonated. Power input to the heater was controlled and monitored.

Approximating the acoustic field in the milli channel cooler

The radiating ultrasonic transducer used for the milli cooler was the 28 kHz Langevin, while the 120 kHz Langevin was used for the micro exchanger. The reason for switching to the higher frequency transducer to insonate fixture 2 is that it is a better match for acoustic power transfer to the smaller hydraulic micro channel. The frequencies of operation of the two radiating transducers were determined by intermediate resonances of these transducers which would support power transfer from the Crest audio amplifier whose cutoff frequency is normally 20 kHz. Frequencies between these value are inefficient for getting the acoustic signal into the coolant.

An approximation of the acoustic pressure field delivered by the 28 kHz project transducer was done on the milli channel cooler which yielded an acoustic pressure in the

cooler body of 80 kPa, or about 0.8 bar when the transducer was driven by a continuous sine wave amplified to 160 V_{pp} delivering a current of 117 mA_{pp}. Considering a 30 degree phase difference, the input power was approximately 1.4 W. The power measured in the heat exchanger was 0.33 W. This computation was made from $P_{in}=mc_p\Delta T/t$ where m is the mass of the milli cooler, c_p the specific heat of brass, ΔT the measured temperature change of the assembly in a time t. Calculation of the acoustic pressure field, p in bars (RMS), was done by equating transmitted acoustic intensity in the cooler to the power absorbed by the milli cooler as evident from its temperature rise in a time, t, according to conservation of energy, thus,

$$\frac{p^2}{\rho c} \left(\frac{W}{m^2} \right) = \frac{mc_p\Delta T}{tA_s} \left(\frac{W}{m^2} \right) \quad (9)$$

With terms as described above, ρ the density of brass and c the velocity of sound in brass. Two data analysis methods were employed: one examined the temperature profiled of the difference between the heater and the exchanger case as a function of the coolant temperature within the saturation state of the coolant. The second analysis method looked at the reduction of thermal resistances when forced and unforced as a function of flow rate and insonation frequency.

Measured tube temperature spanning low quality

The coolant leaving the test coolers was measured in the exit tubing ~10-15 cm from the cooler. Boiling coolant at a constant 94.6 C in the cooler channel would cool slightly at the thermocouple measurement point. An experiment to approximate the

variation in measured temperature to the quality state of the in-channel coolant was performed by boiling water in a flask and simultaneously measuring exit flow temperature at 3 mL/min 15 cm from the cooler in the same rubber tubing used in the experiments to follow. The boiled water was stabilized at approximately 30 % vapor bubbles then allowed to cool just to the beginning of boiling. Exit flow temperature measurements were made during this reduction of boiling quality. The results are shown in Fig 4.13.

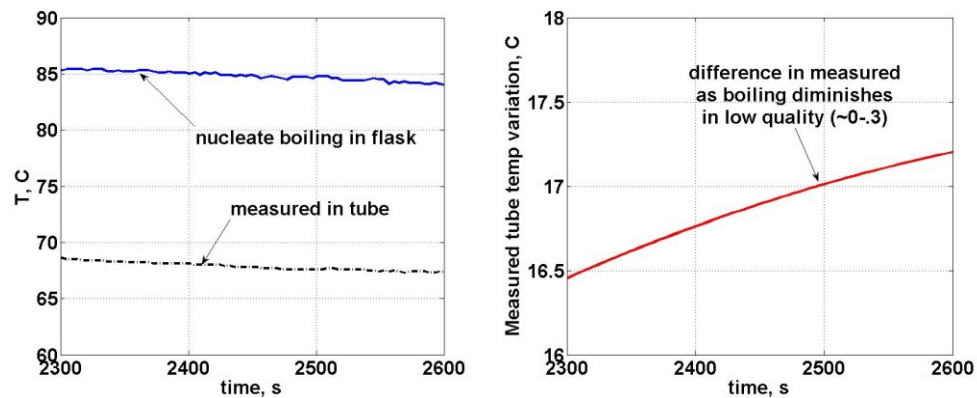
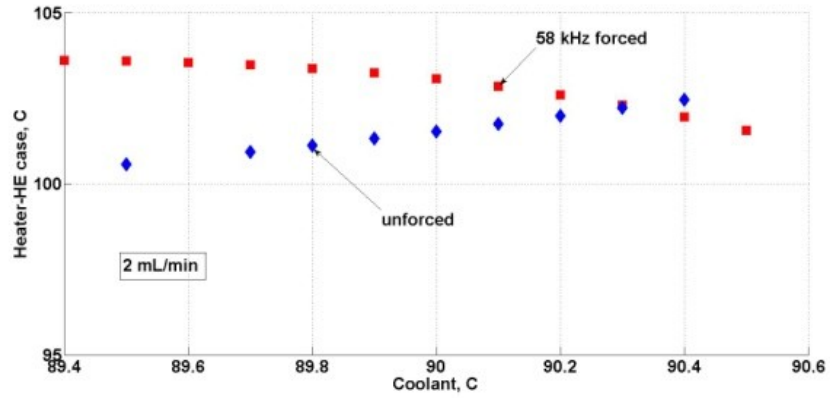


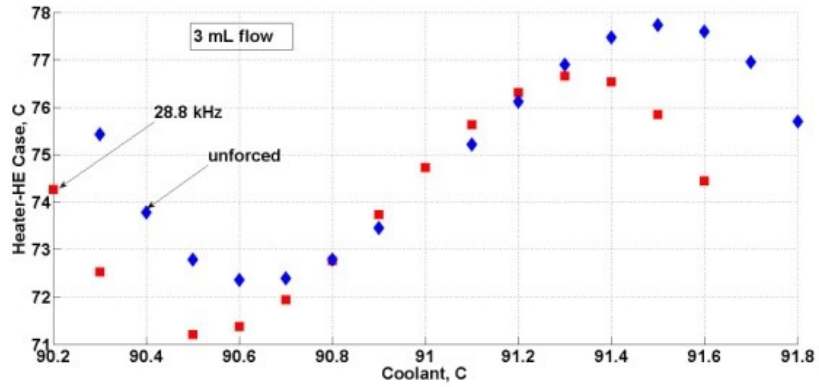
Figure 4.13 Variation in exit coolant temperature versus quality.

The results of Fig 4.13 show that the coolant measurement is an amplified indicator of the range of low quality boiling. This variation approaches 1 degree. This observation was useful in understanding experimental results that follow.

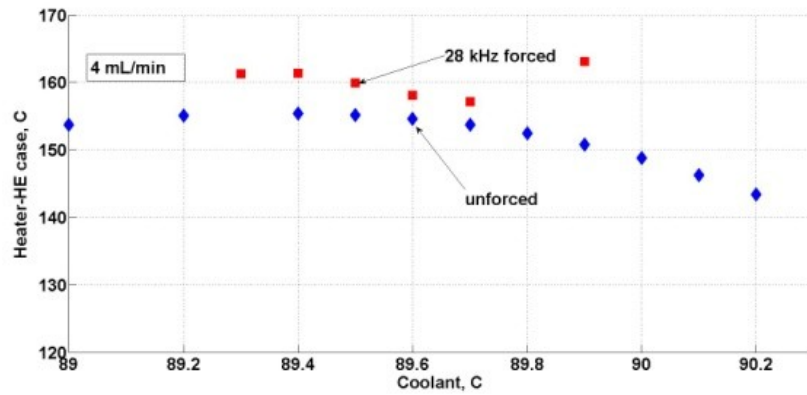
Temperature profiles when insonated



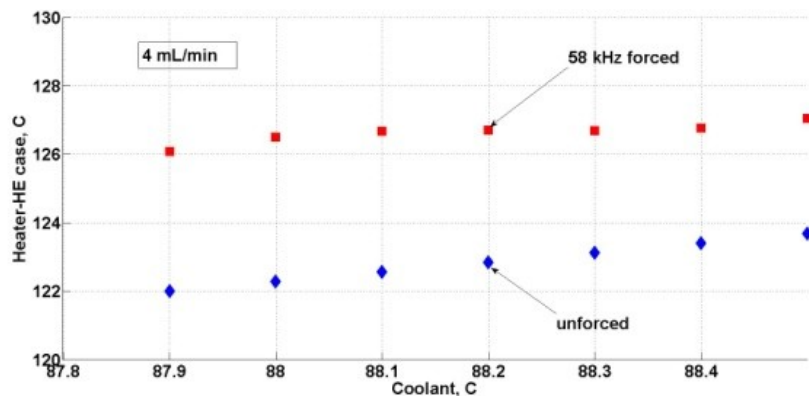
(a) 2 m/min; 58 kHz



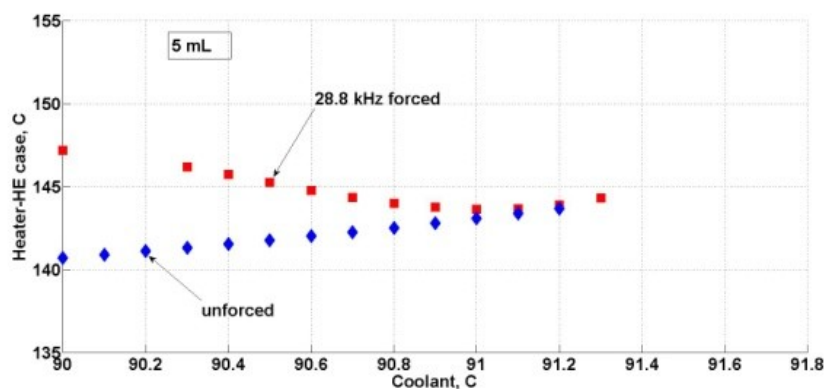
(b) 3 mL/min; 28 kHz



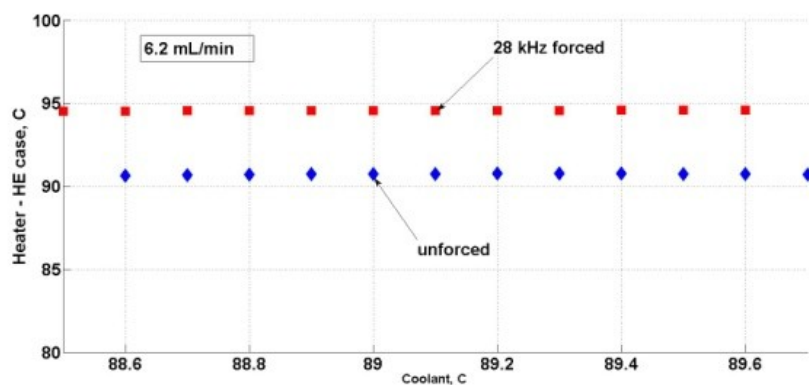
(c) 4 mL/min; 28 kHz



(d) 4 mL/min; 58 kHz



(e) 5 mL/min; 28 kHz



(f) 6.2 mL/min; 28 kHz

Figure 4.14 Profiles of the difference of heater and cooler temperature as a function of coolant temperature when the state of the coolant in the micro channel is under the saturation dome. Plots are for Fixture 1 for flow rates of 2-6.2 mL/min, and insonation of 28 and 58 kHz.

Examination of the temperature profiles in Fig 4.14 (especially (b)) suggests that more than one mechanism may be operative in improving cooler performance by insonation. It is believed that the dominant mechanism near low quality is due to bubble management resulting from the combined effects of nucleation, bubble shrinkage and population control. The improvement noted at the higher quality may be due to transducer harmonics or may be the result of improved mixing from flow interaction with the acoustic field such as acoustic streaming. Determining these possible mechanisms is left for future work.

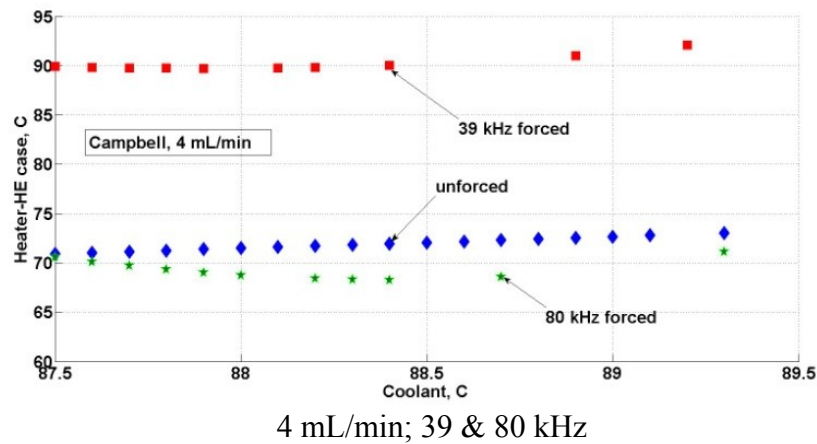


Figure 4.15 Profiles of the difference of heater and exchanger temperature as a function of coolant temperature when the state of the coolant in the micro channels under the saturation dome. Plots are for Fixture 2 for a flow rate of 4 mL/min, and insonation of 39 and 80 kHz.

Fixture	Figure	Frequencyk Hz	Rate mL/min	ΔT_{max}
1	4.14 A	58	2	+4/-1
1	4.14 B	28	3	-3/-3
1	4.14 C	28	4	+5
1	4.14 D	58	4	+4
1	4.14 E	28	5	+6
1	4.14 F	28	6.2	+5
2	4.15	39	4	+20
2	4.15	80	4	-5

Table 4.16 Summary of profile results plotted in Figures 4.14-15

Thermal resistance when insonated

The result of thermal resistance analysis on the experimental data is presented in the next three figures. The coolant temperature shown was made in the rubber tubing exit flow from the cooler approximately 10 cm from the exit which allowed the coolant to cool from the 94.6 C boiling point for Denver. Another explanation for the lower measured coolant temperature is thermocouple calibration. With this in mind, the lower coolant water temperatures identify the beginning of boiling as correspondence with visual inspection of vapor generation in the clear parts of the tubing confirmed.

Fig 4.17 presents the best reduction in thermal resistance found in a broad survey in which insonation frequencies were swept from 4-100 kHz at a flow rate of approximately 2-4 mL/min. During these experiments heater temperatures were varied from 120-190 C. The purpose of the survey was to identify domains for future detailed

study. The 28 kHz transducer was used being operated near the conditions discussed in the field approximation discussed above. Analysis of this large data set found three point sets at 88.2, 88.4 and 88.4 water coolant temperature which had significant reductions in thermal resistance. The exact conditions which produced these points were not recorded, except it is known that these reductions occurred at the onset of boiling, and that they occurred in the milli cooler.

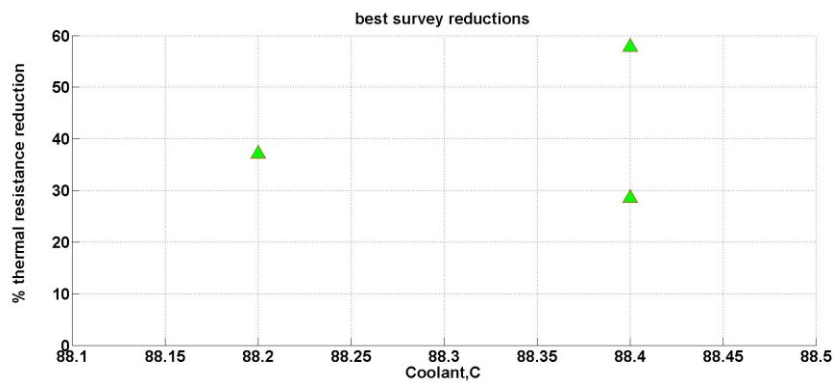


Figure 4.17 Best cases detail from the multi-frequency, multi-flow rates survey

Fig 4.18 (a) plots the reduction in thermal resistance from insonation on the milli channel cooler arranged as a function of flow rate. Fig 4.18 (b) are the results using the high frequency transducer which would have a different transducer/cooler contact. The data in (a) all used the low frequency transducer, and were done in almost identical conditions.

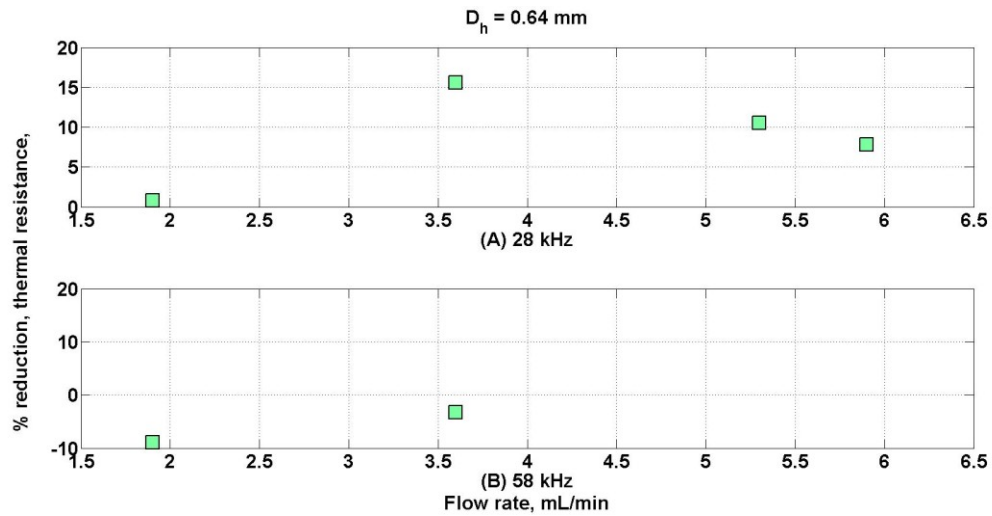


Figure 4.18 Thermal resistance reduction from insonation at 28 and 58 kHz of fixture 1 as a function of flow rate.

Fig 4.18 (a) shows a peak improvement around 3.6 mL/min of 16 %. This is consistent with the thermal profile results of fig 4.16 (b). This peak is explained by the ability of 28 kHz insonation to shrink bubbles smaller than 0.2 mm in diameter which is $\frac{2}{3}$ channel height of the cooler tested. Bubbles of this size would be expected in low quality flow at lower flow rates.

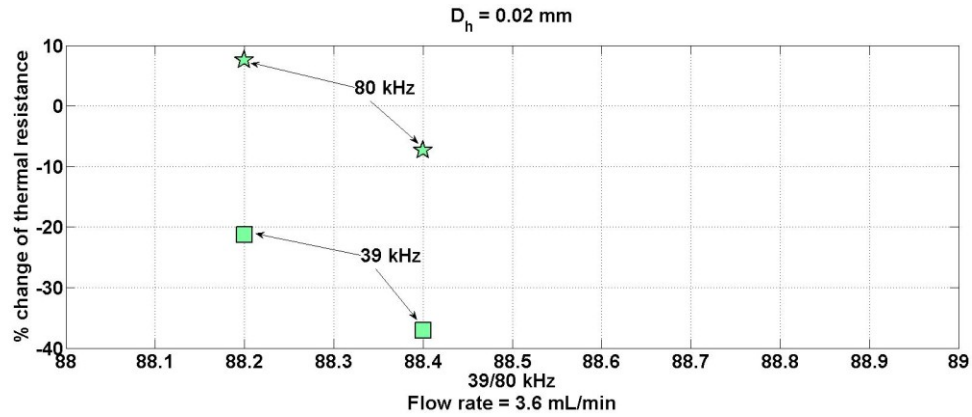


Figure 4.19 Thermal resistance reduction from insonation at 39 and 80kHz of fixture 2 at 3.6 mL/min flow rate.

Fig 4.19 presents thermal resistance improvement in a micro cooler exposed to ultrasonic irradiation. The height of this exchanger is 20 microns; the resonant frequency of a vapor bubble of this diameter is $3.26/0.010$ or 326 kHz. It was not possible to irradiate this exchanger near this frequency with the transducers and amplifiers available, but, insonating it at 39 and 80 kHz using the 120 kHz transducer shows the thermal resistance improving to 8% at the higher frequency and lower quality. This may be the result of the 80 kHz signal operating on vapor shapes spanning a fraction of the width of the 0.2 mm channel.

Pulsed-mode experiments

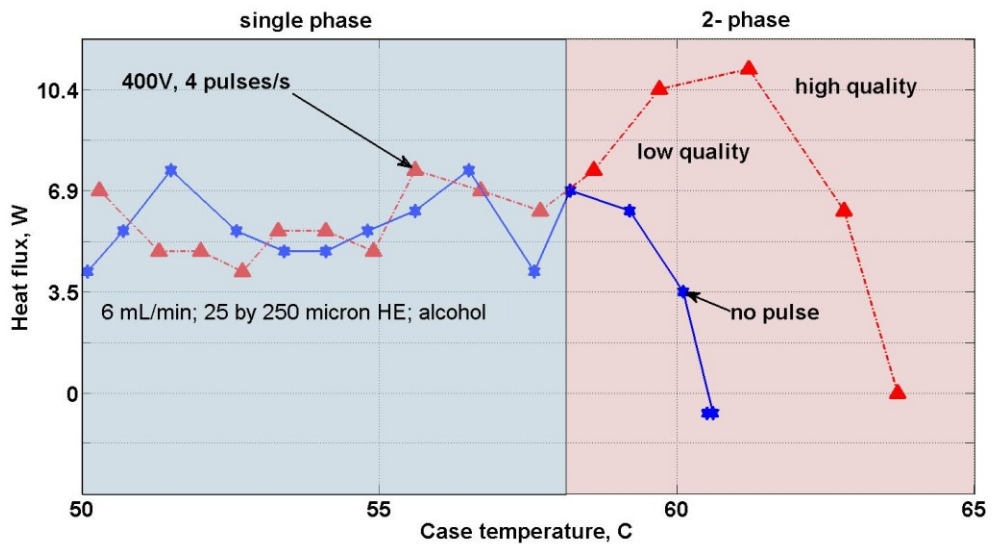


Figure 4.20 Pulsed mode experiment heat flux results

Fig 4.20 plots heat flux out of the fixture 3 after heating in contact with the cooler then separated from the heater and allowed to cool while temperatures are monitored. This was done with and without pulsed insonation. Coolant is ethanol having a boiling point of 78 C. Acoustic pulses are 400 Vdc, 5 microsecond duration repeating at 4 Hz generated from the prototype transducer driver. Cooler tested had a hydraulic diameter of 0.045 mm. Note the temperature measured is the case, not the coolant.

Discussion of results

The insonated channel flow visualization film pictures establish that 20 W insonation applied to the channel reduces the size of bubbles and removes vapor blocks very rapidly. It is seen in the picture immediately after insonation that the larger bubbles

have been significantly reduced in size rather than completely swept away as might be the case if the dominant mechanism were acoustic streaming. The observed reduction in size is consistent with the hypothesis that insonation near and above bubble resonant size can significantly shrink them. These preliminary observations did not attempt to quantify flow rates, frequencies or channel dimensions that produce best results.

In order to qualify and quantify the benefit of insonating micro channel coolers, fixtures 1 and 2 were studied under controlled conditions of flow rate and insonation frequencies. But, no attempt was made to determine thresholds of acoustic power which result in exchanger performance improvement. This because (a) the apparatus employed for the testing used commercial audio amplifiers impedance-matched to the transducer but still relatively inefficient for best transfer of acoustic power into the exchanger, (d) the attachment between radiating transducer and exchanger was always problematic, and would sometimes loosen during the test and (c) there was always a phase difference of at least 45 degrees between voltage and current into the transducer further limiting power transfer. For these reasons the signal to the transducer was always maximized at transducer resonance points.

Test fixture 1 was better matched to the insonation frequencies from the high-power, project Langevin transducers which have design resonant frequencies of 28 and 120 kHz. Testing with fixture 1 began with a broad survey over frequency at a fixed flow rate. It then continued with studies at fixed frequencies for various flow rates. It was found that a maximum benefit approaching 16 % improvement in thermal resistance was found at 3.6 mL/min. The best benefit gain of over 60 % was seen in the broad survey at

4 mL/min but at an unknown frequency. The benefits all occurred just at the onset of boiling.

Testing of fixture 2, a micro channel cooler was done using the higher frequency transducer at a fixed flow rate of 4 mL/min and insonation frequencies of 39 and 80 kHz. As expected these frequencies were too low to produce a benefit, but the 80 kHz showed a significant improvement over insonation at 39 kHz indicating the 80 kHz was beginning to operate on vapor objects larger than channel height. This is another indication that bubble size management is the operative mechanism and not simply vibration of the walls shedding bubbles attached by surface tension or sweeping them away from acoustic streaming.

The pulsing experiment performed on the 40 μm hydraulic diameter micro channel produced a 3X heat flux improvement. It is thought that this was due to the small hydraulic diameter, and small surface area of this exchanger coupled with the ability of the high voltage pulsing circuit to generate high frequency components affecting the bubble size within the 25 micron channel height. This benefit also occurred at the onset of boiling.

Conclusion

The experimental results support the hypothesis that insonation can improve heat flux dissipation, but only under a range of conditions. It has been found that insonation at frequencies near the resonance of bubbles smaller than the height of the micro channel generally improves heat removal. The best performance enhancement is observed in the low quality region well way from dry out. In the single phase region insonation appears to add heat to the system through absorption of acoustic energy faster than sub cooled bubble nucleation subtracts.

It is believed that this benefit results from insonation retarding bubble growth in the exit section of the channel allowing bubbles already formed to exit the channel with their entrained latent heat. Conversely, without insonation bubble coalescence can occur leading to slug and annular flow. It does not appear that this enhancement is primarily a result of of acoustic streaming or vibration of the walls although these mechanisms may operate in flow regimes not studied. The evidence against these mechanisms being primary is that the beneficial affects observed were all associated at the onset of boiling, occurred only at flow rates around 3.6 mL/min and at a frequency matching interior bubble szes of around one-half to two-thirds channel height. If streaming and wall vibration were dominant then the affect would be more generalized.

Although the effects of rectified diffusion occur rapidly (within a few thousand cycles as established by modeling, see Chapter 3) the reestablishment of large bubble flow resistance requires minutes. This suggests that a duty cycle at a very low frequency

(4 Hz was used in this research), and perhaps even as reduced as 0.001%, using a pulsed signal would achieve similar results to the continuous application of an acoustic field.

References

1. Tukerman, D.B., Pease, R.F.W., High-performance heat sinking for VLSI, *Electron Device Letters, IEEE*, May 1981, V2, I5, p 126-129
2. Kandlikar, S.G., Nucleation characteristics and stability considerations during flow boiling in micro channels, *Experimental Thermal and Fluid Science*, 30, (2006) p 441-447
3. Blackmore, B.P., *Detachment of air bubbles from slit micro channels with shearing flow*, MS Thesis, University of Alberta, (2000)
4. Leighton, T.G., 'The Acoustic Bubble, Academic Press (1977), pp73-92
5. Frampton, K.D., The scaling of acoustic streaming for application in micro-fluidic devices, *Applied Acoustics*, V64, I7, (July 2003), p 681-692
6. Cubaud, T., *et al.*, Transport of bubbles in square micro channels, *Physics of Fluids*, V 16, No 12, (2004), p 4575-4585
7. Gupta, R., *et al.*, On the CFD modelling of Taylor flow in micro channels, *Chemical Engineering Science*, 64, (2009) p. 2941-2950

8. Brandner J.J., *et al.*, Concepts and realization of microstructure heat exchangers for enhanced heat transfer, *Experimental Thermal and Fluid Science*, 30 (2006) p. 801-809
9. Qu, W., et al., Transport Phenomena in Two-Phase Micro-Channel Heat Sinks, Proceedings of IMECE2002, Nov 2002, New Orleans, Louisiana
10. Lee, J., et al., Two-phase flow in high-heat-flux micro-channel heat sink for refrigeration cooling applications: Part II-heat transfer characteristics, *International Journal of Heat and Mass Transfer* 48 (2005) 941-955
11. Bertsch, et al., Review and comparative analysis of studies on saturated flow boiling in small channels, CTRC Research Publications Cooling Technologies Research Center, (2008) Purdue University, Purdue e-Pubs

Chapter Five: Summary

Hypothesis

The basis of the research performed was the hypothesis that insonating a micro channel cooler would improve performance. A benefit results from the interaction between the acoustic field and vapor bubbles which develop in the channel when the coolant begins to boil. The primary role of insonation is seen as retarding this process by reducing bubble size past a frequency-related threshold of around one third to one half channel height. Secondary causes may be from nucleation of small latent heat carrying bubbles in the flow, removal of large vapor objects in the end of the channel by the forces of induced acoustic streaming and vibrational dislodging bubbles adhered to the wall by surface tension.

In order to test the hypothesis

The hypothesis was tested by insonating several micro channel coolers of different hydraulic dimensions at different flow rates and at different insonation frequencies. However, before that could happen several technologies involved in such testing were mastered.

Transducers and their operation

In conducting this research many PZT ultrasonic transducers were tried. The lower power ones typically used in ranging, doorbells, etc. were quickly abandoned. Four models were used: a 14 and 50 mm disk, and a 28 and 44 kHz Langevin bolt-type. Ultrasonic transducers of these types are polarized ceramic, and have capacitance which gives them a complex impedance. High power audio amplifiers were employed to drive them in circuits that compensate for reactance..

The Langevin transducers were also pulse driven to get 400 V pulses of 10-20 μ s using a pulse generator developed for this purpose.

Producing, irradiating and photographing rising bubbles in water

The effect of insonating rising air bubbles was tested in aquariums after techniques for producing nearly monodisperse 0.1-0.4 mm radius bubbles were mastered.

These bubble columns were irradiated with ultrasonic transducers immersed in water approximately 5-10 cm away employing individual transducers and arrays

Photographs producing whole bubble images without highlights were made with high-intensity backlighting behind frosted glass. To capture bubbles in flight, and to track changes in them as a result of insonation, high-speed commercial burst-mode cameras were employed which could take 40-60 frames/second at 1/2000 to 1/4000 s.

Pictures made of forced and unforced rising bubbles were processed by image analysis. Statistical analyses were performed to quantify size and frequency change in populations, and montages made to track image change in particular bubbles.

Measuring the acoustic field

A Faraday cage shielded, grounded probe was developed along with a force beam calibrator to measure the acoustic field along the irradiated path of flight. Ray-trace modeling of acoustic fields, and associated tank tests were done to validate probe performance. A journal paper resulted from this effort.

Modeling the effect on rising bubbles

A numerical analysis thermodynamic model for bubble growth and shrinkage was developed from the picture and field data. This model transforms the pulsing work done on the bubble from the acoustic field into a thermal pulse which adds heat to it. The resulting volume change at constant density and temperature specifies the added mass and describes the new size. Predictions of the model were validated by size change under controlled conditions in the experiments, and also by growth values given by others published in the literature. A journal paper is pending.

The model and the experiments show that ultrasonic insonation near the resonant frequency of an air bubble entrained in water will change its size. It has also been discovered that nearly mono-disperse groups of bubbles will have their mean size shifted towards the insonation frequency when insonated at a frequency close to resonance.

Testing the hypothesis on micro channel coolers

The rising bubble experiments and the derived model establish that ultrasonic insonation can shrink bubbles when a bubble is irradiated at a frequency in which $\omega(\text{insonation})/\Omega_0(\text{bubble}) \leq 1.1$. Thus, selective insonation should improve performance of a micro channel cooler when bubbles are forming in the exchanger of a size that is smaller than channel height by preventing further growth leading to flow reduction by clogging or increased drag

An initial experiment to test the hypothesis was done by insonifying an open channel of sub millimeter dimensions while video-taping the effect on flow when insonation was turned on. The effect seen was dramatic as the still pictures of this experiment shown in Chapter 4 establish. Vapor objects are allowed to form in the saturated coolant, which are immediately cleared by insonation. Importantly, while large bubbles disappeared in the video pictures, small bubbles remained.

Three sub-millimeter channel coolers were made and tested by insonating them with continuous sine waves at power levels approaching 20 W, and by 400 V_{dc}, 10 μ s pulses repeating at 4 Hz both applied over 1.5 cm². Ultrasonic stimulation at 28 and 58 kHz produced significant benefit approaching 5 W/cm² improvement in heat flux when flow rate through the exchanger was \sim 3 mL/min. A similar improvement was observed when pulsing at a higher flow rate \sim 6 mL/min. Improvement from insonation occurred when the insonation frequency matched an entrained bubble size of $\frac{1}{3}$ to $\frac{1}{2}$ channel height.

Conclusion of the work

The research hypothesis has been verified: insonating mille and micro channel coolers operating with its coolant state saturated at low quality, and at low flow rates at frequencies matching the resonance of an air bubble whose size is $\frac{1}{3}$ to $\frac{1}{2}$ channel height can increase heat flux removal. Observation has established a flux improvement of as much as 5 W/cm^2 in the exchangers studied. In the case of pulsing, the energy stored in the $.4 \mu\text{F}$ capacitor for a $20 \mu\text{s}$ pulse is 0.032 J . At a repetition rate of 4 Hz this adds to 0.13 W . This is applied to the heat exchanger over an area of $\sim 1.5 \text{ cm}^2$. Thus, an input power of $\sim 0.1 \text{ W/cm}^2$ can produce a benefit of 5 W/cm^2 in heat flux removal.

Ultrasonic insonation may also be improving micro channel cooler performance by other means than selective bubble shrinkage at the onset of two phase flow. Although it is doubtful in these experiments that acoustic streaming was sweeping out bubbles before reaching a detrimental, clogging size because (a) the applied field is perpendicular to flow, and (b) the observed effect is limited and would not be so limited if streaming were a factor. But, it is possible that streaming, or forcing agitation, might dislodge bubbles from the wall sooner, and at a smaller size than would occur without insonation. It is also possible that small bubble nucleation is occurring at channel crevices which produces bubbles that carry away latent heat. This research has shown nucleation from insonation. Both possibilities will be explored in future work.

Appendix A: Photography

Getting started

At the heart of the study of the effect of ultrasound irradiation of air bubbles in flight in small water tanks is the difficulty of visualizing the effect on the bubble so measurements can be made. At the beginning of this project the lab had a professional grade Olympus 35 mm film camera. The procedure for macro photography of moving bubbles, and how to light them to produce images that were not dominated by highlights caused by lighting was not understood. Further, the cost and time lost in photo documenting insonified bubbles by a film camera was prohibitive. It was soon realized that digital photography was necessary. As for lighting, backlighting was essential and was recommended by Dr. Lengsfeld based on her work with tiny droplets, and by Michael Much who works for Olympus and has become an accomplished artist in making beautiful pictures of soap bubbles. Michael advised us on what cameras to buy and confirmed the need for backlighting.

Here are a few samples of the more than 10,000 pictures made during this work beginning with the very misleading color photograph made with the film camera in which highlights can be interpreted as modal shape changes in the insonified bubble.



Figure A.1 Olympic 35 mm film – Bubbles in flight

High-resolution bubbles in flight from a porous wooden bubble block

In order to produce quality photographs of rising air bubbles, appropriate bubble streams of controllable size had to be created. Just about every apparatus used in aquarium aeration and other apparatus invented by us was evaluated for making bubble streams. In the end two devices worked for bubble stream production: one is a finely porous wooden block attached to very slightly pressurized air hose and reservoir, the other, again suggested by Dr. Lengsfeld, is a small stainless steel tube having a very small hole through it. This we called a bubble pipe. This next picture shows unradiated bubbles rising from the bubble block in a small aquarium which is back lighted by

reflected high intensity 850 W from a professional photographer's halogen spot light. The picture was taken with an Olympus E-510, 10 MPx camera with a 50 mm Zuiko lens at 1/4000 second exposure. It's striking how clearly the bubbles are defined, and that no misleading highlights are present. These are ideal for image analysis by the NIH program, ImageJ, that was employed extensively in this work. The presence of the ruler in the image permits calibration of the ImageJ analysis function.

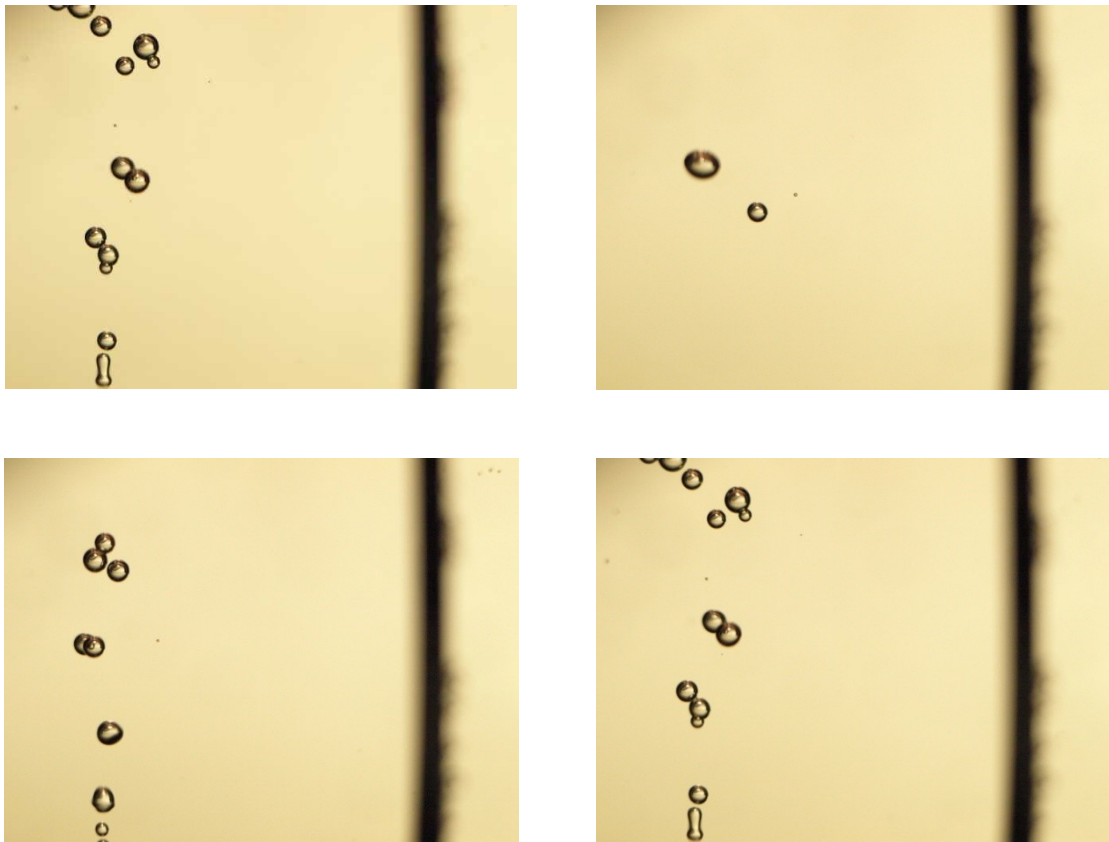


Figure A.2 Olympus E-510 10 MPx digital, Zuiko lens

The next set of 6 pictures show insonified bubbles rising in the water aquarium that were produced by the bubble pipe and illuminated similarly to the picture above..

These are also taken with the Olympus E-510.

This set of pictures is remarkable for the fact that it reveals bubbles that are undergoing induced shape changes which promote in some cases aggregation in flight. Aggregation of bubbles in flight when not insonated is very rare. Even when promoted by the energy of insonation, aggregation in flight accounts for only a few percent of observed bubble growth.



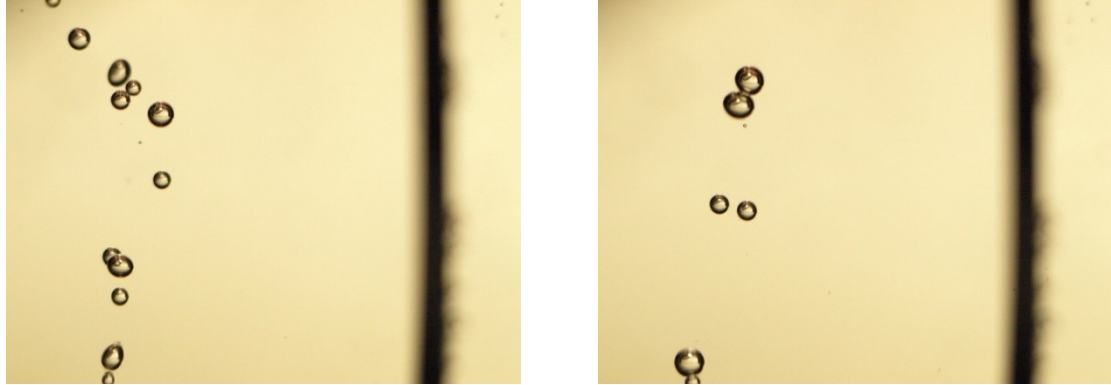


Figure A.3 Bubbles forced into contact

The visualization of bubble aggregation in flight prompted us to pursue for a while whether preferential contact angles could be deduced from the pictures. This remains a work in progress which requires much higher speed photography to pin down the contact angle at the exact moment of aggregation. However, the study of coalescing bubbles remains a fascinating topic. In pursuing our main objective, the hypothesis that bubble populations can be managed by ultrasonics to benefit practical applications, pictures were taken showing coalescence. Samples of these are shown in the next panel.

Bubbles coalescing

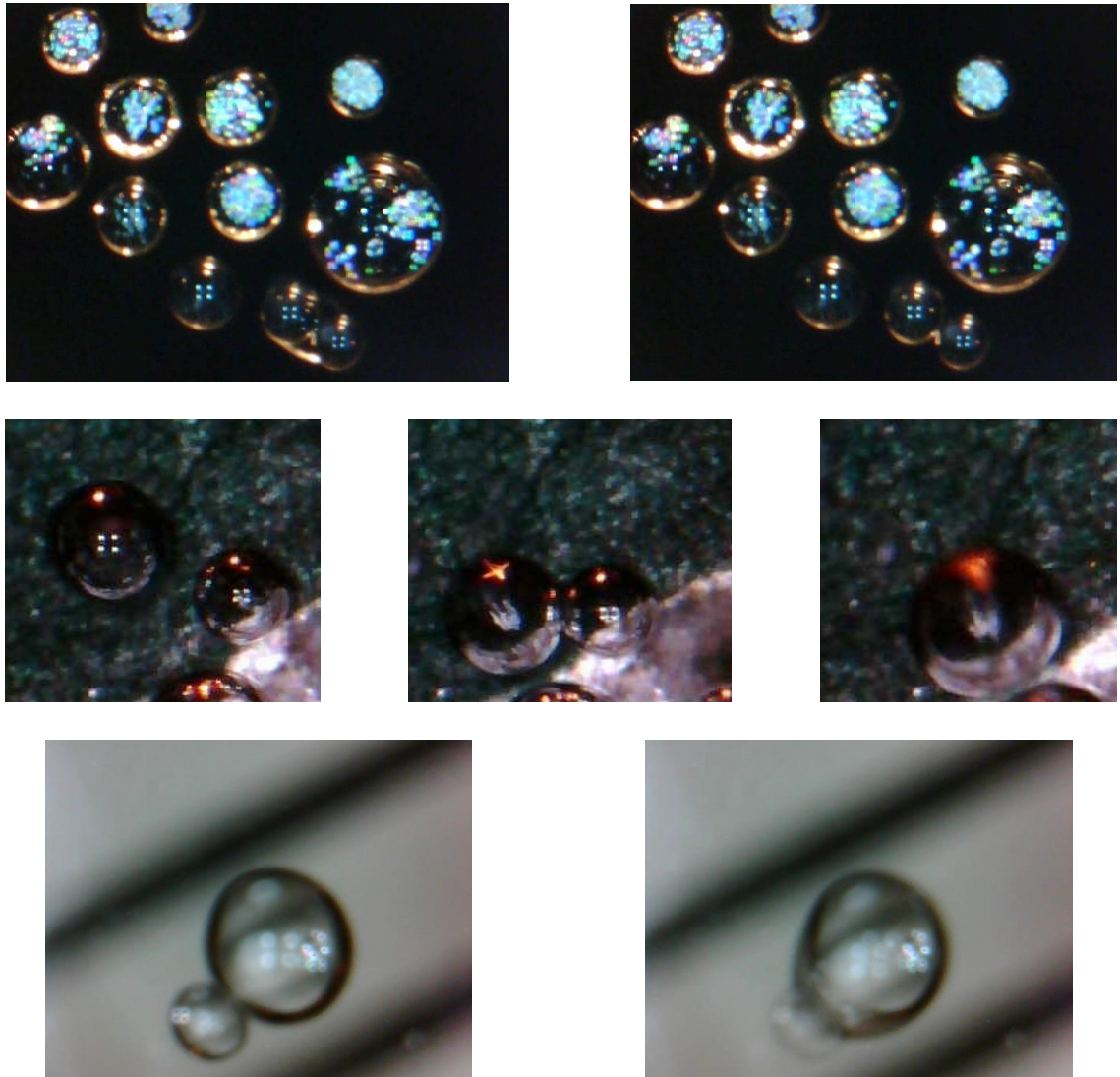


Figure A.4 Bubbles coalescing when forced

Although the bulk of the work done in the pursuit of the objectives stated for proving the hypothesis of effective bubble management by insonation was done on air bubbles rising in plain water, other fluids were examined. The interest in other fluids was

mostly that associated with examining the change from surface tension and viscosity. In doing this another bubble change mechanism was photodocumented – bubble aggregation, the opposite of coalescence.

Bubble aggregation

It came as surprise that fluids such as glycerin and vinegar should produce pictures showing bubbles aggregating in heads of bubbles clustered together attached to a long tail as shown in the next panel. The fluid in the top row is glycerin and in the bottom row vinegar.

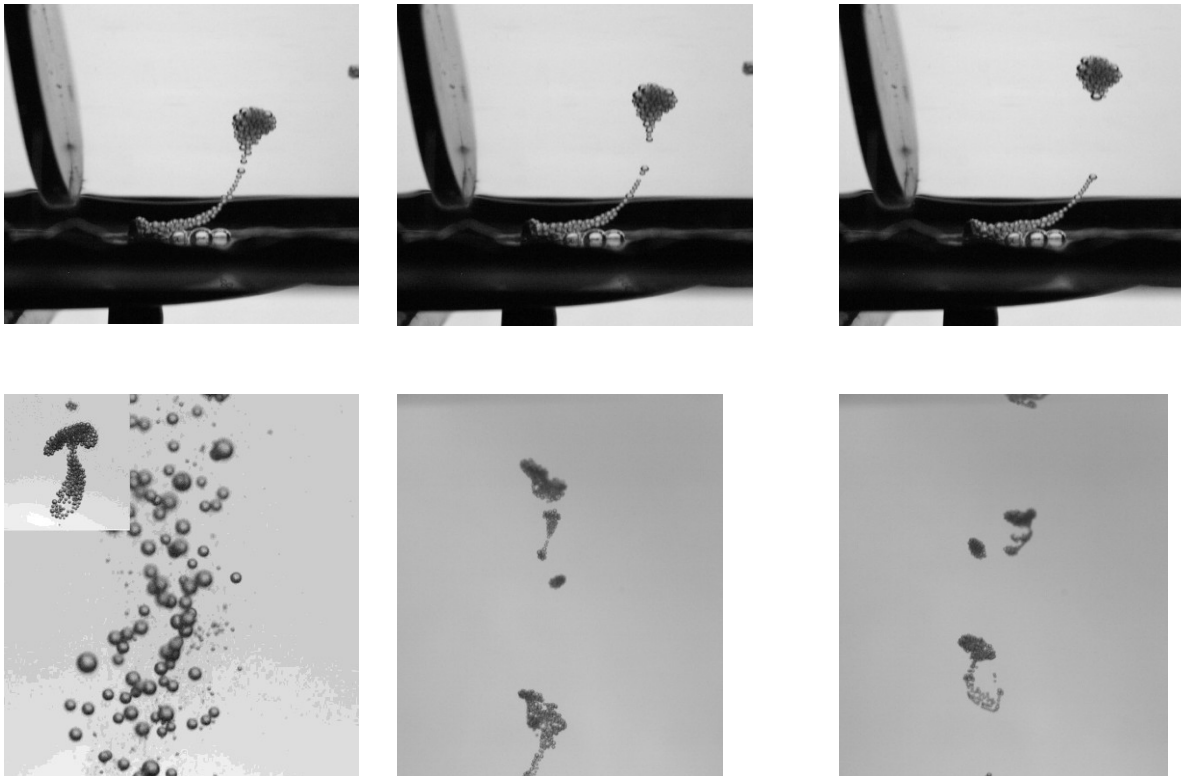


Figure A.5 Bubbles aggregation when forced

Appendix B Nucleation from insonation in micro channels

Introduction

The research done has concentrated on the improvement in micro channel heat flux removal in lower quality two-phase operation caused by bubble shrinkage thought to prolong channel blocking from bubble growth. This is an assumption based on insonated bubble behavior studied in chapter 2.

Another mechanism that could be operative which would also account for increased heat flux removal, and which also operates near or at saturation, is the addition in the flow of nucleated bubbles which would also remove latent heat.

This mechanism was examined by experimenting with the apparatus shown below.

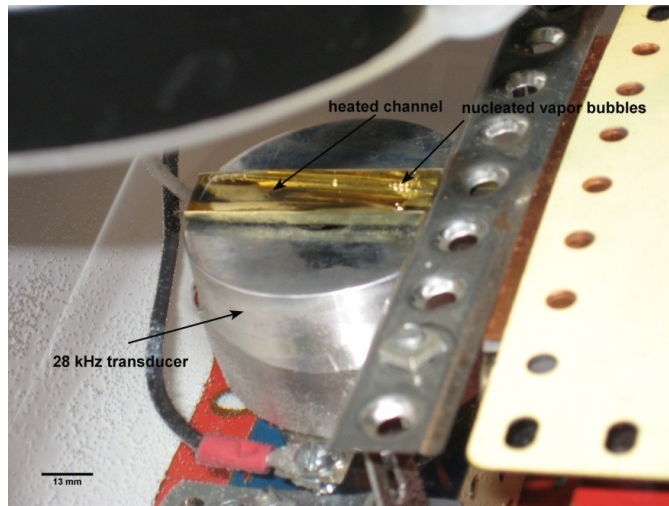


Figure B.1 Apparatus for the study of nucleation by insonation.

In figure B-1 a 28 kHz PZT Langevin transducer (the same as described in Chapter 4) is pressed firmly against the bottom of a 1 cm wide brass channel that has its top cut away to expose 5.2 cm of channel. After the channel cutout, 10 cm of it are clamped into an aluminum heated block having two 100 W cylindrical heating elements controlled by a variac. Following this is a hose connection to a dc aquarium pump for circulating water through it. A 5 frames/s Olympic camera is suspended overhead to photograph the channel through a magnifying lens. Photo documentation begins when the water is heated to the onset of boiling so that vapor bubbles produced in the heater exit the heater block and are photographed passing over the 5 cm insonation zone. Each frame is 0.2 seconds apart. This apparatus was initially used to show bubble change, and destruction resulting from ultrasound exposure.

Minnaert vapor bubble sesonance

Minnaert bubble resonance for vapor bubbles is computed from:

$$f = \frac{1}{2\pi a} \left(\frac{3\gamma p_a}{\rho} \right)^{\frac{1}{2}} \text{ (m/s)} \tag{B1}$$

In which f is resonant frequency in m/s, a is bubble radius in m, λ is the polytropic constant (1.2 given by Crum), p_a is atmospheric pressure in Pa and ρ is water density in kg/m^3 . For vapor bubbles in water this reduces to $fa=3.26 \text{ (m/s)}$.

Forced nucleation

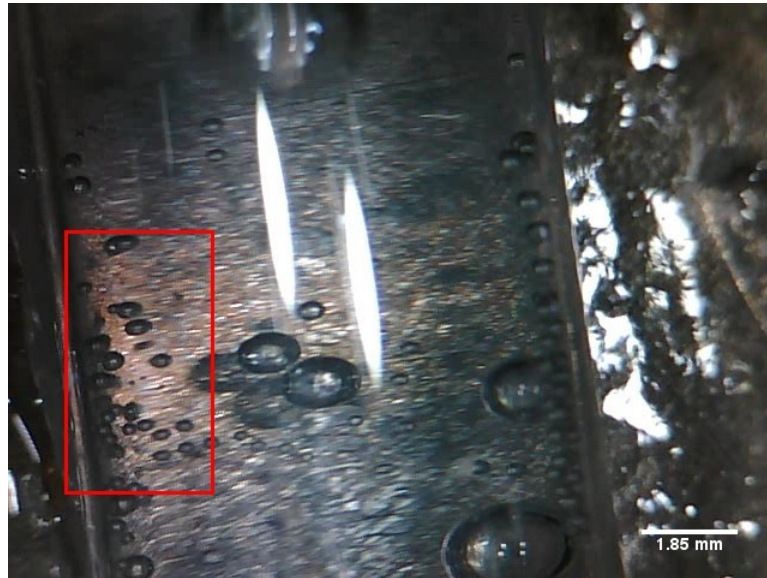


Figure B.2 View of the 9.6 mm channel.

In Fig B-2, large bubbles were produced in the heater block and are travelling from the top of the picture towards the bottom. The large bubbles shown are much larger than would be effected by the 28 kHz insonation. The red box shows a population of bubbles that have been nucleated and which have grown to resonant size. Subsequent frame analysis of this population of bubbles shows that having grown to resonant size they remain attached to the channel until one of several events occur:

1. If the liquid surface layer diminishes in the channel so that the top of the bubble makes contact with the surface, the bubble will burst, or be rapidly

carried along with the flow. This is probably due to surface tension forces at the top of the bubble moving with the flow which pulls the bubble from its stationary contact.

2. If another bubble approaches and makes contact, coalescence will usually result. Observation has indicated that such coalescence is more likely in an acoustic field probably due to forced contact. Often this has a cascade effect in which the larger coalesced bubbles make contact and coalesce again. When a sufficiently large bubble results, the surface tension bond to the channel is broken by drag and buoyancy forces, and the larger bubble is swept along with the flow.
3. If a large vapor slug exits the heater it will sweep all the smaller bubbles in its path.

Bubbles undergoing nucleation

Two instances have been captured from the photo documentation sets in this insonated channel study. These are shown in Figs B-3 and B-4. In each case two enlarged photographs are presented that are 0.2 s apart (camera framerate). Black arrows mark the vacant spot before nucleation in the first photograph, then the nucleated bubble just as it appears. In both cases the first picture shows a blurred spot exactly where the nucleated bubble pops up.

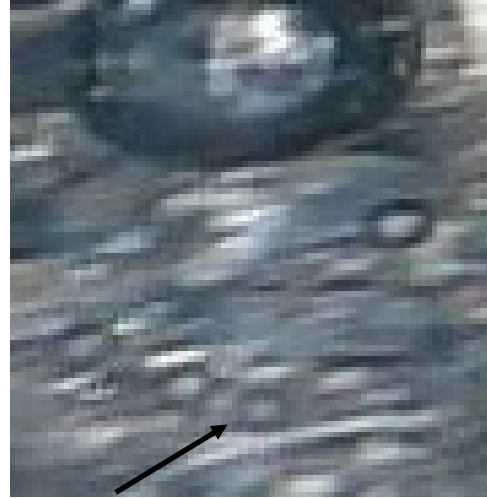


Figure B.3 small bubble $r = 0.221$ mm created by nucleation in 28 KHz field.



Figure B.4 small bubble $r = 0.222$ mm created by nucleation in 28 KHz field.

The nucleated bubbles appearing in Figs B-3 and B-4 are unique to insonation. This effect is not observed when the acoustic forcing field is turned off. In both cases the size of the initially nucleated bubble was the same within the accuracy of measurement. It is interesting to note that the Minnaert resonance of both bubbles is 29.4 kHz when being forced near 28 kHz. Judging from the nucleated bubbles surrounding these, they will subsequently grow slightly. This behavior would be in agreement with the theory of Chapter 3.

Conclusion

Insonation has been observed to nucleate vapor bubbles of a small size near the Minnaert frequency in channel flow. This is another heat removal mechanism associated with channel insonation providing a benefit linked to latent heat. Observation of this effect does not indicate that this would be a major mechanism compared to others studied. More work on the optimization of the use of intentional nucleation would be indicated.

Appendix C-Transducer driving circuit

Bubbles rising in water, and various micro channel coolers were insonated by PZT ultrasonic transducers. A piezoelectric transducer is modeled as a capacitor in series with a resistor. This capacitance varies with frequency. Around resonance of the transducer the capacitance is minimized and can be compensated by a small inductor. In the work done in this research a single compensating inductor of 2.5 mH was employed which effectively reduced phase angle between current through the transducer and the voltage applied for all the transducers used. The value of 2.5 mH was computed as the best for the 28 kHz transducer.

The transducer circuit with its series inductor was connected to the output of a Crest Vs 1100, Class AB audio amplifier specified to deliver 1100 W in stereo bridge mode into a real 8Ω load. The near resonant load of the 28 kHz compensated circuit was approximately 35Ω , therefore it was connected to the Crest amplifier through a 4:1 windings, impedance matching transformer. This is shown in the schematic, Fig. C.1.

Unlike a simple Class A amplifier having a single transistor amplifier stage and is limited in power output due to component heating, a Class AB amplifier has two active transistor stages: one to amplify the positive sine wave component, the other the negative. Class AB amplifiers are 50 % more efficient than Class A but offer some distortion due to crossover between amplifier stages. Most commercial audio amplifiers required to generate high output power are of the Class AB type.

Since sound fidelity is not a requirement for insonating micro channel coolers, in future development an amplifier should be chosen based on best efficiency in the 10-100 kHz range.

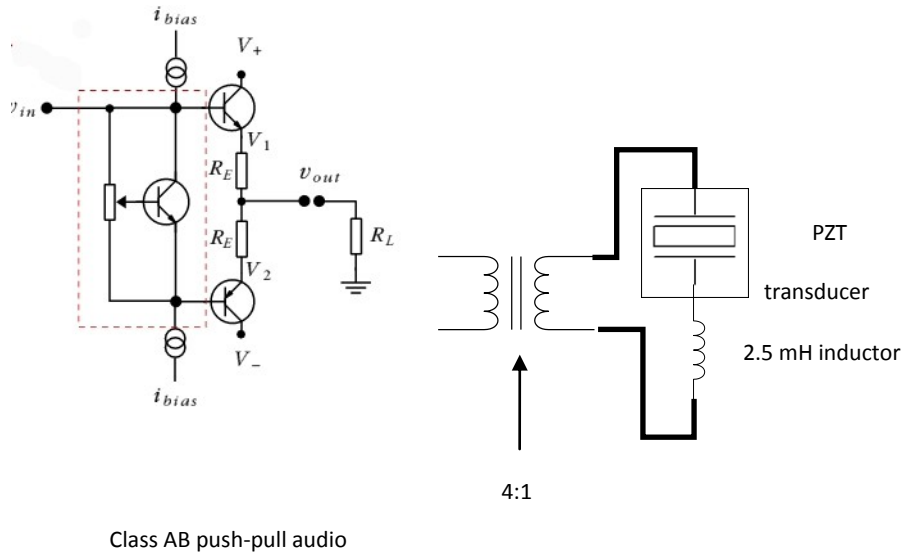


Figure C.1 Amplifier driving circuit for PZT transducer operation

Class C and D amplifiers could well be a better choice for this application. Class C are high efficiency, fixed frequency amplifiers that are designed to operate into a tuned (by reactive components) load, while Class D amplifiers synthesize the signal into pulse trains. The Class C mode of operation is very similar to that diagramed in Fig. C1. And the pulsed operation of Class D could probably be optimized to match the primary and secondary resonances of the operative piezoelectric transducer.

Appendix D Piezoelectric Properties of Project Transducers

Three types of piezoelectric transducers have been used in this research: disks; rings and Langevin bolt types as detailed in Table D.1.

Manufacturers specifications for transducers





Material	Dimensions	Resonance	Characteristics	Picture
SM111	50mm diameter 3 mm thick radial	44 kHz \pm 3	$\leq 8 \Omega$ 7200 pF @ 1 kHz $V_{in} \leq 1050$ $P_{max} \leq 55$ W	
SM111	9.6x8.2x9 .5 mm radial	98 kHz \pm 5	$\leq 20 \Omega$ 5000 pF	
SM118	79.5 x 45 x 35 mm	28 kHz \pm 0.5	$\leq 35 \Omega$ 3800 pF $V_{in} \leq 1600$ $P_{max} \leq 70$ W	
SM111	40x58 mm	120 kHz \pm 1.5	$\leq 25 \Omega$ 5100 pF $V_{in} \leq 1600$ $P_{max} \leq 60$ W	

Table D.1 Transducers used

Property Values

Property values for the poled ceramic materials for these are given in Table D.2.

PROPERTY	UNIT	SYMBOL	SM111	SM112	SM118	SM121	SM211	SM311	SM410	SM411
EQUIVALENCE			Modif. PZT-4	N/A	PZT-8	PZT-4	N/A	PZT-5H	PZT-5J	PZT-5K
			N/A	N/A	Navy Type III	Navy Type I	N/A	Navy Type VI	Navy Type V	Navy Type IV
Electromechanical coupling coefficient		K_p	0.58	0.59	0.51	0.54	0.67	0.65	0.64	0.6
		K_t	0.45	0.46	0.40	0.43	0.35	0.37	0.45	0.4
		K_{31}	0.34	0.35	0.30	0.32	0.41	0.38	0.36	0.3
Frequency constant	Hz • m	N_p	2200	2150	2340	2290	1940	1980	2030	2060
		N_t	2070	2050	2090	2080	1920	1950	2050	2000
		N_{31}	1680	1600	1700	1690	1410	1450	1460	1500
Piezoelectric constant	$\times 10^{-12} \text{m/v}$	d_{33}	320	360	250	300	650	600	500	500
		d_{31}	-140	-155	-100	-130	-320	-270	-210	-210
	$\times 10^{-3} \text{Vm/N}$	g_{33}	25	24.7	25.6	26.4	13.6	19.4	23.3	24.0
		g_{31}	-11.0	-10.6	-12.5	-12.9	-6.7	-9.2	-10.3	-10.0
Elastic Constant	$\times 10^{10} \text{N/m}^2$	Y_{33}	7.3	7.2	7.4	7.3	5.1	5.3	5.6	5.4
		Y_{11}	8.6	8.4	8.7	8.6	6.2	7.2	6.5	7.4
Mechanical Quality Factor	-----	Q_m	1800	1600	1200	1000	60	80	60	85
Dielectric Constant	@1KHz	$\epsilon^T_{33/\epsilon_0}$	1400	1600	1100	1300	5400	3500	2000	2100
Dissipation Factor	%@1KHz	$\tan \delta$	0.4	0.6	0.2	0.4	3.0	2.5	2.0	2.0
Curie Temperature	°C	T_c	320	320	300	320	165	220	320	320
Density	g/cm^3	ρ	7.9	7.9	7.6	7.8	7.8	7.8	7.7	7.8

Table D.2 Properties of piezoelectric materials used

The property values of particular interest are d_{33} and d_{31} as these map voltage applied to the plated electrodes to displacement in length or width as shown in the diagram, D.3.

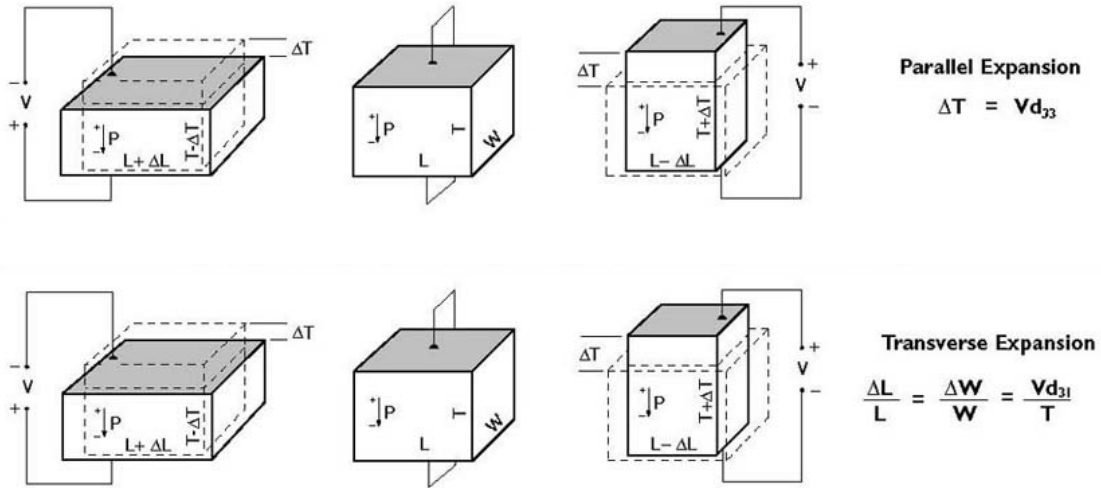


Figure D.3 Piezoelectric crystal expanding in length (top) and width (bottom)